



VRIJE UNIVERSITEIT BRUSSEL
FACULTEIT TOEGEPASTE WETENSCHAPPEN
VAKGROEP WERKTUIGKUNDE

Conception and Realization of Pleated Pneumatic Artificial Muscles and their Use as Compliant Actuation Elements

FRANK DAERDEN



VRIJE UNIVERSITEIT BRUSSEL
FACULTEIT TOEGEPASTE WETENSCHAPPEN
VAKGROEP WERKTUIGKUNDE

Conception and Realization of Pleated Pneumatic
Artificial Muscles and their Use as Compliant
Actuation Elements

FRANK DAERDEN

Proefschrift ingediend tot het behalen van de academische graad van
Doctor in de Toegepaste Wetenschappen

Academiejaar 1998–1999
Openbare Verdediging: 2 juli, 1999

Promotor: Prof. Dr. ir. Dirk Lefeber
Copromotor: Prof. Dr. ir. Patrick Kool

Dankwoord

De laatst neergeschreven woorden van een werk zijn gebruikelijkerwijze voorbehouden voor het begin van de tekst. Dit zijn de woorden van dank en appreciatie. Dit werk is er maar gekomen dank zij de hulp en steun van vele mensen, direct en indirect. Mijn speciale dank gaat uit naar

- mijn ouders en zussen, voor hun onafgebroken morele steun en waardering,
- prof. Marc Van Overmeire, voor het bieden van de mogelijkheid een doctoraatsstudie aan te vatten toen hij me ettelijke jaren geleden aanwierf,
- de promotoren, prof. Dirk Lefebber en prof. Patrick Kool, voor de technisch-wetenschappelijke ondersteuning, de kostbare begeleiding en het gestelde vertrouwen,
- André Plasschaert, Walter Van Praet, Jean-Paul Schepens en Frans Boulpaep, bij wie ik technische hulp, ideeën en inzichten zocht en vond,
- Krista Sergeant, voor haar hulp bij de afwerking van de scriptie en het organiseren van beide verdedigingen,
- Björn Verrelst, voor de hulp bij de laatste fase van dit werk en voor het voortzetten ervan, hetgeen hij volgens mij uitstekend zal doen,
- Peter Verboven, voor het gebruik van boeken en radio,
- Thierry Lenoir, voor de informatica-ondersteuning.

Vele huidige en vroegere collega's zijn hier niet met naam genoemd, ook hen bedank ik voor alle hulp die ze me gaven. Vrienden en vriendinnen hebben mij meer steun gegeven dan zij zelf waarschijnlijk beseffen, het zijn dikwijls de kleine dingen die het doen.

I'd like to thank Badridin Kharoum for his wise African words which colored many of my evening and weekend hours during the last months. A final word of appreciation is saved for Xianwei Meng whose down-to-earth and yet warm words of advise I will never forget.

Frank Daerden

17 juni 1999

Contents

1	Introduction	1
2	Pneumatic Artificial Muscles: General Study	5
2.1	Definition, Concept and Operation	5
2.2	Review	7
2.2.1	Braided Muscles	8
2.2.2	Netted Muscles	12
2.2.3	Embedded Muscles	15
2.3	Properties	19
2.3.1	Stiffness/Compliance	19
2.3.2	Antagonistic Set-Up	21
2.3.3	Skeletal Muscle Resemblance	23
2.3.4	Performance Data	23
2.3.5	Interaction with Surroundings	24
2.4	Applications	24
2.5	Skeletal Muscle vs. PAM	26
2.5.1	Microscopic Aspects	26
2.5.2	Macroscopic Aspects	29
2.5.3	Joint Stiffness Modulation	32
2.6	Summary	33

3	Zero Parallel Stress Pressurized Axisymmetric Membranes	34
3.1	Setting the Goal	34
3.2	Pressurized Axisymmetric Membranes	35
3.3	Zero Parallel Stress Membranes	39
3.3.1	Analytical Solution	40
3.3.2	Numerical Solution	45
3.3.3	Characteristics	47
3.4	Inelastic Approximation	51
3.5	Maximum Volume Property	57
3.6	Summary	58
4	Pleated Pneumatic Artificial Muscles	59
4.1	Concept	59
4.2	Design	61
4.2.1	Membrane	61
4.2.2	End Fittings	63
4.3	Materials Selection	64
4.3.1	Membrane	64
4.3.2	End Fittings	71
4.4	Assembly	72
4.5	Summary	73
5	Prototype: Design and Characteristics	75
5.1	Membrane Size	76
5.2	End Fitting Sizes	78
5.3	Characteristics	82
5.3.1	Experimental Set-up	83
5.3.2	Traction	84
5.3.3	Diameter	88
5.3.4	Concluding Remarks	89
5.4	Summary	89

6	Antagonistic Rotative Actuator	91
6.1	Brief Description	91
6.2	Linkage Mechanism	92
6.3	Static Actuator Characteristics	96
6.4	Valves	101
6.4.1	General	101
6.4.2	Servo-Valves Characteristics	104
6.5	Compliance/Stiffness	112
6.6	Summary	114
7	Rotative Actuator Control: the Δp-Approach	116
7.1	General Considerations	116
7.2	System Description	117
7.3	Dynamic Characterization	120
7.3.1	Step Test Results	121
7.3.2	System Model	127
7.4	Position Control, Unloaded Case	128
7.4.1	Integral Control	130
7.4.2	Proportional-Integral Control	135
7.4.3	Controller Influence on Compliance/Stiffness	144
7.5	Influence of Inertial Load	145
7.6	Summary	148
8	Conclusions	150
A	Elliptic Integrals of the First and Second Kind	153
B	First Law of Thermodynamics Applied to a Pneumatic Artificial Muscle	156
C	Instrumentation	161
	Nomenclature	167
	Bibliography	171

Chapter 1

Introduction

This dissertation is a study of the development of a new actuator belonging to the class of Pneumatic Artificial Muscles. It concludes a work that started as an assignment to find a suitable engine to power the joints of walking and running machines. This kind of application imposes special requirements on the actuation. Most importantly, it needs to be lightweight because it is carried along by the machine: adding weight to the machine increases system inertia and energy demands. The extra weight is not only due to the extra engine weight but also to its need for a stronger support, which increases the machine's structural weight. Besides the weight constraint the ranges of torque and speed have to be considered. Walking and running is done at low to moderate speeds and high torques. Choosing an actuator that does not show the same ranges will necessitate the use of a transmission, which is better avoided since it introduces undesired phenomena such as backlash, friction and extra inertia to the structure, and makes it bulkier and more complicated to construct and design. A certain level of compliance in order to soften impact shocks and, if possible, to have a partly passive actuation is desirable as well. Naturally, the actuator has to be shock resistant if it is to be used in running machines. Autonomous machine operation, requiring the energy source to be carried along, is a requirement that has not to be fulfilled in a first instance but its possibility needs to be present.

Except for pneumatic cylinders, the classic actuator types were found not to comply. Electromagnetic motors—DC motors, AC motors, stepper motors, linear motors—which are widely used in robotics at present fail on the requirements of weight and direct transmission. Weight is the major drawback of electric motors in this application. Electric motors have power to weight ratios in the order of magnitude of 100 W/kg, although peak values are higher, and their torque to weight ratios range more or less within 1–10 Nm/kg (Isermann

and Raab, 1993; Raab and Isermann, 1990; Hollerberg et al., 1991). Gearing is needed to have high torques at low speeds, although direct drive robots, having their joints directly powered by high performance motors, are being developed.

Hydraulic actuators have a very good power to weight ratio, 2000 W/kg on average according to Raab and Isermann (1990), and high torques at low speeds, but their energy source can leak due to the high operating pressures, typically 20 MPa. They can be directly connected to the robot joints, however. Compliance is not inherent to this type of actuation but it can be introduced by means of servo-valve control.

The most common pneumatic actuators are cylinders. These have power to weight ratios of 400 W/kg according to Raab and Isermann (1990), they can be connected directly to the joint and they operate at moderate levels of speed. Moreover, because of gas compressibility, they have an inherent compliance. Designing an autonomous machine, generating its own pressurized air, is, from a technological point of view, possible (e.g. by an on-board internal combustion engine and compressor). Therefore, they seem appropriate to be used.

There is, however, an alternative kind of pneumatic actuator, known as the Pneumatic Artificial Muscle (PAM), which has a better power to weight ratio than the cylinder. Basically, this is a contractile device operated by pressurized gas. Its core element, the fluid chamber, is a deformable membrane, which is the reason of its low weight. Most of the existing types of PAMs use elastomeric materials for this and, hence, their deformation is based on material elongation. Power to weight ratios of these kinds of actuators exceed values of 1 kW/kg (Caldwell et al., 1993a).

New and more or less specialized actuators, e.g. shape memory alloys and polymeric actuators, are still not sufficiently developed to be used in walking machines, their speeds of operation are very low, with scales of time in the order of tens of seconds (Hollerberg et al., 1991; Caldwell, 1993).

The use of PAMs to power walking and running machines was thus considered and existing types were studied. The most commonly used type, the McKibben Muscle, shows a moderate capacity of contraction, hysteresis as a result of friction between an outer sleeve and its membrane and a threshold behavior. It is therefore difficult to control. Besides this, friction reduces the life span of this actuator. Other types use more or less high tensile stiffness membranes, trapped in a netting and bulging through their meshes. Although friction is largely avoided this way, these types are difficult to build.

This work describes the development of a new PAM, named the Pleated PAM. It uses a high stiffness membrane that is initially folded together and unfurled upon inflation. This leads to a strong reduction in energy losses with regard to the classical types and, hence, develops stronger forces and higher values of

maximum contraction.

A general study of PAMs is given in Chapter 2. It serves as an introduction, dealing with their concept, operation and properties as actuating elements. Existing types and their applications are reviewed. An introduction to the structure and operation of skeletal muscle is included in order to explain the PAM's resemblance to it and to accentuate its extreme complexity.

Chapter 3 provides a rigorous mathematical basis for the Pleated PAM. Its operating principle is based on the lack of stress components in any direction other than its longitudinal axis. This is verified theoretically by considering the membrane's force equilibrium. The static relations of the developed tensile force, of the membrane stress and strain, and of the membrane geometry to the contraction state are established. Influencing parameters to this relationship are the applied gauge pressure, the slenderness of the membrane and its compliance. If the membrane has a very high tensile stiffness, all geometric characteristics are influenced by slenderness only and geometric similarity laws are derived for that case.

The Pleated PAM is formally introduced in Chapter 4. Its pleated or folded membrane arrangement is explained along with its design and materials selection. The proposed design uses cartridge pleating and a lined high tensile stiffness fabric.

The detailed design and the characteristics of a prototype Pleated PAM are treated in Chapter 5. From an initial choice of length and slenderness the static characteristics, as described in Chapter 3, are derived. Together with strength considerations these allow to establish the sizes of all muscle parts. Results of static tests performed on this prototype muscle, measuring force and diameter as a function of contraction and gauge pressure, are discussed. An excellent agreement between these data and the values predicted by the mathematical model derived in Chapter 2 is found.

Chapter 6 describes an antagonistic rotative actuator, which is, basically, a revolute joint that is powered by two of the prototype Pleated PAMs. A tendon drive is chosen to transmit motion and force from the muscles to the joint. The actuator's static characteristics are derived from the prototype muscle and joint drive characteristics. The drive is designed such as to have a linear torque to angular displacement relationship, which will simplify its control. This relationship is confirmed experimentally. Torques are furthermore proportional to the applied muscle gauge pressures and, therefore, muscle pressures determine the equilibrium position of the actuator. An important part of the actuator are the pneumatic valves, since they distribute the pneumatic power to the muscles. Several pressure regulating servo-valve types have been tried and results of dynamic pressure setting tests are discussed.

A procedure to allow the application of linear control techniques is discussed in Chapter 7. This is referred to as the Δp -approach because it is based on controlling the pressure difference between both muscles while keeping the sum of their gauge pressures at a constant level. It is made possible because of the linear torque to rotation relation and because of the dynamic behavior of the used servo-valve. A proportional-integral positioning control law is examined and a way of controlling the actuator compliance is proposed.

The Pleated PAM has been developed in order to satisfy the conditions cited earlier—lightweight, high values of torques at low and moderate speeds, direct joint connection, natural compliance, shock resistance, possible autonomous operation—it can be said this has led to the development of a new actuator instead. Other appropriate actuators, belonging to the same family, show some drawbacks that are avoided by the design of the Pleated PAM.

The developed actuator has more potential than to power walking and running machines alone. Other possible applications that can be cited are: powering a robot arm operating in situations where a delicate interaction between the machine and its surroundings is necessary; accurate positioning operations; powering lightweight robot arms carrying a relatively high payload; actuating grippers with an adjustable firmness. Using electric actuation for these applications is difficult and for some even impossible. Pleated PAM's, on the other hand, are inherently suited for these.

Chapter 2

Pneumatic Artificial Muscles: General Study

2.1 Definition, Concept and Operation

A Pneumatic Artificial Muscle is a contractile and linear motion engine operated by gas pressure. Its concept is a very simple one: the actuator's core element is a flexible reinforced closed membrane (shell, diaphragm) attached at both ends to fittings (end fittings, closures, clamps) along which mechanical power is transferred to a load. As the membrane is inflated or gas is sucked out of it, it bulges outward or is squeezed, respectively. Together with this radial expansion or contraction, the shell contracts axially and thereby exerts a pulling force on its load. The force (tension, load) and motion thus generated by this type of actuator are linear and unidirectional. This contractile operation distinguishes the PAM from bellows, which extend upon inflation.

Throughout literature different names are found for PAMs: Pneumatic Muscle Actuator (Caldwell et al., 1993a), Fluid Actuator (Yarlott, 1972), Fluid-Driven Tension Actuator (Paynter, 1988b), Axially Contractible Actuator (Immega and Kukulj, 1990; Kukulj, 1988), Tension Actuator (Immega, 1989; Paynter, 1988a).

A PAM's energy source is gas, usually air, which is either forced into it or extracted out of it. This way the actuator is powered by the pressure difference of the inside gas with regard to the surroundings. Although it is possible to design an underpressure operating muscle (Marcinčin and Palko, 1993; Morin, 1953), PAMs usually operate at an overpressure: generating and supplying compressed gas is easier to accomplish and, with ambient pressure mostly at about 100 kPa, a lot more energy can be conveyed by overpressure than by underpressure. Charging an overpressure PAM with pressurized gas enables it to move a

load, discharging it, conversely, makes it yield to a load.

From the latter property one can deduce the length to load relation. During a time interval dt energy is fed to the muscle, which is at a gauge pressure of $p = P - P_0$ relative to the ambient pressure, by forcing an infinitesimal mass dm of gas into it. Thereby, the membrane's volume increases by dV and a net amount of work

$$dW_m = p dV \quad (2.1)$$

crosses its boundary (which is taken bordering the inside surface of the diaphragm, so it encompasses the gas inside the muscle but not the diaphragm itself). During the same period dt , the actuator's length changes by dl (< 0 for shortening) and a load F is displaced over the same distance, requiring an amount of work

$$dW_l = -F dl \quad (2.2)$$

Also, the membrane's material is deformed, requiring dW_d . Estimating this depends on material behavior laws—e.g. elastic, plastic, visco-elastic. Disregarding work to deform the membrane and assuming quasi-static conditions, dW_l and dW_m equal out, leading to the fundamental expression of the ideal load to length relation:

$$F = -p \frac{dV}{dl} \quad (2.3)$$

In reality, however, dW_d cannot usually be disregarded and the developed force will have a lower value. Part of F is needed to compensate the inertia of the diaphragm's moving parts, but, as these have a very low mass, this is negligible. Comparing the PAM force-length expression to that of pneumatic cylinders, Paynter (1988b) defined $(-dV/dl)$ as the actuator's 'effective area'.

Eq. 2.3 shows how the generated force depends on gauge pressure and on change of volume with regard to length. As the evolution of volume to length is dependent on the type of membrane that is used, especially its geometry and the way it inflates, the contractile state of a PAM is determined by its length and gauge pressure. Whatever the type, since contraction happens as a natural consequence of inflation, volume will be increasing with decreasing length and therefore force will increase with length. Although theoretically not necessary, for all of the existing PAMs, to the author's knowledge, it is a monotonically increasing function. Fig. 2.1 roughly outlines the operation of a PAM of an arbitrary type and shape kept at constant pressure. Theoretically, some types can have an infinitely high force at their longest state—which will be shown to be the case for the one that is the subject of this work—but due to material

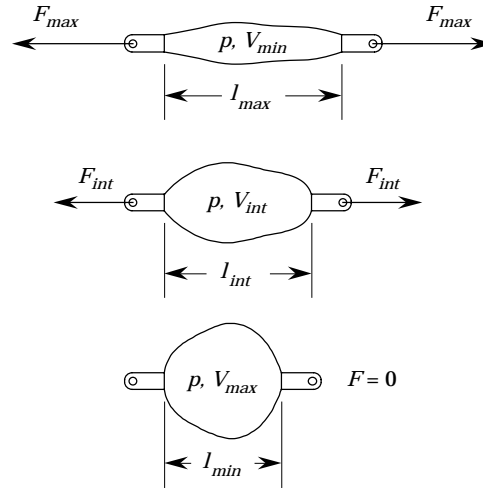


Figure 2.1: Arbitrary PAM.

yielding this will never be so in practice. As contraction increases, the volume will increase towards a maximum level, at which point force will have dropped to zero and contraction will have reached its maximum value. Further shortening of the muscle can only be done by compressing it, reversing the sign of force and, hence, making it act as a bellows.

The equilibrium load at a certain state can also be deduced from a more elaborate calculation of membrane stresses—such a calculation will be performed in Chapter 3 for the type of muscle proposed in this work. These stresses, which are purely tensile, are in fact the transmission of force from internal pressure to external load. As they can grow very large, especially at low contraction, an adequate reinforcing, usually fiber reinforcement, of the membrane is needed. This can be done externally, by a sleeving embracing the membrane or internally, by embedding the fibers into it.

2.2 Review

Ever since their first conceiving, which according to Marcinčin and Palko (1993) was in 1930 by a Russian inventor named S. Garasiev, fluid-driven muscle-like actuators of a number of kinds have been developed. They can be distinguished, according to their design and operation:

- pneumatic or hydraulic operation;

- overpressure or underpressure operation;
- braided/netted or embedded membrane;
- stretching membrane or rearranging membrane.

Hydraulic operation is taken into consideration for completeness' sake. The key attribute of these artificial muscles is their inflation and deformation. Due to the flexibility needed for this and, consequently, the limited material strength, the pressure difference across the shell needs to be limited. Typical maximum values range at about 500 kPa to 800 kPa. At these values hydraulic operation suffers from a bad power to weight ratio, making it not very attractive. The third characteristic refers to the tension carrying element of the muscle: a structure either embracing the membrane or embedded in the membrane. The last characteristic refers to the manner in which the membrane inflates: to be able to expand radially, either the membrane material has to stretch radially or the radial section has to change by rearranging the membrane's surface. In case of pure rearranging, the total membrane surface is constant regardless of contraction and volume. This allows for a greater tension to be developed as no energy is put into stretching membrane material.

This review will be done according to the third of the above cited points of classification. Three classes will be discriminated: braided muscles, netted muscles and embedded muscles. Each type will be reviewed according to the amount of information available in literature.

2.2.1 Braided Muscles

Braided muscles are composed of a gas-tight elastic tube or bladder surrounded by a braided sleeving (weave, braid, sleeve) as is shown in Fig. 2.2 for a special kind of this type of muscle. The braid fibers run helically about the muscle's long axis at an angle (pitch angle, braid angle, weave angle) of $+\theta$ and $-\theta$. When pressurized the tube presses laterally against the sleeve. Thereby the internal pressure is balanced by braid fiber tension due to fiber curvature about the tube. Fiber tension is integrated at the braid's end points to balance an external load. As the pressing contact between tube and sleeving is absolutely necessary to convey load, braided muscles cannot operate at underpressure: passing through the meshes of the braid, surrounding gas would only act on the tube that, consequently, would be squeezed without transferring a noticeable amount of work to the clamps.

This type of muscle was derived from a patented design by Morin (1953), who actually embedded the fibers into a rubber diaphragm. According to Baldwin (1969), J. L. McKibben introduced it as an orthotic actuator in the late

1950's: due to the similarity in length-load curves between this artificial muscle and skeletal muscle, it seemed an ideal choice for this purpose (Schulte, 1961; Gavrilović and Marić, 1969). However, practical problems, such as pneumatic power storage or availability and poor quality valve technology at that time, gradually reduced interest from the prosthesis/orthotics community in McKibben's muscles. In the late 1980's it was reintroduced by Bridgestone Co. in Japan as the Rubbertuator (Inoue, 1987), and used to power an industrial use robot arm, Soft Arm. Since then several research groups have been using this type of PAM to power robots, mainly of anthropomorphic design, and prostheses and orthotics (Hannaford et al., 1995; Greenhill, 1993; Caldwell et al., 1995, 1998; Grodski and Immega, 1988; Hesselroth et al., 1994; Winters, 1995).

The general behavior of these muscles with regard to shape, contraction and tension when inflated will depend on the geometry of the inner elastic part and of the braid at rest (meaning neither pressurized nor loaded), and on the materials used. Usually, braided muscles have a cylindrical shape because of a cylindrical bladder and a constant pitch angle throughout the braid. Two basic types of braided muscles can be distinguished: one that has both its inner tube and braid connected to fittings at both ends and another that only has the braid connected to end fittings and whose inner tube is an unattached bladder. The former type is generally referred to as the McKibben Muscle. The latter has no particular name so, for sake of clearness, it will be referred to as the Sleeved Bladder Muscle.

McKibben Muscle

The type of pneumatic artificial muscle most frequently used and published about at present is the McKibben Muscle. It is a cylindrical braided muscle that has both its tube and its sleeving connected at both ends to fittings that not only transfer fiber tension but also serve as gas closure. Typical materials used are latex and silicone rubber and Nylon fibers. Fig. 2.2 shows its structure and operation.

By changing its pitch angle the braid changes its length and diameter. Notating l_s as the length of each thread of the braid, n the amount of encirclements each strand makes about the tube, one can easily deduce the volume enclosed by the diaphragm:

$$V = \frac{l_s^3}{4\pi n^2} \cos \theta \sin^2 \theta \quad (2.4)$$

Maximum volume is thus attained at a weave angle of about 54.7° . Increasing the angle beyond this value is only possible by axially compressing the muscle. This is not a stable process: the flexible muscle shell has no flexural stiffness

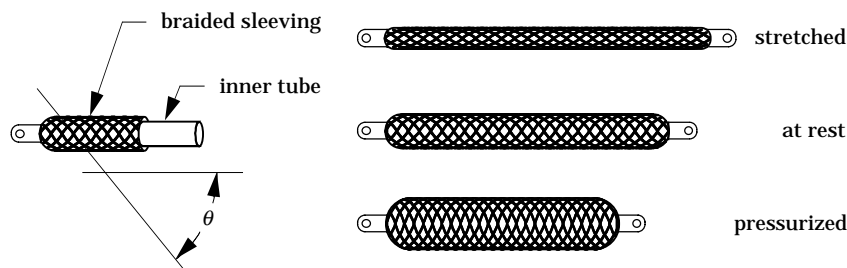


Figure 2.2: McKibben type muscle.

and thus it would easily buckle. Therefore this will not be considered. When stretching, the pitch angle decreases to a lower limit, which is determined by fiber thickness, the amount or density of fibers, the number of encirclements and the diameter of the end fittings. Typical values of pitch angles, given by Caldwell et al. (1995), are 59.3° for the maximum inflation state and 20.0° for the fully stretched state.

Tension can be related to weave angle (Schulte, 1961; Chou and Hannaford, 1996) using Eq. 2.3:

$$F = \frac{\pi D_{max}^2 p}{4} (3 \cos^2 \theta - 1) \quad (2.5)$$

with D_{max} the muscle's diameter at a braid angle of 90° , which is the limiting case. Defining contraction as $\epsilon = 1 - l/l_0$ where l stands for muscle actual length and l_0 muscle length at rest, tension can also be related to contraction (Tondu et al., 1995; Inoue, 1987):

$$F = \frac{\pi D_0^2 p}{4} \left(\frac{3}{\tan^2 \theta_0} (1 - \epsilon)^2 - \frac{1}{\sin^2 \theta_0} \right) \quad (2.6)$$

with D_0 and θ_0 the diameter and the weave angle at rest, respectively. The rest state is determined by the original tube size and braid characteristics. Elongation beyond the rest size is possible, as stated before, until the minimum pitch angle is reached. The range of contraction-extension depends on the lower pitch angle limit and, consequently, on the density of strands in the weave and on their thickness. Chou and Hannaford (1996) report ranges of 0.75-1.1 of initial length for Nylon fiber McKibben Muscles, 0.86-1.14 for fiberglass McKibben Muscles and 0.79-1.02 for the Rubbertuator—which is in accordance with Inoue (1987).

The tension expressions can be expanded to take into account friction—between sleeving strands and tube and between the strands themselves—and deformation of the inner tube (Schulte, 1961; Chou and Hannaford, 1996). Friction and

non-elastic deformation of the diaphragm will show up as hysteresis and threshold pressure (i.e. the pressure difference to overcome in order to start radial diaphragm deformation), while elastic lateral deformation will lower tension. The force needed to elongate or compress the tube with regard to its rest length can be modelled as a passive spring force acting in parallel with the active force calculated by Eq. 2.3. This passive force will increase tension at $l > l_0$ and lower it at $l < l_0$.

Chou and Hannaford (1996) report a threshold pressure of 90 kPa, hysteresis width of 0.2–0.5 cm and height of 5–10 N for a Nylon braid muscle of 14 cm rest length and 1.1 cm rest diameter and more or less double these figures for an approximately equal sized fiberglass braid muscle (cf. Fig. 2.3). They also show hysteresis to be substantially due to dry friction. Caldwell et al. (1993b) report forces attaining only 53% of their values predicted by Eq. 2.3. The typical operating gauge pressure range of McKibben Muscles is 100–500 kPa. The maximum allowable gauge pressure is determined by the strength of the tube: too high a pressure would make the tube bulge through the meshes of the net and it would subsequently burst. The higher this pressure the more energy can be transferred, but equally the higher the pressure threshold value because of the increasing toughness of the diaphragm. As a result of this, low forces cannot be generated.

As for power to weight ratios of McKibben Muscles, values cited by Cald-

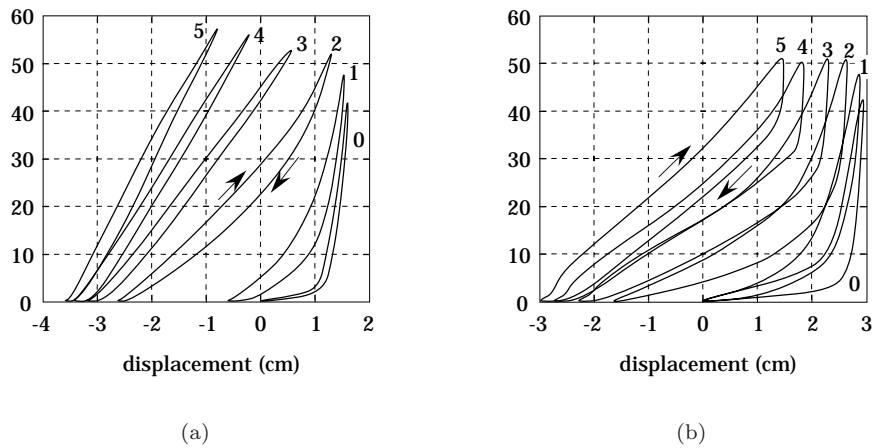


Figure 2.3: McKibben Muscle tension (N) and hysteresis at isobaric conditions (0, 100, 200, 300, 400 and 500 kPa), (a) Nylon braid, (b) fiberglass braid. (Chou and Hannaford, 1996)

well et al. (1993b) range from 1.5 kW/kg at 200 kPa and 3 kW/kg at 400 kPa. Hannaford et al. (1995) cite a value of 5 kW/kg and Hannaford and Winters (1990) even 10 kW/kg. To determine these values, no auxiliary elements such as valves, were taken into consideration. The weight of McKibben Muscles is typically about 50 g (Tondu et al. (1995), $l_0 = 34$ cm, $D_0 = 1.4$ cm), but can be as low as 5.5 g (Caldwell et al. (1993a), $l_0 = 9$ cm, $D_0 = 1$ cm).

As mentioned earlier, this type of muscle is the most frequently encountered one to date. The main reason for this seems to be its simple design, ease of assembly and low cost. On the other hand life expectancy of this muscle, of which no written reports were found, seems not very high. Users complain about early braid fiber failure at the point of clamping. A major disadvantage of the McKibben Muscle is its inherent dry friction and threshold pressure. Due to friction temperature effects influence muscle operation: warm muscles behave different from cold ones (Caldwell et al., 1995). Hesselroth et al. (1994) report a positional drift of the Rubbertuator that occurs when the actuator pressure is oscillating about a fixed value.

PAM designs that are closely related to the McKibben design can be found in Greenhill (1993), who calls it the Digit Muscle, and in patents Woods (1957) and Beullens (1989).

Sleeved Bladder Muscle

This type differs from the McKibben type in the design of the inner bladder: it is not connected to the sleeving. This means that no passive spring force is added to or subtracted from muscle tension. Instead, the diaphragm will have deformation energy stored at every state of contraction, decreasing the attainable muscle tension. Winters (1995), whose McKibben-like muscles simply consist of a bladder surrounded by a braid directly attached to tendon-like cords, reports motion ranges of 5–30% shortening and less than 10–20% lengthening depending on pitch angle at rest. The main advantage of this PAM is its extreme ease of assembly. A Sleeved Bladder Muscle is also subject of the patent of Beullens (1989).

2.2.2 Netted Muscles

The difference between braided and netted muscles is the density of the network surrounding the membrane, a net being a mesh with relatively large holes and a braid being tightly woven. Because of this, if the membrane is of the stretching kind, it will only withstand low pressures. Therefore this type of fluid actuator will usually have a diaphragm of the rearranging kind.

Yarlott

This type of fluid muscle is disclosed in a US patent by Yarlott (1972). It comprises an elastomeric bladder of a prolate spheroidal shape netted by a series of cords or strands that run axially from end to end. The bladder is radially reinforced by strands to resist elastic expansion. This can also be done by a single cord wound helically about the shell as shown in Fig. 2.4. In its fully inflated state, this actuator takes the spheroid bladder shape. When elongated, the axial strands straighten out and push the bladder into a shape characterized by a series of ridges and valleys as can be seen from the front view in Fig. 2.4. The shell's surface area remains more or less constant and a surface rearranging ensues on inflating. As shell stretching is thus reduced, more pneumatic energy can be transformed into mechanical power. If completely elongated, the axial strands will be fully straightened and pressurization would then lead to an infinitely high tension. However, due to strand material yielding this will not be attained. Apparently, Yarlott designed this muscle to operate at low gauge pressures—a value as low as 1.7 kPa is cited.

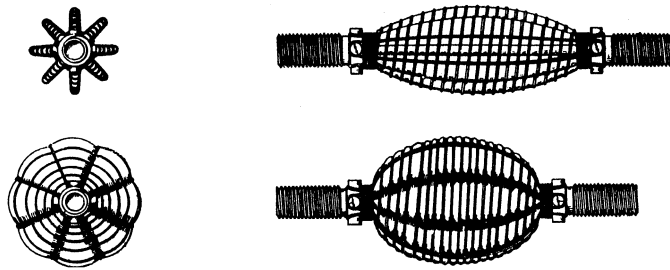


Figure 2.4: Yarlott Muscle. (Yarlott, 1972)

ROMAC

This RObotic Muscle ACTuator was designed by G. Immega and M. Kukulj in 1986. It is the object of a US patent (Immega and Kukulj, 1990) and is treated briefly in Immega (1986, 1987). It consists of an articulating polylobe bladder harnessed by a wire netting and closed at either ends by fittings, as is shown in Fig. 2.5(a). The bladder is made of a sheath, that is characterized by its high tensile stiffness, its flexibility and its fluid-tightness (e.g. impregnated para-aramid fiber fabric). The netting or harness is comprised of non-stretchable flexible tension links which are joined at nodes so as to form four-sided diamond shaped apertures in the network, as shown in Fig. 2.5(a). The harness expands

radially and contracts axially, thereby changing the base of each protruding lobe. As a result of this mechanism the enclosed volume changes. The total surface of this actuator is constant regardless of contraction-elongation due to the tensile stiffness of the membrane material. Each base side of a protrusion or lobe is connected to a base side of an adjacent lobe by a flexible seam or continuous fold running underneath a wire element. Due to the absence of friction and membrane stretching, a much higher force and nearly negligible hysteresis is attained compared to muscles of the stretching membrane type.

Two versions of ROMAC are made: a standard one, having lengths of 6–30 cm and a miniature one, having lengths of 1–6 cm. The miniature version and also low pressure operating standard versions do not, in effect, need to be harnessed. For standard sizes, muscle forces of 4500 N to 13600 N at gauge pressures of

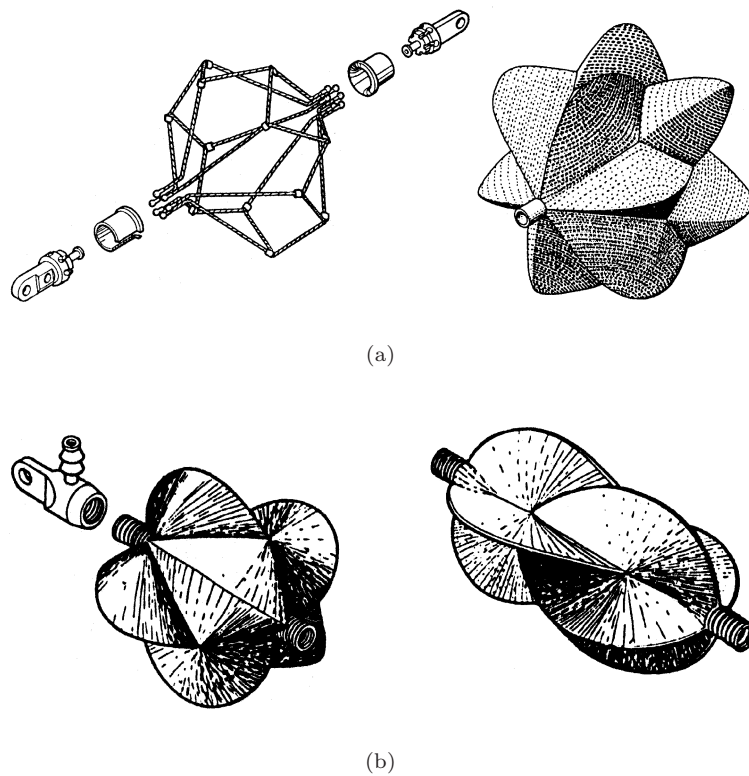


Figure 2.5: ROMAC, standard version (a) and miniature version (b). (Im-mega, 1986)

700 kPa, and maximum contractions of up to 50% are cited.

Kukolj

This type of actuator, which is described in a US patent by Kukolj (1988), is in its basic embodiment a variation of the McKibben Muscle. The main difference between them is the sleeve: McKibben Muscles have a tightly woven braid while the Kukolj design uses an open-meshed net. In its non-loaded condition, there is a gap between the net and the membrane, which only disappears at a suitably high extending load. The condition of non-pressurization and load, such that the net fits the diaphragm, is the fully extended condition. The reason for the gap, mentioned by the inventor, is the tendency of the network to contract faster than the membrane, resulting in buckling of the latter near its ends. The initial stretch prevents this from happening. Fig. 2.6 shows the Kukolj Muscle in its uninflated, non-loaded condition, and in a set-up, lifting a weight mounted hanging from a hinged arm, showing the actuator in fully stretched and intermediate inflation conditions.

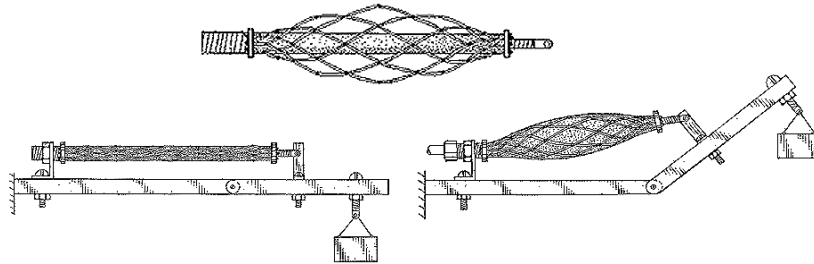


Figure 2.6: Kukolj Muscle. (Kukolj, 1988)

2.2.3 Embedded Muscles

As mentioned earlier, the load carrying structure of this type of fluid muscles is embedded in its membrane. Among this type figure several designs, most of which will be referred to by their inventor's name.

Morin Muscle

This early design of fluid muscle, described in Morin (1953), had for its object

an elastic diaphragm adapted to be subjected to the pressure of any fluid and adapted to transmit any change in the pressure of said fluid to a controlling device, such as measuring instruments, valves and similar devices.

With this in mind one cannot really call it an artificial muscle but, as it has the same principle of operation and is the origin for McKibben's design, it is included in this review.

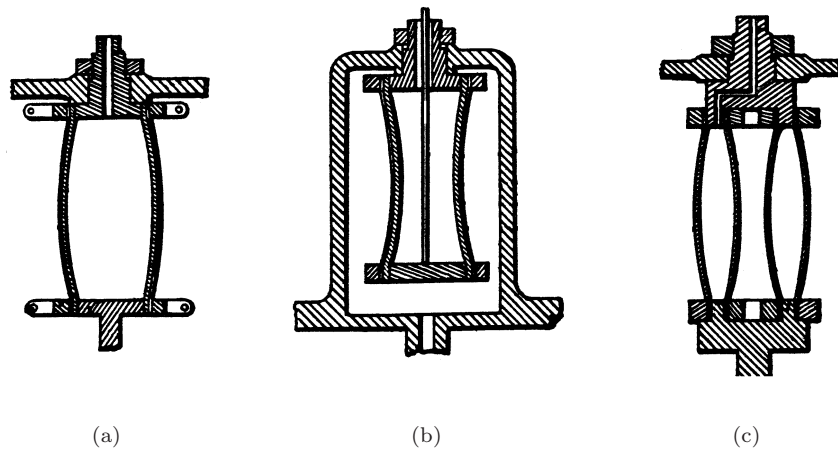


Figure 2.7: Morin Muscle designs. (Morin, 1953)

In this design a rubber tube is embedded by threads of a high tensile stiffness. These threads can be directed along the actuator's long axis or in a double helix about that axis. As fiber material Morin cites cotton, rayon, asbestos or steel; a choice that is clearly marked by that time. The two-phase membrane is clamped by two end fittings, serving to seal and to attach load. Full tensional load is taken by the fibers while the elastomer stretches to allow for inflation. Possible operating fluids suggested by Morin are compressed air, water, oil or even steam. In his patent he proposes three designs having different ways of operation regarding pressure: an overpressure design as shown in a longitudinal cross-section in Fig. 2.7(a), an underpressure design, Fig. 2.7(b), and a concentric membranes design, Fig. 2.7(c). In the underpressure design the diaphragm is housed inside a vessel. The diaphragm is at ambient pressure while the vessel is pressurized. Power is transduced via a rod attached to the lower diaphragm end fitting and sliding through an orifice in the upper end fitting.

Typical operating pressures or other characteristics are not mentioned.

Baldwin Muscle

This type of muscle (Baldwin, 1969) is based on the design of Morin. It consists of an elastomeric membrane, a very thin surgical rubber, embedded by glass filaments in the axial direction. The resulting membrane has a modulus of elasticity in the fiber direction that is much higher than that in the direction perpendicular to the fibers. Fig. 2.8 sketches this type of muscle.

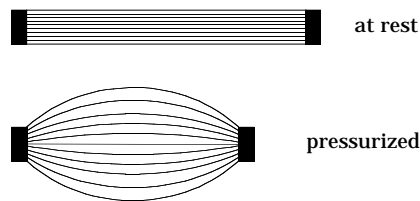


Figure 2.8: Baldwin type muscle.

Due to the absence of friction and the very thin membrane, this muscle shows less hysteresis and a very low threshold pressure compared to braided muscles but, as radial expansion is quite high, gauge pressures have to be limited to low values, typically 10–100 kPa. Baldwin (1969) cites forces of up to 1600 N at these low pressures. Life tests which consisted of the continuously lifting and lowering of a weight of 45 kg at a gauge pressure of about 100 kPa indicated an operating life of some 10000 to 30000 cycles. A similar but earlier design, developed by K. Nazarczuk in 1964 at the Warsaw Polytechnic, is mentioned in Marcinčin and Palko (1993).

UPAM

The UPAM, which stands for UnderPressure Artificial Muscle, has in fact a similar design as the Morin type showed in Fig. 2.7(b). It is described very superficially in Marcinčin and Palko (1993); Marcinčin and Smrček (1994a,b); Marcinčin et al. (1995); Smrček et al. (1995). As gas is sucked out of the membrane it collapses in a non-axisymmetrical way, i.e. it is squeezed and flattened in the middle. Contractions of 20% for muscles of a maximum diameter of 50 mm and length of 100 mm are mentioned. Since contraction stops when the membrane sides touch, these actuators have to be designed quite thick in order to obtain reasonable values for maximum contraction. Forces vary between 20 N and 140 N, but it is not mentioned at what underpressure. These values are rather low because of the maximum pressure difference of 100 kPa with regard to ambient conditions.

Paynter Knitted Muscle

This design is the object of a US patent by Paynter (1988a). The actuator has a spherical bladder that is reinforced by a knitted structure of strong, tough and flexible fibers. It is made to have the same spherical shape as the bladder so that it conforms to it and can be easily bonded to it. The bladder is made of an elastomeric material. During inflation the bladder does not stretch as is the case for McKibben Muscles. When fully inflated the muscle takes on the shape of the original bladder and knitting sphere. If extended from thereon, it will gradually take on a fluted shape. Unpressurized, the muscle can be extended to a length equalling half the circumference of the sphere. Therefore, maximum contraction with regard to this fully extended state is 36.3%. Operating gauge pressures can be as high as 800 kPa. Life expectancy is mentioned to be “many hundreds of thousands of cycles”.

Paynter Hyperboloid Muscle

An alternative design by Paynter, also described in a US patent by Paynter (1988b), concerns a type of muscle whose membrane, in its fully elongated state, has the shape of a hyperboloid of revolution. The elastomeric membrane is embedded by a sleeve of inextensible, flexible threads that are anchored to the end fittings. With the actuator at its longest, these threads run in straight lines from end to end, thus defining the hyperboloid surface. A set of strands runs in one sense about the axis, an equal amount of strands run in the opposite sense. Fig. 2.9(a) shows a section of this type of muscle. When inflated, the membrane bulges into a nearly spherical surface at full contraction, as shown in Fig. 2.9(b).

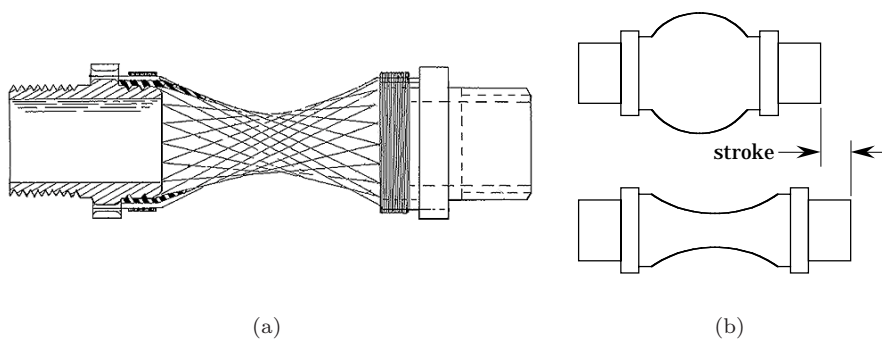


Figure 2.9: Paynter Hyperboloid Muscle. (Paynter, 1988b)

Paynter (1988b) cites metal wires, cord, polyester fibers and para-aramid fibers as possible strand materials. For the membrane he suggests neoprene rubber or polyurethane. The muscle can be powered both pneumatically or hydraulically. The maximum bulging diameter is about two times the end fittings diameter, while tension is proportional to the square of this value. A maximum contraction or stroke of about 25% and tensions of some 500 N at 200 kPa at zero contraction are mentioned for a muscle 2.5 cm long and of 1.25 cm end fitting diameter.

Kleinwachter

Kleinwachter and Geerk (1972) describe in their US patent how the inflatable membrane technique can be used in designing a torsional device, which they refer to as torsion muscle. It is shown in Fig. 2.10. It has a toroid diaphragm attached at its outer edge to a ring shaped structure and at its inner edge to a shaft. The diaphragm is embedded with stiffening filaments that run obliquely across the radial direction from the outer structure to the shaft. When inflated the membrane bulges and the filaments thereby rotate the shaft in the direction of φ , as indicated on the figure. One-way rotation and torque are thus achieved.

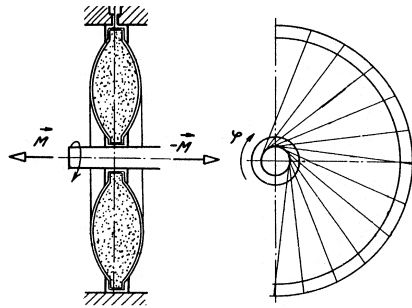


Figure 2.10: Kleinwachter torsion device.

2.3 Properties

2.3.1 Stiffness/Compliance

Due to gas compressibility all pneumatic actuators show a natural compliance. Besides this, PAMS also have their varying effective area. Compliance, C , which

is defined as the inverse of stiffness, can be deduced from the basic PAM tension equation, Eq. 2.3:

$$C^{-1} = K = \frac{dF}{dl} = -\frac{dp}{dV} \left(\frac{dV}{dl} \right)^2 - p \frac{d^2V}{dl^2} \quad (2.7)$$

Both terms of the right-hand side have the same sign as dl : elongating a muscle causes muscle tension to increase.

If the actuator is closed, the first term can be directly related to gas compressibility, which is defined as (Moran and Shapiro, 1992)

$$\chi = \frac{1}{\rho} \frac{d\rho}{dp} = -\frac{1}{V} \frac{dV}{dp} \quad (2.8)$$

It can be estimated depending on the thermodynamic processes going on within the system boundaries (which, as defined in §2.1, include only the gas inside the membrane). Usually a perfect gas approximation and polytropic change of state is taken:

$$\frac{dP}{dV} = -n \frac{P}{V} \quad (2.9)$$

with the exponent n ranging between 1.0 (isothermal changes of state) and 1.4 (isentropic changes) when dealing with dry air. Compressibility can then be written as

$$\chi = \frac{1}{nP} \quad (2.10)$$

As an example value, the isothermal compressibility of dry air at atmospheric conditions is 10^{-5} Pa^{-1} . Compared to that of liquids, this is quite a high value: the isothermal compressibility of water at 20°C is $4.59 \times 10^{-10} \text{ Pa}^{-1}$ (Moran and Shapiro, 1992) and for mineral oil $6.67 \times 10^{-10} \text{ Pa}^{-1}$ (Ebertshäuser, 1989).

For an open actuator the situation is more complex. The change of pressure with volume is not only determined by compressibility but also by the mass flow in or out of the volume. If fast pressure controlling valves are used, isobaric conditions can be maintained, thus eliminating compressibility effects.

The second term typifies muscle actuators: it expresses muscle stiffness at isobaric conditions and is attributed purely to the variation of the effective area. If the pressure regulation of the muscle is fast enough, only this term will determine compliance. It is clear from Eqs. 2.7 and 2.9 that an increase in pressure, increases stiffness and diminishes compliance.

2.3.2 Antagonistic Set-Up

Since PAMs are one-way acting, two are needed to generate bidirectional motion: as one of them moves the load, the other one will act as a brake to stop the load at its desired position. To move the load in the opposite direction the muscles change function. This opposite connection of the muscles to the load is generally referred to as an antagonistic set-up: the driving muscle is called the flexor or agonist, while the brake muscle is referred to as the extensor or antagonist. The antagonistic coupling can be used for either linear or rotational motion, as is shown in Fig. 2.11.

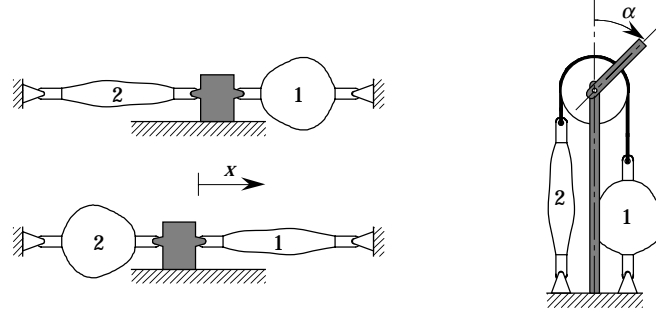


Figure 2.11: Antagonistic set-up.

In this set-up the equilibrium position of the load, in the absence of any outer force or force field, will be determined by the ratio of both muscle gauge pressures. This is a direct consequence of the actuator's varying effective area, as can be seen from Eq. 2.3. If the load is at its equilibrium position and both pressures are equal, the diaphragms are at lengths l_{10} and l_{20} . Changing the pressures will break the equilibrium and thus a net force will move the load until a new point of equilibrium is reached at a distance x from the previous one. Notating dV_i/dl_i as $f_i(l_i)$, Eq. 2.3 can be rewritten for each muscle:

$$F_1 = -p_1 f_1(l_{10} - x) \quad F_2 = -p_2 f_2(l_{20} + x) \quad (2.11)$$

with individual muscle lengths at $l_1 = l_{10} - x$ and $l_2 = l_{20} + x$. Expressing force equilibrium then yields x as a function of the gauge pressure ratio. This can also be readily seen from the graph in Fig. 2.12, which shows the force characteristics of the muscle pair shown in Fig. 2.11. Muscle (1) is at a gauge pressure p while the pressure of muscle (2) varies. As the muscle pressure changes, the force graph of that muscle is scaled accordingly and the equilibrium will move to the new intersecting point of the graphs. A uniform scaling of both gauge pressures

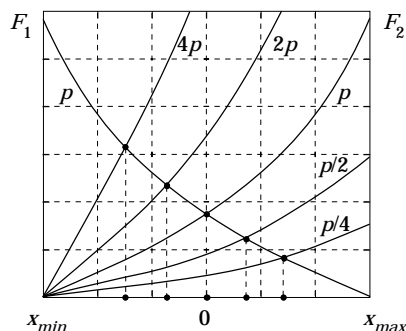


Figure 2.12: Equilibrium position as a function of gauge pressure ratio.

will not influence the equilibrium and thus only the ratio of gauge pressures will determine the equilibrium position.

Using two one-way pneumatic cylinders instead of PAMs, the equilibrium position would not be determined by the gauge pressure ratio. Instead, at all positions, these ratios would be the same because of the constant piston areas. Position would then be determined by the mass of fluid inside each cylinder. This is a major difference between PAMs and pneumatic cylinders: position control using two antagonistically set up pneumatic cylinders is done by mass flow control, using fluid muscles it is done by pressure control.

It is interesting to examine what compliance or stiffness in an antagonistic set-up, co-activating both muscles (cf. Fig. 2.11), will be. Assume for this purpose both muscles identical and at length l_0 when equally pressurized. The net force acting on the load at any given position x is

$$F = F_1 - F_2 = -p_1 \frac{dV_1}{dl_1} + p_2 \frac{dV_2}{dl_2} = p_1 \frac{dV_1}{dx} + p_2 \frac{dV_2}{dx} \quad (2.12)$$

Stiffness can then be put as

$$K = -\frac{dF}{dx} = -\frac{dp_1}{dV_1} \left(\frac{dV_1}{dx} \right)^2 - \frac{dp_2}{dV_2} \left(\frac{dV_2}{dx} \right)^2 - p_1 \frac{d^2V_1}{dx^2} - p_2 \frac{d^2V_2}{dx^2} \quad (2.13)$$

All terms in this expression are positive indicating the restoring nature of muscle forces. In fact, the flexor-extensor coupling of muscles to a load can be compared to a (generally non-linear) spring-mass system, whose stiffness characteristic can be controlled by regulating muscle pressures. As position is determined by gauge pressure ratio, Eq. 2.13 shows that stiffness and compliance can be controlled independently of position by setting the sum of the pressures while keeping their ratio fixed: the higher this sum, the stiffer the actuator.

2.3.3 Skeletal Muscle Resemblance

PAMs resemble skeletal muscle insofar that both are linear contractile engines having a monotonically decreasing load-contraction relation (although this not always the case for skeletal muscle). Both have to be set up antagonistically in order to get bidirectional motion and both are able to control joint compliance. A lot of differences, however, exist: skeletal muscles

- do not change volume during contraction (McMahon, 1984, Chapter 1);
- have a modular structure, they are a vast parallel and series connection of microscopic contractile systems;
- are organized in units whose activation depends on the level of external load;
- come in fast and slow types, depending on the need of sustained action and speed;
- have integrated multiple force and strain sensors;
- have energy stored in them and running through them;
- can serve as energy source or even building material for muscles of other biological systems, in other words, they are comestible.

The latter distinctive feature is perhaps the most extraordinary: one biological system can disintegrate another one's actuators down to the molecular level and use this to power or build its own actuators. The structure, operation and properties of skeletal muscle will be described in more detail in §2.5.

2.3.4 Performance Data

Force generation is not typified by a single figure as force varies with contraction. Theoretically it can even tend to infinity at the onset of contraction. However, some typical values can be given:

- McKibben Muscle (Tondu et al., 1995): 650 N at rest length, 300 N at 15% contraction and zero at 30% contraction, all at a gauge pressure of 300 kPa, for a muscle of 150 mm rest length, 14 mm rest diameter and a weight of 50 g;
- Rubbertuator (Inoue, 1987): 220 N at rest length, 100 N at 10% contraction and zero at 20% contraction, all at a gauge pressure of 300 kPa, for a muscle of 150 mm rest length and a weight of 32 g;

- ROMAC (Immega, 1987): 15000 N at 5% contraction, 6000 N at 25% contraction and zero at 50% contraction, all at a gauge pressure of 700 kPa, for a muscle of 13 cm rest length and a weight of 320 g.

For the type of muscle proposed in this work, 3300 N at 5% contraction, 1300 N at 20% and zero at 43% contraction at 300 kPa for a muscle of 10 cm rest length, 2.5 cm rest diameter and a weight of 100 g are found.

Contraction ranges differ strongly from type to type:

- McKibben: -10% to 25% and -14% to 14% Chou and Hannaford (1996);
- Rubbertuator: -2% to 20% (Inoue, 1987);
- ROMAC: 0% to 50% (Immega, 1986).

The power that can be transmitted by PAMS, as is the case for any kind of pneumatic device, depends strongly on the valves that are used to regulate the flow of gas. Using the valves Kolvenbach KPS 3/4, cf. Appendix C, allows flows of $0.0095 \text{ Std.m}^3/\text{s}$ for a gauge pressure drop of 700 kPa to 300 kPa. Using Eq. 2.1 this implies a transmission of about 0.7 kW at isobaric operation. This is an upper limit, as no losses or other energy consuming effects are considered.

In terms of weight PAMS perform extremely well compared to other types of engines: values ranging in excess of 1 kW/kg (Caldwell et al., 1993a), even up to 10 kW/kg (Hannaford and Winters, 1990) are reported.

2.3.5 Interaction with Surroundings

Finally, concerning its effects on operating surroundings, one can state that as long as an innocuous gas is used, a PAM causes no pollution, hazards, detrimental or harmful effects. As is the case for all pneumatic devices there are no hazards of fire or explosion. Furthermore, because of its intrinsic compliance it is well suited for safe man-machine interaction. Some authors, in this respect, refer to the fluid muscle as having a soft touch (Inoue, 1987).

2.4 Applications

To the author's knowledge, Pneumatic Artificial Muscles have never really been commercially produced, except for the Rubbertuators, which were manufactured and marketed by Bridgestone Co. for some time. At the present, McKibben-like muscles are being brought to the market by Festo Ag. & Co., showing a general renewed interest in these devices. PAMS, at present, are

mainly used as robotic actuators in applications where compliance and low power to weight ratio are important, e.g. walking/running machines or even humanoid robots. Prosthesis/orthotics applications are less frequently seen today as was the case some thirty years ago when Schulte (1961) used it to drive an arm brace. To the author's knowledge only Winters (1995) mentions Sleeved Bladder Muscles as having potential as a suitable power system in prosthetics.

Caldwell et al. (1993a) used 18 small (90 mm long, 10 mm diameter, 5.5 g) McKibben Muscles to power a dexterous four-fingered manipulator, with each finger powered by four muscles, and the thumb by six. Caldwell et al. (1995) report on how to use McKibben Muscles for powering the elbow and wrist of an anthropomorphic arm. Caldwell et al. (1998) and Caldwell et al. (1997) take it one step further to the start of a design of a full humanoid robot. Another full humanoid project is the Shadow Robot Project (Greenhill, 1993).

Hannaford et al. (1995) use them in an anthropomorphic arm, having fifteen McKibben Muscles. The Anthroform Biorobotic Arm, as they call it, is controlled by simulated spinal neural networks. Their purpose, in a first instance, is "to improve the understanding of the reflexive control of human movement and posture".

Grodski and Immega (1988) used ROMAC to control a 1DOF teleoperated arm by means of the myoelectric signals taken from a human operator's biceps and triceps. The operator can thus make the robot arm move without having to move his own. Independent position and stiffness control of the robot arm is achieved by regulating ROMAC gauge pressure proportional to the operator's EMG signal output. Visual feedback to the operator is necessary.

Inoue (1987) describes the Soft Arm, developed by Bridgestone Co., which is powered by Rubbertuators. It has a shoulder, an upper arm, a lower arm and wrist, 4 to 5 DOFs, and a useful payload of maximum 3 kg. Possible applications that are cited are painting or coating, both needing gentle handling by the robot and explosionproof operation.

Yoshinada et al. (1991) use hydraulically actuated McKibben Muscles to power an underwater manipulator. This is one of the rare occasions where using a hydraulic actuation makes sense. The surrounding fluid is the same as the driving fluid, eliminating the weight problem. In these conditions, using gas would actually create problems due to the upward force that would act on the gas. The manipulator has a seven DOF arm and a three-fingered hand. It is designed to carry a payload of 5 kg and has a weight of 18 kg.

Baldwin (1969) proposes a series of non-robotic technical applications. One of them is a rotary engine, driven by four radially set up muscle actuators pulling an eccentric or crank. He reports engine speeds of 180rpm at 70 kPa. Besides this he reports on two biological muscle functions achieved with his type of

muscle: a sphincter action, closing off a fluid passage, and a peristaltic action. Paynter (1974) shows two possible lay-outs for rotative engines powered by PAMs. The first is actually the same as above mentioned Baldwin's. The second is an axial set-up using the swash-plate hydraulic pump configuration. Other technical applications include an active vehicle suspension system using ROMACS (Immega, 1989) and a borescope steering section actuated by hydraulically powered McKibben Muscles (Krauter, 1991).

2.5 Skeletal Muscle vs. PAM

It is beyond the scope of this work to give a detailed description of how skeletal muscle work. Nevertheless, it is important to digress somewhat on their characterization as an actuator from an engineering point of view. A comprehensive treatment of this subject can be found in McMahon (1984), of which most of the following information (all that is not marked by a citation) is drawn, and other special literature (Nigg and Herzog, 1994; Jones and Round, 1990).

2.5.1 Microscopic Aspects

Mammals have two types of muscle (Hunter and Lafontaine, 1992): smooth and striated. Striated muscles are subdivided in cardiac and skeletal muscles. Smooth muscles control the diameter of various bodily tubes such as intestines and veins, the cardiac muscle is the actuator that powers the heart and skeletal muscles drive the limbs, eye, tongue and chest. A striated muscle is a complex arrangement of parallel and series elements held together by connective tissue, and traversed by nerves, blood and lymphatic vessels. As shown in Fig. 2.13 it is a bundle of fibers, muscle cells, connected at their ends to the tendon. This modular arrangement makes skeletal muscle a very versatile actuator. Large displacement muscles have longer than average fibers, powerful muscles have more fibers than average. Furthermore, muscle fibers are nearly identical for all mammals (Hollerberg et al., 1991). The tendons are connected to the bone, by which muscle contraction force is transferred to the skeleton as a torque acting about a joint.

Each muscle fiber is a bundle of smaller fibers, called myofibrils, which are a series connection of even smaller units, called sarcomere. The connecting discs between sarcomeres are what give this type of muscle its banded or striated look. The sarcomere is the basic motor unit having a length varying, depending on the state of contraction, between $1.5\ \mu\text{m}$ and $3.6\ \mu\text{m}$. Its rest length is about $2.2\ \mu\text{m}$ which coincides with the rest position of its muscle's

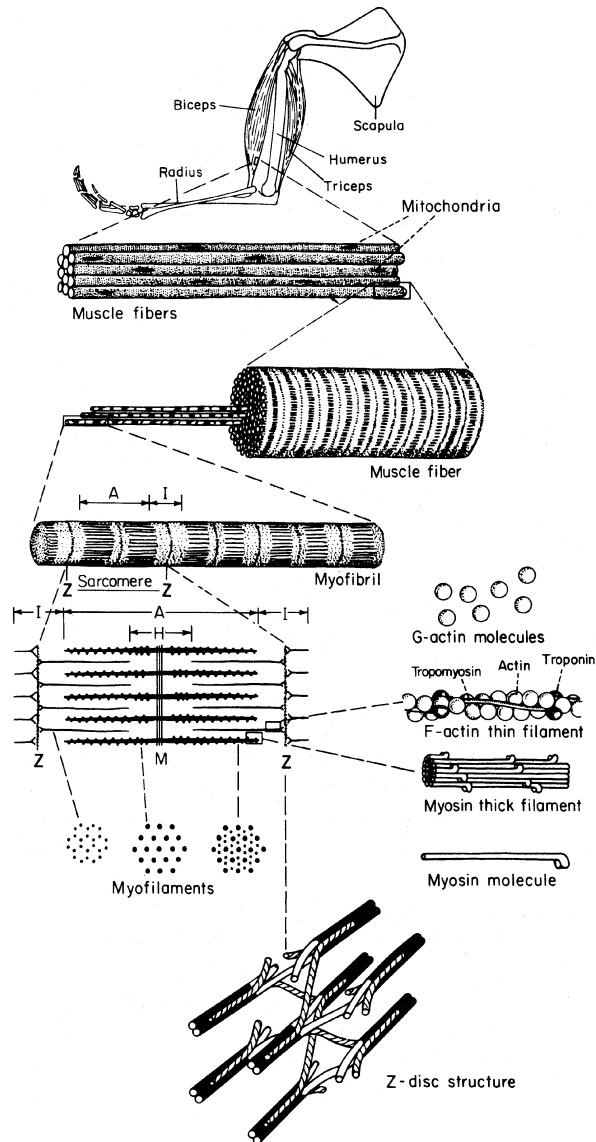


Figure 2.13: Striated muscle structure. (McMahon, 1984)

actuated limb and with maximum tension. The sarcomere is composed of an interdigitating structure of thin and thick myofilaments. Parallel bundles of these filaments are drawn into each other as the muscle contracts: this is done

by periodically attaching and detaching of the crossbridges (protrusions from the thick filaments) to the thin filaments (cf. Fig. 2.14).

Running among the myofibrils, a membrane, the sarcoplasmic reticulum, provides the sarcomeres of Calcium ions needed for contraction. It has a complex, repeated pattern organization locked to the structure of the sarcomere and contains transverse and longitudinal tubules filled with an intra-cellular fluid of a high Ca^{++} concentration. A voltage pulse, the action potential, releases Ca^{++} ions into the myofibrils where they trigger a series of biochemical reactions that cause contraction. After this pulse, the Calcium ions are pumped back into the sarcoplasmic reticulum. The exact biochemical processes bringing about contraction are, to date, still not fully understood, and subject to research and debate.

From the point of view of control, muscle fibers are organized in motor units: these are fascicles of fibers that are innervated by a single skeletomotor neuron, together with that neuron. The amount of fibers in a unit ranges from a few hundreds up to a few thousands. The smaller units are the first to be excited, this way small loads can be handled. At growing loads larger units are turned on. A direct result of this organization is the proportionality between the increment in force and the level of the force at the moment of increment.

Skeletal muscle systems are equipped with a sensory system used for motion control. These are the proprioceptors. Two types of such receptors exist: stretch receptors or spindle organs and force receptors or Golgi tendon organs. The latter are situated at the junction of muscle fibers and tendon and are in fact elastic capsules (0.8 mm long, 0.5 mm thick) whose deformation is dependent on muscular tension. The former are short fibers (2–3 mm long, 0.15 mm thick) located inside the muscle, running parallel to the muscle fibers and attached to two adjacent fibers. They can thus be regarded as a kind of strain

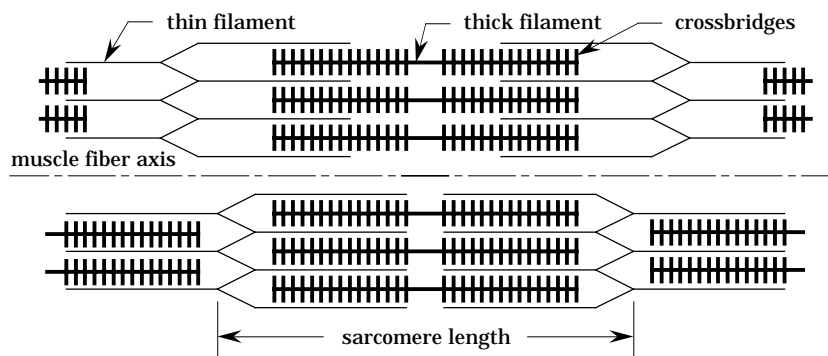


Figure 2.14: Crossbridges contraction generation.

gauge. Muscles have a density of about 5–120 spindle organs per g, depending on control demands, and about a half or a third as many Golgi tendon organs.

It is clear, even from this brief discussion about their structure, that skeletal muscle are extremely complex and ingeniously controlled transformers of chemical energy into mechanical power. Conceiving and making true artificial muscles is still far ahead. With this in mind, in the opinion of the author, Muscle Mimicking or Muscle-like Actuator would have been a better name for all actuators referred to as Artificial Muscles. Nevertheless, Artificial Muscle as an eponym is generally accepted and used.

2.5.2 Macroscopic Aspects

The microscopic complexity of muscle operation makes it a difficult task to establish a macroscopic model that describes muscle behavior. Several have been conceived, of which the Hill or active state muscle model is mostly referred to as a mechanics model. This model was derived from quick-release experiments, where a pretensioned and stretched muscle is suddenly relaxed to a lower tension and from isometric (passive and active) tension-length experiments.

In isometric tension-length characteristics, one can distinguish the developed or tetanized force and the passive force. The latter results from an elastic component. This spring element is usually non-linear: passive muscle stiffness is found to be linearly dependent on stress because more fibers get involved as stress increases. The active force shows a maximum when the muscle is at its rest length and decreases therefrom both for shortening and lengthening. It is scaled by the amount of stimulation the muscle receives. The maximum active muscle stress developed is about 200 kPa and this for all mammalian

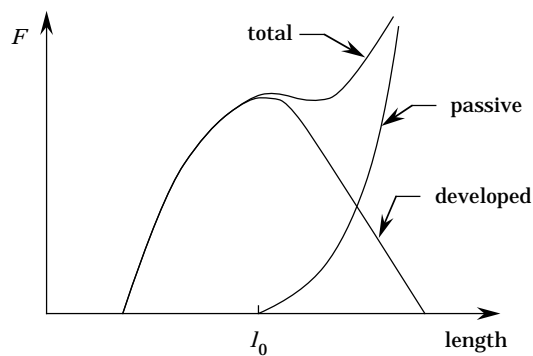


Figure 2.15: Isometric force versus muscle length.

muscle although many other parameters may be very different. The diagram in Fig. 2.15 shows the isometric behavior.

Depending on the amount of connective tissue and on stimulation level, tension versus length can have a local maximum. This curve is cited by Schulte (1961) to illustrate the likeness of skeletal muscles and McKibben actuators. These actuators, when elongated from their rest length, show a passive elastic stiffness on top of the active pressure-induced component, due to the elongation of their elastomeric inner tube.

Force-velocity relations for shortening are found to have hyperbolic shapes which can be well described by the empirical relation

$$(F + a)(v + b) = (F_0 + a)b \tag{2.14}$$

with v the shortening velocity at the start of shortening in a quick-release experiment, a and b muscle constants and F_0 the muscle's active state or isometric tetanus tension. The active state depends on the stimulation level, on muscle length and on fatigue and history of exercise. The higher the muscle's contraction rate is, the lower the load against which this happens. This decreasing of muscle tension as speed increases indicates the presence of damping working against the force developing elements. If an active muscle is loaded by a force higher than the isometric tetanus tension F_0 , it extends at a constant speed until, at some point of loading ($1.8F_0$), the muscle gives and extends

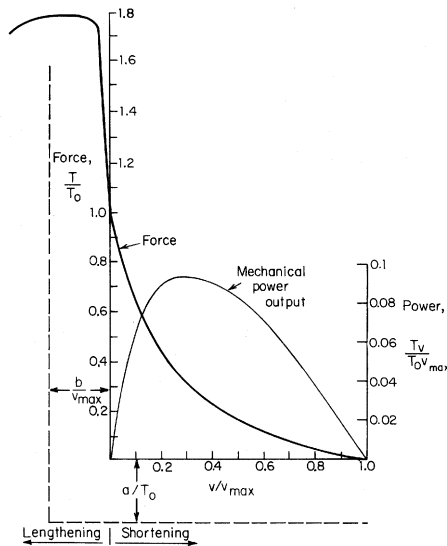


Figure 2.16: Force versus muscle velocity. (McMahon, 1984)

rapidly. Fig. 2.16 shows the force velocity relationship together with the developed power, being the product of force and velocity. The power generated by a muscle shows a maximum at force and velocity between a third and a quarter their maximum values.

The model proposed by Hill consists of a tension generating contractile element surrounded, both in series and in parallel by passive elastic elements. The contractile element is a pure force generator in parallel with a dash-pot (cf. Fig. 2.17), taking into account overall viscoelastic behavior. The force generator has as output F_0 which depends on muscle length and on time. The contractile element is characterized by its tension-length and force-velocity relationships. Passive tension-length experiments yield the sum of series and parallel elastic stiffness, while the series elastic element is determined by the instantaneous displacement in a quick-release test. An interesting consequence of this model is the possibility of isometric contraction: the contractile element can shorten while the series elastic element lengthens under the generated load, overall muscle length can thus remain unvaried.

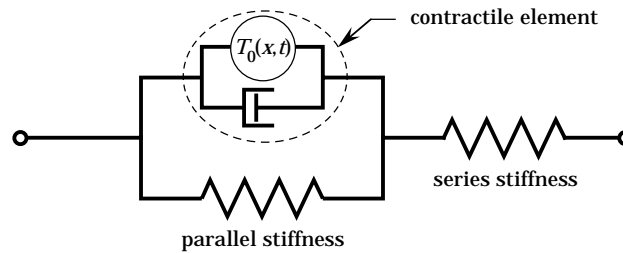


Figure 2.17: Active state muscle model. (McMahon, 1984)

This model only describes muscular behavior. Tendon elasticity has to be added to cover the full actuator, which is called the musculotendinous unit. Although the model has deficiencies, e.g. there is no unique relationship between F_0 and v at a given muscle length and level of activation (Zahalak, 1990), it is still widely used to understand muscle dynamics.

Typical performance data for skeletal muscle are (Hunter and Lafontaine, 1992; Hollerberg et al., 1991; McMahon, 1984; Chou and Hannaford, 1996):

- contraction range: within -50% to 50% of rest length, typically -12% to 36% ;
- contraction rate: 2 s^{-1} to 20 s^{-1} ;

- stress: 350 kPa peak value, 100 kPa sustained;
- power to weight ratio: 200 W/kg peak value, 50 W/kg sustained;
- efficiency: 25% to over 45%.

2.5.3 Joint Stiffness Modulation

Due to the elastic elements present in musculotendinous systems, joints driven by such actuators have an intrinsic compliance. The ability of the central nervous system to control joint compliance/stiffness independently of position is one of the key features in biological motion. This can be achieved by co-activating opposing joint muscles and, as such, it comes at an energy cost. Hogan (1984) explains this stiffness modulation in a mechanical way, comparable to the reasoning followed in §2.3.2, with neural activation replacing PAM gauge pressure: position is controlled by the ratio of activation levels, while stiffness is determined by the sum of these. Stiffness modulation is seen as a means by which gravitational destabilization of the total skeletal system can be offset: without any stiffness or with stiffness too low, the skeleton would collapse or start oscillating. On the other hand, without any compliance the system would not be able to absorb mechanical shocks or perform tasks that need delicate handling. Modulation could also be done by receptor feedback to the nervous system. Both ways have their drawbacks as stiffness regulating means: time-delay in case of feedback, which could lead to instability, energy cost in case of co-contraction. An experimental observation described by Hogan (1984) to corroborate his hypothesis is the enhanced co-activation of opposing muscles if an increasing load is imposed on the limb they drive.

Other theories to explain how position and stiffness are controlled have been put forward: Feldman (1986) describes the λ Model theory, stating how muscle static force is a function of length minus a variable threshold value, λ , controlled by the central nervous system, shifting this threshold results in moving the equilibrium position of the actuated limb; Houk (1979) suggests that neither position nor muscle force is directly controlled but that the nervous system acts to keep muscle stiffness at a more or less fixed value, using length feedback from muscle spindles and force feedback from tendon organs.

Whatever the correct or full explanation of how it is achieved, compliance or stiffness modulation is extremely important for all vertebrate systems to move about in the way they do. One can only conclude that the actuators needed to mimic the mammal kind of versatile motion, will have to show the same property.

2.6 Summary

This chapter provided an introduction to Pneumatic Artificial Muscles. Their concept, operation, properties—compliance and stiffness, antagonistic set-up, skeletal muscle resemblance, performance data and safe operation—and applications were presented. A review and classification of existing PAM-types was included.

The most commonly used type to date is the McKibben Muscle. As most other types, it suffers from friction, hysteresis and threshold behavior with regard to operating pressures. Membrane material elongation was shown to have a limiting effect on the developed force. The aim of developing the Pleated PAM was to avoid these drawbacks as much as possible.

To end this chapter a short description of skeletal muscle was given. This is not meant to be complete but serves to emphasize the extreme complexity of this biological actuator and its machine, the skeletal system.

Chapter 3

Zero Parallel Stress Pressurized Axisymmetric Membranes

3.1 Setting the Goal

In the previous chapter it was seen that elastic shell deformation has a detrimental effect on the axial force developed by the muscle actuator. Besides elastic deformation, energy dissipating effects, such as friction, and non-linear material behavior, such as rubber elongation, lead to hysteresis and threshold values of gauge pressure. Some designs produce a tension of only 53% of the ideal value due to these effects (cf. §2.2.1).

This work proposes a new design of PAM that is free of friction and elevated elastic deformation. To avoid friction it is necessary to use a closed membrane that is able to withstand the high membrane stresses without the use of an outer reinforcement: friction between the reinforcement and the membrane is intrinsic to such a layout. Avoiding high elastic deformation can be done by choosing a high tensile stiffness membrane material. Such materials, which should also be thin, flexible and gas-tight (or able to be made so), can be found for example in the class of polymer materials. The problem then is how to allow lateral expansion to happen. In order to reach a reasonable axial contraction due to inflation, a lateral expansion to at least a few times the original diameter can be expected to be necessary. This is impossibly done by elastic deformation when using a high tensile stiffness material: strains of more than a few hundredths usually lead to material failure in such a case. Furthermore, the moderate pressure levels of around 500 kPa would be insufficient to cause high strains. Therefore, other means to realize this have to be found.

This chapter will show how lateral expansion with little stress occurring in that direction can be obtained. In that case the membrane will have a surface ge-

ometry that is kept at an equilibrium mainly by the stresses in the longitudinal direction. If stress is low in the lateral direction, only marginal amounts of elastic deformation work can result from it and, consequently, muscle tension will be closer to its ideal value. The mechanism leading to expansion for the proposed design will be shown to be a rearranging of the shell.

The PAMS considered in this work are linear displacement and force devices, no torsional or bending moments are generated. Such actuators either have to be axisymmetrical or have a rotationally repeated pattern (cf. ROMAC, §2.2.2) if they are to avoid having lateral force components from the pressure loading. This chapter will consider axisymmetrical membranes in proving the point made above. The muscle design resulting from it will have a rotationally repeated pattern that is very close to an axisymmetrical geometry.

3.2 Pressurized Axisymmetric Membranes

In this section a theoretical analysis of membranes that are closed, flexible, axisymmetrical and subjected to an axial force at both ends and to a uniform orthogonal surface load, due to a pressure difference across the surface, will be presented. The purpose is to characterize such membranes in terms of geometry, membrane stresses, the pressure load and the axial force (pulling force, traction, tension). Due to axisymmetry, the surface can be described by a generating curve that is revolved around the x -axis. Any section of the membrane with a plane containing the x -axis is called a meridian curve, or in short meridian, and such plane a meridional plane. Any section with a plane perpendicular to the x -axis is called a parallel circle (circular because of the revolution) and any such plane a parallel plane. The parallel plane that runs through the center of the volume enclosed by the membrane is called the equatorial plane. When not pressurized, the membrane is assumed stretched, i.e. its generating curve will be a straight line and its shape that of a cylinder of radius R and length l . When pressurized, the generator is curved, leading to an axially shortened and laterally expanded surface.

Fig. 3.1 shows a longitudinal or meridional section of such a membrane at a pressurized state. The generator is symmetric to the equatorial plane. Each parallel is a circle of radius r , which is a function of x . At the points $(x_o, 0, 0)$ and $(-x_o, 0, 0)$ the membrane is closed by two rigid discs perpendicular to the x -axis. The contraction of this state is defined as

$$\epsilon = 1 - \frac{2x_o}{l} \quad (3.1)$$

Stresses and geometry will be a function of x , contraction, applied pressure

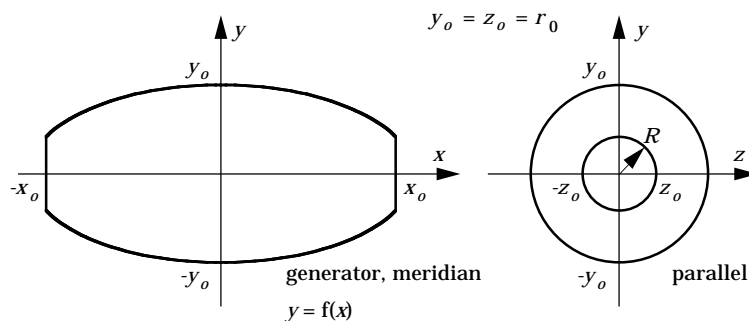


Figure 3.1: Pressurized axisymmetrical membrane.

and material properties. Traction will be a function of contraction, applied pressure and material properties.

It is known from membrane theory (Kraus, 1967; Timoshenko and Woinowsky-Krieger, 1959) that a flexible membrane cannot withstand bending moments, shear forces orthogonal to its surface and compressive stresses. As a result all stresses will be tensile and tangent to the surface. The fundamental equations are obtained by establishing the force equilibrium in the membrane. This is readily done, as shown in Fig. 3.2, across an infinitesimal surface fragment, dS , that is confined between two parallel planes, at a distance dx from each other, and two meridional planes, rotated by $d\alpha$ between each other— α being the angle with regard to the positive z -axis. Due to the axisymmetry to the long axis, each side of the fragment will be loaded by normal stresses only:

σ_1 : meridional stress, the membrane tensile stress tangent to a meridian and perpendicular to a parallel,

σ_2 : parallel stress, the membrane tensile stress tangent to a parallel circle and perpendicular to a meridian.

These are purely tensile and furthermore assumed to be constant across the thickness, s , of the membrane. The directions of these stresses coincide with the principal directions of the stress tensor and of the surface.

The sides of dS have lengths $r d\alpha$ and $(r + \tan \beta dx)d\alpha$ along the parallel sections and $dx/\cos \beta$ along the meridional sections, β being the angle between the tangent to the meridian and the x -axis with its positive direction taken counter clockwise. The forces that load dS —neglecting own weight—are due

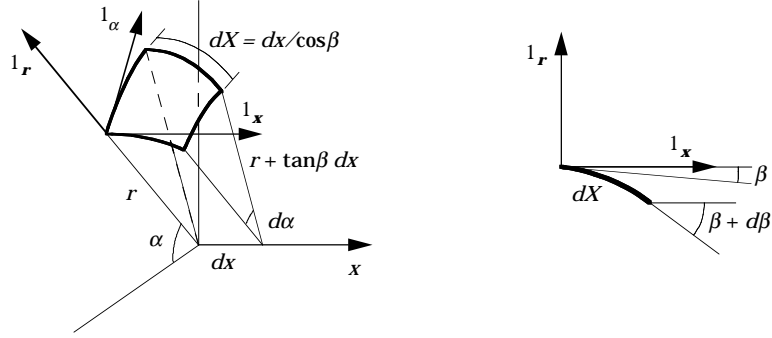


Figure 3.2: Infinitesimal surface element.

to the pressure, acting perpendicular to the surface,

$$\begin{aligned} p dS &= -p dS \sin \beta \mathbf{1}_x + p dS \cos \beta \mathbf{1}_r \\ &= -pr d\alpha dx \tan \beta \mathbf{1}_x + pr d\alpha dx \mathbf{1}_r \end{aligned} \quad (3.2)$$

and the membrane tensile forces, acting tangentially to the surface,

$$-\sigma_1 sr d\alpha = -\sigma_1 sr \cos \beta d\alpha \mathbf{1}_x - \sigma_1 sr \sin \beta d\alpha \mathbf{1}_r \quad (3.3)$$

$$\begin{aligned} \sigma_1 sr d\alpha + \frac{d(\sigma_1 sr d\alpha)}{dx} dx &= \left(\sigma_1 sr \cos \beta d\alpha + \frac{d(\sigma_1 sr \cos \beta)}{dx} d\alpha dx \right) \mathbf{1}_x \\ &\quad + \left(\sigma_1 sr \sin \beta d\alpha + \frac{d(\sigma_1 sr \sin \beta)}{dx} d\alpha dx \right) \mathbf{1}_r \end{aligned} \quad (3.4)$$

$$-\sigma_2 s dX = -\sigma_2 s \frac{dx}{\cos \beta} \mathbf{1}_\alpha \quad (3.5)$$

$$\sigma_2 s dX + \frac{d(\sigma_2 s dX)}{d\alpha} d\alpha = \sigma_2 s \frac{dx}{\cos \beta} \mathbf{1}_\alpha - \sigma_2 s \frac{dx}{\cos \beta} d\alpha \mathbf{1}_r \quad (3.6)$$

where the right-hand side of the expression of Eq. 3.4 is obtained from Eq. 3.3 and its derivative with respect to x , and the right-hand side of the expression of Eq. 3.6 from Eq. 3.5 and its derivative with respect to α . The equilibrium along $\mathbf{1}_\alpha$ yields no extra information apart from the axisymmetry. Along $\mathbf{1}_x$ one gets

$$-pr \tan \beta + \frac{d(\sigma_1 sr \cos \beta)}{dx} = 0 \quad (3.7)$$

and along $\mathbf{1}_r$

$$pr + \frac{d(\sigma_1 sr \sin \beta)}{dx} - \frac{\sigma_2 s}{\cos \beta} = 0 \quad (3.8)$$

These equations prove that an equilibrium is possible without having stress components along the parallels. In practice, this would mean that as the membrane expands radially, the material elongation in that direction would be achieved at no cost of work.

Eliminating pr from Eq. 3.8 using Eq. 3.7, leads to

$$\frac{d(\sigma_1 sr)}{dx} = \sigma_2 s \frac{dr}{dx} \quad (3.9)$$

Together with

$$\frac{dr}{dx} = \tan \beta \quad (3.10)$$

$$pr \frac{dr}{dx} = \frac{d(\sigma_1 sr \cos \beta)}{dx} \quad (3.11)$$

this leads to a set of three equations having five unknowns, namely σ_1 , σ_2 , s , r and β .

Eq. 3.11 has a straightforward first integral:

$$2\sigma_1 sr \cos \beta = pr^2 + c \quad (3.12)$$

which states that the integral of the axial tension component at point x along a parallel, $2\pi r \sigma_1 s \cos \beta$, is equal to the sum of the total force due to pressure acting on the membrane between that point and x_o , πpr^2 , and a constant πc . Taking the axial force equilibrium, this constant proves to be the traction force F_t acting at the membrane's ends:

$$2\pi \sigma_1 sr \cos \beta = \pi pr^2 + F_t \quad (3.13)$$

Eliminating β from Eqs. 3.10 and 3.13 leaves two equations (' denoting the derivative with regard to x):

$$\pi pr^2 + F_t = 2\pi \sigma_1 sr \frac{1}{\sqrt{1 + r'^2}} \quad (3.14a)$$

$$(\sigma_1 sr)' = \sigma_2 sr' \quad (3.14b)$$

with σ_1 , σ_2 , s , r and F_t unknown. The constitutive laws, describing membrane material behavior, provide the extra equations. Hooke's law for a homogeneous, orthotropic linear elastic medium are written as (Kraus, 1967)

$$\varepsilon_1 = \frac{\sigma_1}{E_1} - \frac{\nu_{12}}{E_2}\sigma_2 \quad (3.15a)$$

$$\varepsilon_2 = \frac{\sigma_2}{E_2} - \frac{\nu_{21}}{E_1}\sigma_1 \quad (3.15b)$$

$$\varepsilon_n = -\frac{\nu_{n1}}{E_1}\sigma_1 - \frac{\nu_{n2}}{E_2}\sigma_2 \quad (3.15c)$$

where the ε_i 's are the strains (n denoting the direction perpendicular to the surface), the E_i 's the Young's moduli and the ν_{ij} 's the Poisson's ratios. Due to axisymmetry, parallel strain is easily related to radius as

$$\varepsilon_2 = \frac{r - R}{R} \quad (3.16)$$

The length along a meridian can be related to the original length l of the unpressurized cylindrical membrane:

$$2 \int_{x=0}^{x=x_o} \frac{dl_e}{1 + \varepsilon_1} = 2 \int_0^{x_o} \frac{\sqrt{1 + r'^2}}{1 + \varepsilon_1} dx = l \quad (3.17)$$

This expresses how an infinitesimal piece of length dl_e originally had a length of $dl_e/(1 + \varepsilon_1)$ and integrating this has to result in the original membrane length, l . Finally, membrane thickness variation can be put down to the Poisson effect:

$$s = s_0(1 + \varepsilon_n) \quad (3.18)$$

The set of Eqs. 3.14a to 3.18, represent the eight fundamental membrane equations in eight unknowns: σ_1 , σ_2 , ε_1 , ε_2 , ε_n , s , r and F_t . Because two equations are first order differential equations, the set has to be solved for values of x ranging from 0 to x_o and boundary conditions $r(x_o) = R$ (a fixed value) and $r'(0) = 0$ (equatorial symmetry). For each value of x_o , the solution relates the membrane's geometry to its surface stresses, its strains and the axial force exerted on it to keep it at an equilibrium length ($= 2x_o$).

3.3 Zero Parallel Stress Membranes

Eqs. 3.7 and 3.8 suggest that it is possible to have force equilibrium without parallel stress components. This means $\sigma_2 = 0$ and $\varepsilon_2 \neq 0$ and therefore

Hooke's law as stated in Eq. 3.15b, is not valid anymore. As an extra property the change in membrane parallel cross-sectional area ($= A \approx 2\pi rs$ for thin membranes) will be assumed unaffected by the radial expansion. As the parallel circle diameter increases, the membrane will become thinner. Only the transverse contraction (Poisson's effect) due to the longitudinal stress will affect the cross-section. If the unpressurized membrane has a cross-sectional area A , the cross-sectional area at any pressurized state will equal $A(1 + \epsilon_n)^2$. Since it is the purpose to avoid elastic material deformation as much as possible, only high tensile stiffness materials are considered. Therefore, ϵ_1 will not be allowed to exceed a value of a few hundredths and, as the Poisson ratio typically has a value in the order of a few tenths, the transverse contraction will be disregarded. The basic set is thus reduced to:

$$\pi pr^2 + F_t = \frac{2\pi c_1}{\sqrt{1 + r'^2}} \quad (3.19a)$$

$$\sigma_1 sr = c_1 (> 0) \quad (3.19b)$$

$$2 \int_0^{x_o} \frac{\sqrt{1 + r'^2}}{1 + \frac{\sigma_1}{E_1}} dx = l \quad (3.19c)$$

$$2\pi rs = A \quad (3.19d)$$

with boundary conditions $r(x_o) = R$ and $r'(0) = 0$.

3.3.1 Analytical Solution

Eq. 3.19a can be rearranged to a differential equation of first order and first degree:

$$r' = -\frac{\sqrt{1 - \left(\frac{p}{2c_1}r^2 + \frac{F_t}{2\pi c_1}\right)^2}}{\frac{p}{2c_1}r^2 + \frac{F_t}{2\pi c_1}} = -\frac{\sqrt{1 - (c_2r^2 + c_3)^2}}{c_2r^2 + c_3}, \quad (3.20)$$

c_2 and c_3 being positive constants. It can be seen from Eqs. 3.10 and 3.12 that

$$\cos \beta = \frac{1}{\sqrt{1 + r'^2}} = c_2r^2 + c_3 \quad (3.21)$$

and, therefore $0 \leq (c_2r^2, c_3) \leq 1$. The constants c_2 and c_3 can be readily interpreted: c_2 is proportional to the ratio of pressure load to total membrane

meridional stress and c_3 is the ratio of tension to total meridional stress. The latter can also be seen as the cosine of the angle at which the meridian cuts the long axis: $c_3 = \cos \beta_{r=0}$. If this angle's value reaches $-\pi/2$, then $c_3 = 0$ and also $F_t = 0$. This implies that at that point the membrane is at its maximum contraction state. It is clear from Eqs. 3.20 and 3.10 and from the boundary condition $r'(0) = 0$ that $r' \leq 0$, $\beta \leq 0$ and $\beta_0 \equiv \beta_{x=0} = 0$.

To solve the differential equation it can be written as

$$dx = -\frac{c_2 r^2 + c_3}{\sqrt{1 - (c_2 r^2 + c_3)^2}} dr \quad (3.22)$$

which has to be integrated from $x = 0$ ($r = r_0$) to $x(r)$:

$$x = \int_r^{r_0} \frac{c_2 u^2 + c_3}{\sqrt{1 - (c_2 u^2 + c_3)^2}} du \quad (3.23)$$

This is an elliptical integral and can be split into canonical parts (cf. Appendix A) of the first, $F(x|m)$, and second, $E(x|m)$, kind.

$$\begin{aligned} I_0(r) &= \int_r^{r_0} \frac{du}{\sqrt{1 - (c_2 u^2 + c_3)^2}} \\ &= \int_0^{-\beta} \frac{d\gamma}{2\sqrt{c_2(\cos \gamma - c_3)}} \quad (c_2 u^2 + c_3 = \cos \gamma, \quad c_2 r_0^2 + c_3 = 1) \\ &= \frac{1}{\sqrt{c_2(1 - c_3)}} \int_0^{-\beta/2} \frac{d\zeta}{\sqrt{1 - \frac{2}{1 - c_3} \sin^2 \zeta}} \quad (\zeta = \gamma/2) \\ &= \frac{1}{\sqrt{2c_2}} \int_0^\varphi \frac{d\theta}{\sqrt{1 - \frac{1 - c_3}{2} \sin^2 \theta}} \quad (\sin \theta = \sqrt{\frac{2}{1 - c_3}} \sin \zeta) \\ &= \frac{1}{\sqrt{2c_2}} F\left(-\sqrt{\frac{2}{1 - c_3}} \sin \frac{\beta}{2} \left| \frac{1 - c_3}{2} \right.\right) \quad (\sin \varphi = -\sqrt{\frac{2}{1 - c_3}} \sin \frac{\beta}{2}) \end{aligned} \quad (3.24)$$

and

$$\begin{aligned}
I_2(r) &= \int_r^{r_0} \frac{u^2 du}{\sqrt{1 - (c_2 u^2 + c_3)^2}} \\
&= \int_0^{-\beta} \frac{1}{2c_2 \sqrt{c_2}} \sqrt{\cos \gamma - c_3} d\gamma \\
&= \frac{1}{c_2} \sqrt{\frac{1-c_3}{c_2}} \int_0^{-\beta/2} \sqrt{1 - \frac{2}{1-c_3} \sin^2 \zeta} d\zeta \\
&= \frac{1}{c_2} \sqrt{\frac{1-c_3}{c_2}} \left(\sqrt{\frac{2}{1-c_3}} \int_0^{\varphi} \sqrt{1 - \frac{1-c_3}{2} \sin^2 \theta} d\theta \right. \\
&\quad \left. - \frac{1+c_3}{1-c_3} \sqrt{\frac{1-c_3}{2}} \int_0^{\varphi} \frac{d\theta}{\sqrt{1 - \frac{1-c_3}{2} \sin^2 \theta}} \right) \\
&= \frac{1}{c_2} \sqrt{\frac{2}{c_2}} \left(E \left(-\sqrt{\frac{2}{1-c_3}} \sin \frac{\beta}{2} \middle| \frac{1-c_3}{2} \right) \right. \\
&\quad \left. - \frac{1+c_3}{2} F \left(-\sqrt{\frac{2}{1-c_3}} \sin \frac{\beta}{2} \middle| \frac{1-c_3}{2} \right) \right)
\end{aligned} \tag{3.25}$$

These parts combine to

$$\begin{aligned}
x &= \int_r^{r_0} \frac{c_2 u^2 + c_3}{\sqrt{1 - (c_2 u^2 + c_3)^2}} du \\
&= c_2 I_2(r) + c_3 I_0(r) \\
&= \sqrt{\frac{2}{c_2}} \left(E \left(-\sqrt{\frac{2}{1-c_3}} \sin \frac{\beta}{2} \middle| \frac{1-c_3}{2} \right) - \frac{1}{2} F \left(-\sqrt{\frac{2}{1-c_3}} \sin \frac{\beta}{2} \middle| \frac{1-c_3}{2} \right) \right)
\end{aligned} \tag{3.26}$$

Using the substitutions of Eq. 3.24, one can relate r and φ :

$$r = \sqrt{\frac{1-c_3}{c_2}} \cos \varphi \quad (3.27)$$

Instead of using the constants c_2 and c_3 , it is easier to consider φ_R and m , which are defined from

$$\begin{aligned} m &= \frac{1-c_3}{2} & c_2 &= 2m \frac{\cos^2 \varphi_R}{R^2} & 0 \leq (c_2 r^2, c_3) \leq 1 \\ R &= \sqrt{\frac{1-c_3}{c_2}} \cos \varphi_R & c_3 &= 1-2m & 0 \leq m \leq 1/2 \\ & & & & 0 \leq \varphi_R \leq \pi/2 \end{aligned} \quad (3.28)$$

The solution can then be put in a parametrical form:

$$x = \frac{R}{\sqrt{m} \cos \varphi_R} \left(E(\varphi \setminus m) - \frac{1}{2} F(\varphi \setminus m) \right) \quad (3.29a)$$

$$r = \frac{R}{\cos \varphi_R} \cos \varphi = r_0 \cos \varphi \quad (3.29b)$$

The parameter φ varies from 0 to a still unknown value φ_R , which will always be inferior to $\pi/2$. Each contraction has a distinct value φ_R . Fig. 3.3 shows the solution for one particular x_o , it shows the parameter as well as some of the constants.

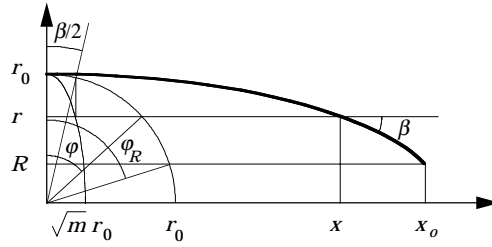


Figure 3.3: Solution of set Eqs. 3.29.

As for σ_1 , one can see from combining Eqs. 3.19b and 3.19d that

$$\sigma_1 = \frac{2\pi c_1}{A} \quad (3.30)$$

so it has a constant value whatever x (this value depending of course on the contraction, the pressure and the material constants). The length constraint

Eq. 3.19c can then be expressed as

$$2 \int_0^{x_o} \sqrt{1+r'^2} dx = 2I_0(R) = l \left(1 + \frac{2\pi c_1}{AE_1} \right) = l \left(1 + \frac{\pi p}{AE_1 c_2} \right) \quad (3.31)$$

which, using Eq. 3.24, is the same as

$$\sqrt{\frac{2}{c_2}} F(\varphi_R \setminus m) = l \left(1 + \frac{\pi p}{AE_1 c_2} \right) \quad (3.32)$$

or

$$\frac{F(\varphi_R \setminus m)}{\sqrt{m} \cos \varphi_R} = \frac{l}{R} \left(1 + \frac{\pi p R^2}{2AE_1 m \cos^2 \varphi_R} \right) \quad (3.33)$$

From this last equation and from

$$x_o = \frac{R}{\sqrt{m} \cos \varphi_R} \left(E(\varphi_R \setminus m) - \frac{1}{2} F(\varphi_R \setminus m) \right) \quad (3.34)$$

the constants m and φ_R are to be determined.

At any contraction ϵ the geometry of the membrane under the conditions of zero parallel stress is now fully set by

$$x = \frac{R}{\sqrt{m} \cos \varphi_R} \left(E(\varphi \setminus m) - \frac{1}{2} F(\varphi \setminus m) \right) \quad 0 \leq \varphi \leq \varphi_R \quad (3.35a)$$

$$r = \frac{R}{\cos \varphi_R} \cos \varphi \quad 0 \leq \varphi \leq \varphi_R \quad (3.35b)$$

$$\frac{E(\varphi_R \setminus m) - \frac{1}{2} F(\varphi_R \setminus m)}{\sqrt{m} \cos \varphi_R} = \frac{l}{2R} (1 - \epsilon) \quad (3.35c)$$

$$\frac{F(\varphi_R \setminus m)}{\sqrt{m} \cos \varphi_R} = \frac{l}{R} \left(1 + \frac{a}{2m \cos^2 \varphi_R} \right) \quad (3.35d)$$

notating $a = \pi p R^2 / AE_1$. The parametric representation $x(\varphi)$ - $r(\varphi)$ and the constants m and φ_R are determined as a function of three dimensionless parameters: contraction ϵ , muscle slenderness l/R and a , which is the membrane's longitudinal strain when only loaded by the pressure at the end closures and, thus, can be taken as a measure for the membrane's compliance in that direction.

3.3.2 Numerical Solution

To solve this set of Eqs. 3.35 numerically, the constants φ_R and m have to be found from the last two equations. Because of the complex way in which the constants depend on ϵ , l/R and a , a reverse way of solving has been followed. Eq. 3.35d is rewritten to

$$F(\varphi_R \setminus m) = \frac{l}{R} \left(\sqrt{m} \cos \varphi_R + \frac{a}{2\sqrt{m} \cos \varphi_R} \right) \quad (3.36)$$

From the definitions of m (Eq. 3.28) and c_3 (Eq. 3.20) it can be seen that m has values ranging between 0 and 0.5. At full inflation, $F_t = 0$ and hence $c_3 = 0$ and $m = 0.5$. At zero contraction an inelastic membrane ($E_1 = \infty$) has $r' = 0$ since lateral expansion can only happen if the meridional length changes. Consequently, $r = R$ and, from Eq. 3.20, it can be seen that $c_2 R^2 + c_3 = 1$. This relation can be satisfied by an infinite and by a finite value for F_t . If $F_t = 2\pi c_1 = \infty$, $c_3 = 1$ and $m = 0$. If F_t has a finite value, the condition $\sigma_2 = 0$ is not met any more: in that case the membrane is in fact a closed pressurized cylinder having a hoop stress $\sigma_2 = pr/s$. At finite values of E_1 , m 's minimum value is somewhat higher than 0.

Starting from 0.5, a series of values of m is entered in Eq. 3.35d which is then each time solved for φ_R . This is done using MATLAB® and Newton's rootfinding method. The pair of constants is then entered in Eq. 3.35c to calculate the corresponding contraction.

Fig. 3.4 shows the right-hand side of Eq. 3.36 for $l/R = 10$, $a = 0.001$, φ_R ranging from 0° to 90° and different values of m . The points at which this curve is intersected by that of the elliptic integral of the first kind (cf. Fig. A.1) determine the values of the constants. Comparing the figures it is clear that they

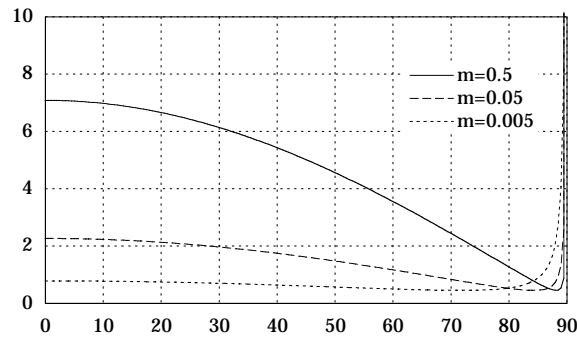
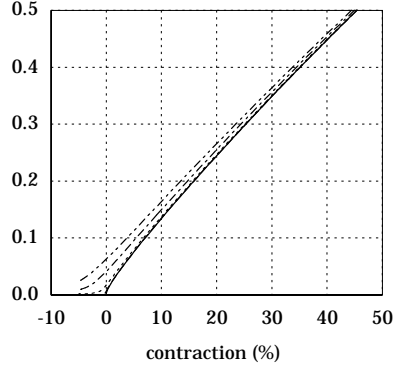
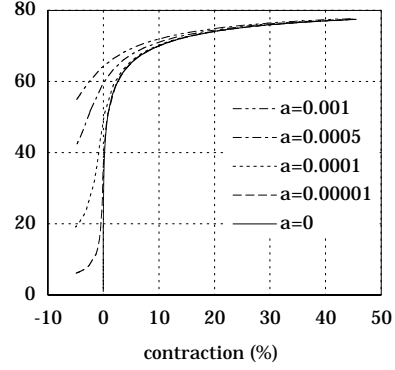


Figure 3.4: $\frac{l}{R} \left(\sqrt{m} \cos \varphi_R + \frac{a}{2\sqrt{m} \cos \varphi_R} \right)$ as a function of φ_R ($^\circ$).

Figure 3.5: m (°).Figure 3.6: φ_R (°).

have two, one or no intersections, as the value of m gradually diminishes from 0.5. If there are two solutions for φ_R , the second has a value very close to $\pi/2$. Putting this value into Eq. 3.35c yields an extremely high and negative value for ϵ , implying that the membrane is strongly elongated. The assumption of linear elastic behavior is not valid for strains higher than a few percentage points and therefore this second solution for φ_R is regarded as having no practical meaning.

If the change in contraction from one value of m to the next is too big or if Eq. 3.35d does not yield a solution any more, the step for m is refined. This process is repeated until the value of membrane contraction reaches -5% , meaning an elongation of 5% .

The solutions for the constants m and φ_R for a slenderness of 10 to 1 and values of a of 10^{-3} , 5×10^{-4} , 10^{-4} , 10^{-5} and 0 are shown in Figs. 3.5 and 3.6. The higher the membrane tensile compliance, the higher the values of m and φ_R . Besides this, the maximum attainable contraction is slightly diminished at increasing values of compliance. From the discussion of Eq. 3.21 it is known that the maximum contraction is characterized by a right angle intersecting of the meridian and the long axis. If the membrane yields, the meridional length increases and the intersection angle steepens. Consequently, the right angle is attained at a lower contraction.

Fig. 3.7 shows the meridians for the membrane at $a = 10^{-4}$ (or in detail: $l = 10$ cm, $R = 1$ cm, $s_0 = 0.5$ mm, $E_1 = 10$ MPa, $p = 100$ kPa) and various contractions. Due to meridional elasticity, the membrane bulges at all contractions and even at elongation. This would not be so if it were inelastic as was indicated above. In that case, the force developed by the internal pressure loading would tend to an infinitely high value at zero contraction.

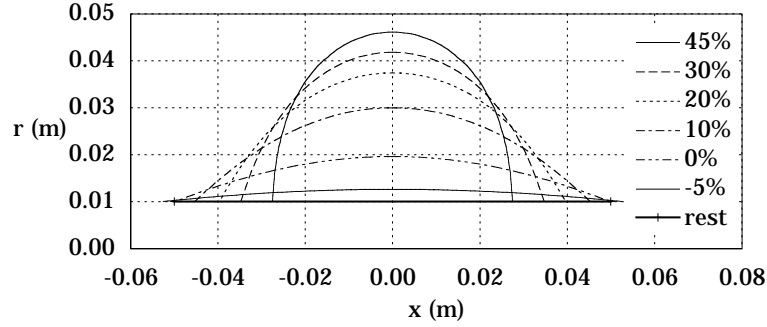


Figure 3.7: Meridians of a zero parallel stress membrane at various contractions.

3.3.3 Characteristics

In this section, the analytical expressions of a number of membrane characteristics are derived: the end closure angle, the equatorial diameter, the enclosed volume, the axial force, the meridional stress and, finally, the meridional strain. Each characteristic's numerical values have been calculated for the same conditions as above, they are represented as a function of contraction/elongation and for various values of membrane compliance.

End Closure Angle

The angle of the meridian with respect to the long axis at the end discs is found from Eqs. 3.21 and 3.28:

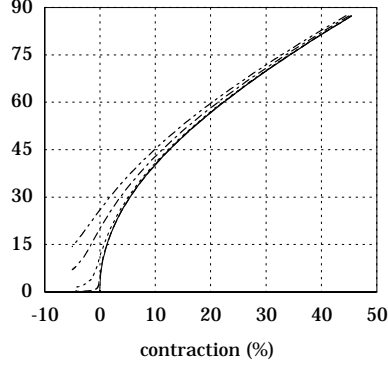
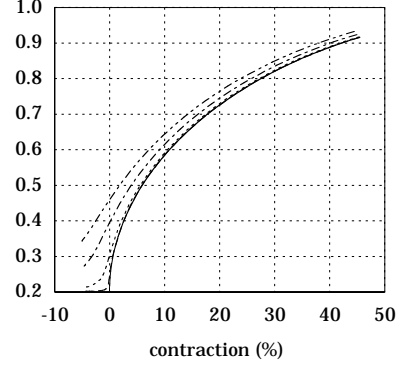
$$\cos \beta_R = 1 - 2m \sin^2 \varphi_R \quad (3.37)$$

defining β_R as a function of ϵ , l/R and a . Increasing the pressure or choosing a lower tensile stiffness membrane results in a higher membrane compliance and, as can be seen from Fig. 3.8 (legend cf. Fig. 3.6), higher values of the end closure angle. Due to compliance, the material yields and the membrane bulges more at the same contraction.

Equatorial Diameter

The equatorial diameter, which is the diameter at the muscle's center, where φ equals zero, follows directly from Eq. 3.29b:

$$D = 2r_0 = \frac{2R}{\cos \varphi_R} = ld\left(\epsilon, \frac{l}{R}, a\right) \quad (3.38)$$

Figure 3.8: $-\beta_R$ ($^\circ$).Figure 3.9: d ().

It is directly proportional to a dimensionless function d assembling the influence of contraction, slenderness and compliance. That way membranes of different sizes can be readily compared. Other characteristics will show this property as well, each will be directly proportional to a dimensionless function and a factor depending on the size and the characteristic's dimensions. Fig. 3.9 (legend cf. Fig. 3.6) shows d as a function of contraction and compliance.

Enclosed Volume

The enclosed volume can be calculated in the classical manner:

$$\begin{aligned} V &= 2 \int_0^{x_o} \pi r^2 dx = 2\pi \int_R^{r_0} \frac{r^2(c_2 r^2 + c_3)}{\sqrt{1 - (c_2 r^2 + c_3)^2}} dr \\ &= 2\pi c_2 I_4(R) + 2\pi c_3 I_2(R) \end{aligned} \quad (3.39)$$

I_4 has to be reduced using the rules from Appendix A, with $a_0 = -c_2^2$, $a_1 = 0$, $a_2 = -c_2 c_3/3$, $a_3 = 0$ and $a_4 = 1 - c_3^2$:

$$\begin{aligned} r^n Y &= -(n+2)c_2^2 I_{n+3} - 2(n+1)c_2 c_3 I_{n+1} + n(1 - c_3^2) I_{n-1} \\ rY &= -3c_2^2 I_4 - 4c_2 c_3 I_2 + (1 - c_3^2) I_0 \end{aligned} \quad (3.40)$$

leading to

$$\left[r \sqrt{1 - (c_2 r^2 + c_3)^2} \right]_R^{r_0} = -3c_2^2 I_4(R) - 4c_2 c_3 I_2(R) + (1 - c_3^2) I_0(R) \quad (3.41)$$

or

$$2\pi c_2 I_4(R) = \frac{2\pi R}{3c_2} \sqrt{1 - (c_2 R^2 + c_3)^2} - \frac{8\pi c_3}{3} I_2(R) + 2\pi \frac{1 - c_3^2}{3c_2} I_0(R) \quad (3.42)$$

And, with Eqs. 3.24 and 3.25

$$\begin{aligned} V &= \frac{2\pi}{3c_2} \sqrt{\frac{2}{c_2}} \left(\frac{1 + c_3}{2} F \left(\varphi_R \setminus \frac{1 - c_3}{2} \right) - c_3 E \left(\varphi_R \setminus \frac{1 - c_3}{2} \right) \right) \\ &\quad + \frac{2\pi}{3c_2} R \sqrt{1 - (c_2 R^2 + c_3)^2} \\ &= \frac{2\pi}{3c_2} \left(\frac{1}{2} \sqrt{\frac{2}{c_2}} F \left(\varphi_R \setminus \frac{1 - c_3}{2} \right) - c_3 x_o \right) + \frac{2\pi}{3c_2} R \sqrt{1 - (c_2 R^2 + c_3)^2} \\ &= \frac{2\pi}{3c_2} \left(\frac{l}{2} \left(1 + \frac{\pi p R^2}{2AE_1 m \cos^2 \varphi_R} \right) - c_3 x_o \right) + \frac{2\pi}{3c_2} R \sqrt{1 - (c_2 R^2 + c_3)^2} \\ &= \frac{\pi R^2}{3m \cos^2 \varphi_R} \left(\frac{l}{2} \left(1 + \frac{a}{2m \cos^2 \varphi_R} \right) - (1 - 2m)x_o \right. \\ &\quad \left. + R \sqrt{1 - (1 - 2m \sin^2 \varphi_R)^2} \right) \end{aligned}$$

which results to

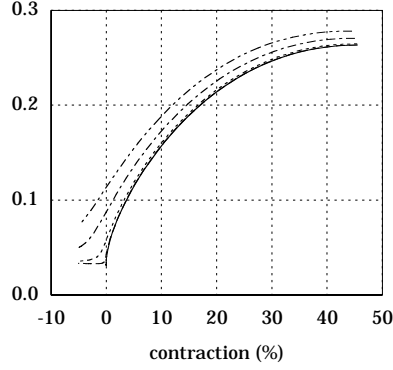
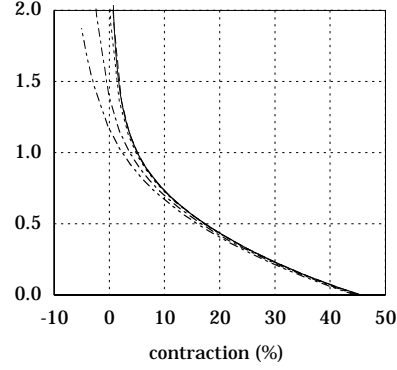
$$\begin{aligned} V &= \frac{\pi R^2 l}{6m \cos^2 \varphi_R} \left(1 + \frac{a}{2m \cos^2 \varphi_R} - (1 - 2m)(1 - \epsilon) \right. \\ &\quad \left. + \frac{2R}{l} \sqrt{1 - (1 - 2m \sin^2 \varphi_R)^2} \right) \\ &= l^3 v \left(\epsilon, \frac{l}{R}, a \right) \end{aligned} \quad (3.43)$$

From Fig. 3.10 (legend cf. Fig. 3.6), showing v as a function of contraction, it is clear how the volume reaches a maximum as contraction increases.

Tension

Tension or traction is expressed as (cf. Eq. 3.20)

$$F_t = 2\pi c_1 c_3 = \pi p \frac{c_3}{c_2} = \pi p R^2 \frac{1 - 2m}{2m \cos^2 \varphi_R} = p l^2 f_t \left(\epsilon, \frac{l}{R}, a \right) \quad (3.44)$$

Figure 3.10: $v(\cdot)$.Figure 3.11: $f_t(\cdot)$.

The influence of contraction, slenderness and compliance are again gathered in one dimensionless function f_t . Referring to §2.1, the effective area of the membrane can be written as $l^2 f_t$. Due to elastic membrane deformation, it has a lower value with respect to the inelastic case, as is clear from Fig. 3.11 (legend cf. Fig. 3.6). The reason for this is the increased bulging at higher compliance. If $E_1 = \infty$, m and φ_R will be zero at zero contraction and, hence, F_t will be infinitely high.

Stress and Strain

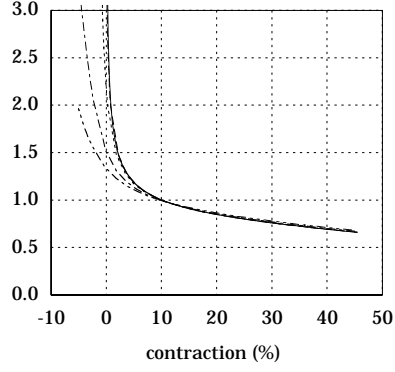
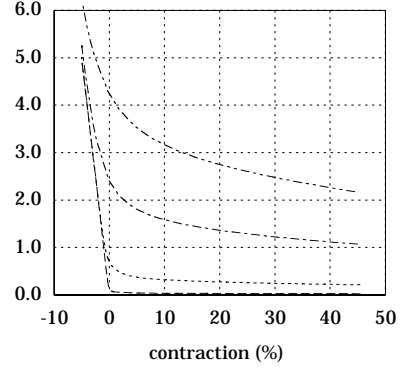
The meridional stress and strain, from Eq. 3.30 and from the definition of c_2 in Eq. 3.20, are

$$\sigma_1 \approx \frac{2\pi c_1}{A} = \frac{\pi p}{c_2 A} = \frac{\pi p R^2}{2Am \cos^2 \varphi_R} = \frac{pl^2}{A} \varsigma\left(\epsilon, \frac{l}{R}, a\right) \quad (3.45)$$

and

$$\epsilon_1 \approx \frac{2\pi c_1}{AE_1} = \frac{a}{2m \cos^2 \varphi_R} \quad (3.46)$$

They are shown in Figs. 3.12 and 3.13 (legends cf. Fig. 3.6). The meridional stress will never be zero, whatever the state of contraction or tension. Once contraction exceeds 10%, stress does not change much any more, as can be seen in Fig. 3.12. Meanwhile, however, tension gradually diminishes to zero.

Figure 3.12: ζ ().Figure 3.13: ε_1 (%).

3.4 Inelastic Approximation

Figs. 3.5 to 3.12 show that the influence of elasticity is not very significant at contractions of more than 5%. At longer lengths the meridional stress grows extremely large, the material yields to these high stress levels and tension drops to more realistic values. At contractions of more than 5% the inelastic behavior can be used as an approximation to compare membranes of different values of slenderness.

If E_1 tends to infinity, a will become zero and the relations of Eqs. 3.35c and 3.35d simplify to

$$\frac{E(\varphi_R \setminus m)}{\sqrt{m} \cos \varphi_R} = \frac{l}{R} \left(1 - \frac{\epsilon}{2}\right) \quad (3.47a)$$

$$\frac{F(\varphi_R \setminus m)}{\sqrt{m} \cos \varphi_R} = \frac{l}{R} \quad (3.47b)$$

In this case, the constants m and φ_R are independent of pressure and elasticity. Therefore, all dimensionless functions established in the previous section will only depend on slenderness and contraction:

$$D = \frac{2R}{\cos \varphi_R} = l d_0\left(\epsilon, \frac{l}{R}\right) \quad (3.48)$$

$$\begin{aligned} V &= \frac{\pi R^2 l}{6m \cos^2 \varphi_R} \left(1 - (1 - 2m)(1 - \epsilon) + \frac{2R}{l} \sqrt{1 - (1 - 2m \sin^2 \varphi_R)^2}\right) \\ &= l^3 v_0\left(\epsilon, \frac{l}{R}\right) \end{aligned} \quad (3.49)$$

$$F_t = \pi p R^2 \frac{1 - 2m}{2m \cos^2 \varphi_R} = p l^2 f_{t0}(\epsilon, \frac{l}{R}) \quad (3.50)$$

$$\sigma_1 \approx \frac{2\pi c_1}{A} = \frac{\pi p R^2}{2Am \cos^2 \varphi_R} = \frac{p l^2}{A} s_0(\epsilon, \frac{l}{R}) \quad (3.51)$$

These expressions show how membranes of different sizes but identical slenderness have their characteristics depending on size: equatorial diameter on length, force on the square of length and volume on the cube of length. Meridional stress is independent of size if the membrane thickness, s , is proportional to size. If one intends to double the force at the same pressure while using geometrically similar membranes, length has to increase by only 41%, but volume—and thus pressurized gas consumption—will increase by 183%. However this also implies contraction lengths being 41% larger, which is not always needed. On the other hand, if one doesn't need high forces it is possible to replace one long membrane by a series of n similar but shorter ones so that total length and contraction are preserved but total volume and, likewise, force are divided by n^2 .

Eqs. 3.47a to 3.51 have been solved for membranes of varying slenderness. The diagrams in figures 3.14 to 3.22 plot the results as a function of contraction and for different values of the inverse of slenderness, broadness, R/l (ranging from 0.5 down to zero for an infinitely thin membrane).

The maximum attainable contraction or travel is strongly dependent on slenderness: slim membranes have a greater travel than broader ones. As R increases with regard to l , the pressure load acting on the end closures increases and therefore, the axial force equilibrium at the ends (cf. Eq. 3.13), with $F_t = 0$,

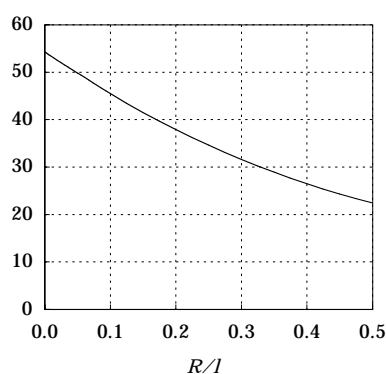
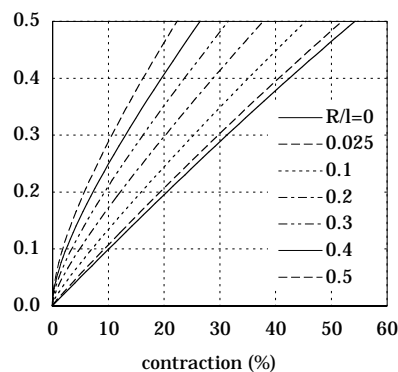
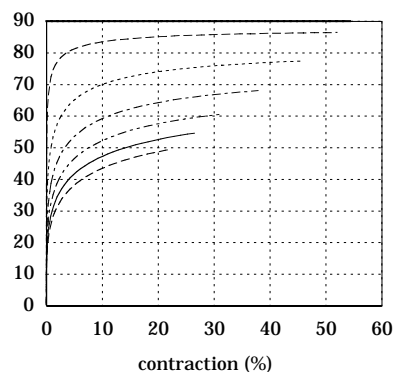


Figure 3.14: Travel (%) as a function of broadness.

Figure 3.15: m ().Figure 3.16: φ_R (°).

will be reached at lower values of $-\beta_R$. Hence, the meridian curve is flatter for lower values of slenderness, it bulges less and this results in a lower maximum contraction. Fig. 3.14 shows travel as a function of broadness. An infinitely thin membrane has the greatest ability to contract: its travel is about 54.3%. This, however, is a limiting case that will not be feasible in practice. At a more practicable slenderness of $l/R = 10$ maximum contraction is about 45.5%; a membrane having an initial diameter equal to its length, has a travel of only 22.3%.

In Fig. 3.15 m is diagrammed as a function of contraction and broadness. As was discussed in §3.3.2, m 's values range from 0 at full length to 0.5 at full contraction. In Fig. 3.16 one can see how φ_R increases from zero at full length to a value less than $\pi/2$ at full contraction. The latter is smaller as the membrane's broadness is higher: this is due to fact that broader membranes bulge less. At extremely small contractions the value of φ_R is near to zero and values of the elliptic integrals are approximated by

$$F(\varphi_R \setminus m) \approx \left(1 + \frac{m\varphi_R^2}{4}\right)\varphi_R \approx \varphi_R \quad (3.52)$$

$$E(\varphi_R \setminus m) \approx \left(1 - \frac{m\varphi_R^2}{4}\right)\varphi_R \approx \varphi_R \quad (3.53)$$

Putting these approximations in Eqs. 3.47a and 3.47b results to the relation $\varphi_R \approx (l/R)\sqrt{m}$ —explaining the steeper increase of φ_R at low contractions—and to the consideration that ϵ is of a higher order exponent with regard to φ_R .

Fig. 3.16 also shows how, as slenderness increases, φ_R gradually evolves towards a constant value of $\pi/2$ regardless of contraction. In the limiting case of zero

broadness, the incomplete elliptic integrals of Eqs. 3.47a and 3.47b will become complete integrals. In these equations $\sqrt{m} \cos \varphi_R / R$ is indeterminate in that case and has to be replaced by $\sqrt{c_2/2}$:

$$\sqrt{\frac{2}{c_2}} E\left(\frac{\pi}{2} \setminus m\right) = l\left(1 - \frac{\epsilon}{2}\right) \quad (3.54a)$$

$$\sqrt{\frac{2}{c_2}} F\left(\frac{\pi}{2} \setminus m\right) = l \quad (3.54b)$$

These now determine m and c_2 as a function of contraction and initial length l . At low values of their parameter m , the integrals can be approximated by (Abramowitz and Stegun, 1965)

$$F\left(\frac{\pi}{2} \setminus m\right) \approx \frac{\pi}{2} \left(1 + \frac{m}{4}\right) \quad (3.55)$$

$$E\left(\frac{\pi}{2} \setminus m\right) \approx \frac{\pi}{2} \left(1 - \frac{m}{4}\right) \quad (3.56)$$

and, in that case $\epsilon \approx m$, as can be checked with Fig. 3.15.

The end closure angle, shown in Fig. 3.17 (legend cf. Fig. 3.15), will always be straight at full length since no expansion occurs at this state. Only for the zero broadness membrane will this angle evolve towards a right angle, all other membranes will have an end closure angle of less than $\pi/2$ at full contraction. The reason for this is the gaining in importance of the pressure load acting on the end closures, as was explained earlier.

The equatorial diameter function d_0 is plotted in Fig. 3.18 (legend cf. Fig. 3.15). For higher values of broadness the membrane's overall values of diameter, obviously, increase, but the total increase in diameter with contraction is less for

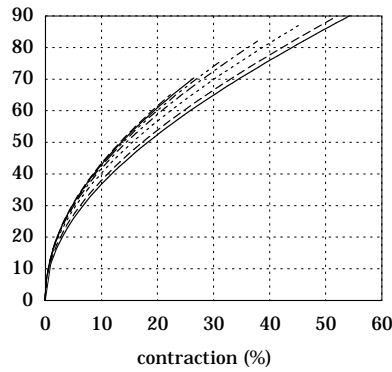


Figure 3.17: $-\beta_R$ ($^\circ$).

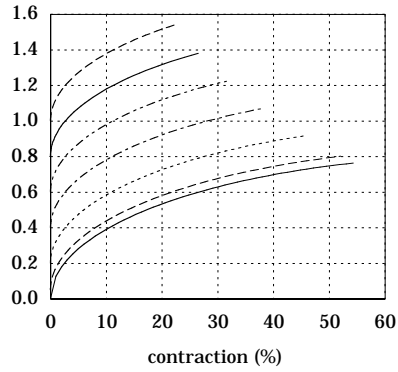


Figure 3.18: d_0 ().

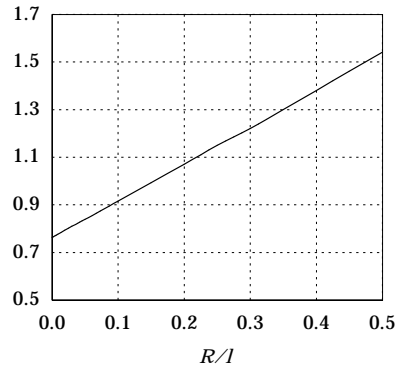


Figure 3.19: d_{0max} ().

broader membranes. The reason for this is the lesser bulging of broad membranes compared to thin. The equatorial diameter's maximum value, occurring at full inflation, which could be defined as the membrane's bulk diameter, lies around the value of the rest length l : its absolute minimum is about $0.76l$ and for a membrane of slenderness 2 it is about $1.54l$. Fig. 3.19 pictures the bulk diameter to full length ratio as a function of broadness, it shows a nearly linear relationship between both.

The influence of broadness on volume is can be seen from Fig. 3.20 (legend cf. Fig. 3.15): although they bulge less, broader membranes have a higher increase in volume with contraction. This indicates higher tensions for the bulkier membranes. The ratio of bulk volume—the volume at maximum contraction—

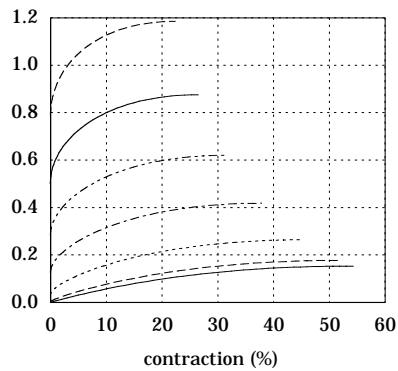


Figure 3.20: v_0 ().

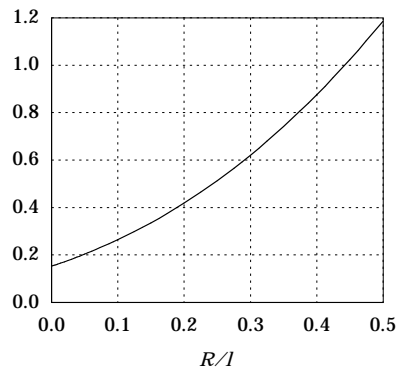


Figure 3.21: v_{0max} ().

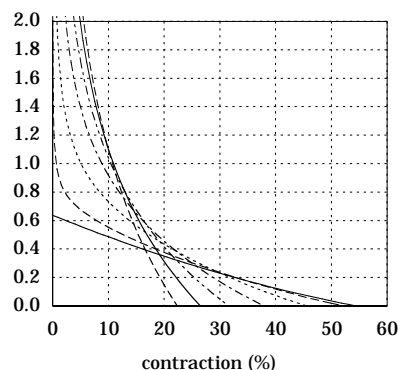


Figure 3.22: $f_{t0} ()$.

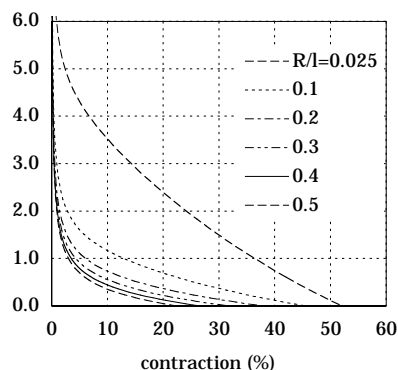


Figure 3.23: $f_{t0}/2\pi R (m^{-1})$.

to the cube of full length as a function of broadness is given in Fig. 3.21. Broadness, obviously, has an important influence on bulk volume and, therefore, on the power the membrane can transfer: broader membranes have a smaller travel compared to slender membranes of the same length, but their tension and the resulting power transfer are much higher.

The dimensionless tension function is plotted in Fig. 3.22 (legend cf. Fig. 3.15). As was mentioned above, the broader the membrane is, the stronger it pulls but also the steeper force drops to zero. In broader membranes the gas has a much greater surface against which to act but at the same time the end closure surfaces and thereby the pressure load against them increase. From Eq. 3.50 and the fact that both $m = 0$ and $\varphi_R = 0$ at zero contraction, it is clear that force will tend to infinity as could be expected from the discussion on the lower value of m in §3.3.2.

The infinitely thin membrane shows a peculiarity at zero contraction: its force at that point is finite. Its value can be found from Eqs. 3.50 and 3.54b:

$$F_t = \frac{2pl^2}{\pi} \quad (3.57)$$

This is, in fact, a physical singularity: at full length, the volume is zero so no gas is contained by the membrane and no pressure can be exerted on the membrane's surface.

It is interesting to look at the plot of tension per unit length along the end closure's circumference $f_{t0}/2\pi R$, as shown in Fig. 3.23: although tension increases for broader membranes of the same length, their tension per length decreases. This implies that slender membranes impose higher stresses on the end closures even though forces are generally lower. This will put a lower limit

on technically feasible values of slenderness.

3.5 Maximum Volume Property

From the calculus of variations Gelfand and Fomin (1963) it can be proven that of all axisymmetrical surfaces that are limited by the same two discs and have a fixed generating curve length, the surface described by the inelastic zero parallel stress membrane encloses the highest volume.

The problem is put as follows, defining

$$I = \int_{x_1}^{x_2} f(x, y(x), y'(x)) dx \quad \text{and} \quad J = \int_{x_1}^{x_2} g(x, y(x), y'(x)) dx \quad (3.58)$$

one has to determine the function $y(x)$ that maximizes I , given the constraint that J is an arbitrary positive constant, and given the boundary conditions $y(x_1) = y_1$ and $y(x_2) = y_2$. This is an isoperimetric problem that is solved by establishing the Euler equation using $h = f + \lambda g$:

$$\frac{\partial h}{\partial y} - \frac{d}{dx} \left(\frac{\partial h}{\partial y'} \right) = 0 \quad (3.59)$$

the result of which is a differential equation having $y = y(x, \lambda)$ for solution and the boundary conditions to determine λ . If one takes I to be the enclosed volume and J the length of the generator, which is independent of the meridional tension because $E_1 = \infty$, one can write

$$f(x, y(x), y'(x)) = \pi x^2 \quad \text{and} \quad g(x, y(x), y'(x)) = \sqrt{1 + (y'(x))^2} \quad (3.60)$$

and, thus, the Euler equation becomes

$$2\pi y - \frac{\lambda y''}{\left(1 + (y'(x))^2\right)^{3/2}} = 0 \quad (3.61)$$

which has for obvious first integral:

$$\pi y^2 + \frac{\lambda}{\sqrt{1 + (y'(x))^2}} = c \quad (3.62)$$

This is none other than Eq. 3.19a with $c = -F_t/\pi p$ and $\lambda = 2\pi c_1/p$, which proves the statement made.

It implies that the inelastic zero parallel stress muscle, of all comparable axisymmetrical muscles working at the same pressure, transfers the highest possible amount of work when going from zero contraction to an intermediate contraction. One has to note, though, that the prove only holds if the volume is effectively represented by I . This is not longer so once the end angle exceeds the value of $\pi/2$.

3.6 Summary

A rigorous mathematical basis and model for the Pleated PAM was presented in this chapter. It started with a general mathematical description of pressurized axisymmetrical membranes. These membranes were shown to have only two stress components, coinciding with the membranes' surface principle directions—the meridional and the parallel direction. Maintaining the membrane equilibrium was proved to be possible without parallel stress components. This is the basis of the Pleated PAM as will be seen in Chapter 4.

In this zero parallel stress case the meridional curve (surface generating curve) can be related to the applied gauge pressure and exerted tension by a linear first order differential equation. This equation was solved analytically and numerically. The characteristics, such as equatorial diameter, volume, developed tension, stress and material strain were subsequently derived and these were found to be proportional to dimensionless expressions, assembling the influence of contraction, slenderness and material compliance.

If a high tensile stiffness membrane material is used, the influence of membrane elastic yielding was shown to be insignificant at contractions exceeding 5%. An inelastic solution of the zero parallel stress case was therefore derived and discussed. This led to geometric similarity laws, relating the characteristics of scaled membranes. The influence of slenderness was examined: apart from being bulkier, broader membranes were proved to have less travel, a generally higher tension, but a lower tension per unit length along the end parallel circles.

Finally, it was seen that the inelastic zero parallel stress condition leads to a muscle that transfers the highest possible amount of work compared to other axisymmetrical muscles.

Chapter 4

Pleated Pneumatic Artificial Muscles

4.1 Concept

Making a PAM that can expand without parallel stress poses practical problems because no material can elongate in the absence of stress. This means that, strictly, it cannot be built. It can however be approximated to a satisfactory degree. To see how, one can consider a membrane that, at full length, is packed together in many folds or pleats that lie along meridional planes. Expansion of such a membrane can happen by unfurling these folds. Fig. 4.1 sketches this arrangement and process for a muscle having twelve folds.

As each such fold has a finite depth, the surface will always be composed of a series of ridges and valleys along a parallel. In fact, the surface will not be axisymmetrical: it will have a rotationally repeated pattern—provided all pleats have the same dimensions. Fig. 4.2 depicts a strip of the membrane going from a ridge to the bottom of a valley in the lateral direction and from

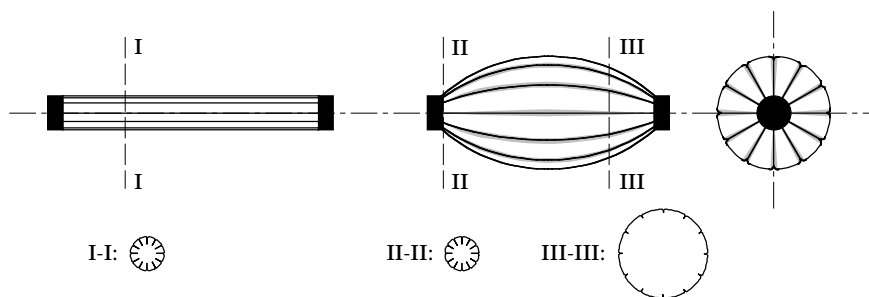


Figure 4.1: Pleated PAM.

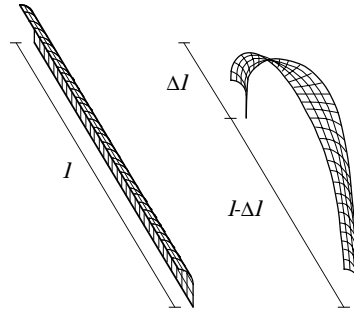


Figure 4.2: Detail strip of a pleated membrane.

end closure to end closure in the longitudinal direction. The strip is shown at full length and at full contraction—at which point the equatorial section is assumed to be circular. When in a contracted state, the meridian of a ridge and that of a valley line will not be of the same kind: the former will be more prolate with regard to the theoretical meridian, the latter more oblate. The reason for this is the difference in values of initial radius for each of these lines. A ridge obviously has a higher value of R than a valley line and, consequently, as was seen in §3.4, at that point the membrane would normally expand to a larger diameter. Unfolding, however, tends to bring the parallel section closer to a circular shape near the equator and this can only be done by increasing the diameter at a valley line and by decreasing that at the ridge. One could say that both pull each other towards a mean diameter. The deeper the fold the greater the difference in R and, thus, the stronger the deviation.

The amount of folds depends on the fold depth and on the ratio of bulk diameter to initial diameter (ratio of expansion): a higher ratio or shallower folds imply that more folds are needed to be able to expand fully. From the calculation of the diameter, as in §3.3.3, one can obtain the ratio of expansion and by choosing the fold depth it is then possible to determine the minimum amount of folds needed. Alternatively, one could use the diagram in Fig. 3.18 to obtain a slightly undervalued estimate and then proceed by putting in a few more folds.

The theoretical zero parallel stress case, as presented in the previous section, can be regarded as a limiting case marked by an infinite amount of folds of infinitely small depth. It can now be understood why the parallel cross-sectional area was assumed to be constant in §3.3: as the muscle expands, no material that was previously unloaded is inserted, instead, the membrane gradually unfolds towards the equatorial region while every part of it is stressed at all times.

The condition of zero parallel stress led to a surface geometry defined by Eqs. 3.35a and 3.35b. Conversely, if the membrane's surface does not exactly match that, it can be expected that there are stress components in the parallel direction. Keeping the pleats shallow will therefore be important in order to minimize these components.

Friction is avoided by this muscle design. There is contact between membrane material inside the folds but no sliding takes place. Unfolding is a mere taking apart of pairs of layers of membrane while folding is done by pressing them back against one another.

4.2 Design

As is the case for nearly all PAM designs (cf. §2.2), the pleated muscle has two main parts: the membrane and the end closures or fittings. The membrane is the core element. Its inflation–contraction behavior is determinant for the way pneumatic energy is transformed into mechanical energy. Its main distinction is the pleated arrangement. The end fittings serve to close off the membrane ends, to guide the flow of gas, to attach the PAM to its load and to keep the folds in place. With regard to the latter, one can also use the end fittings to arrange the folds equidistantly about the muscle's long axis.

4.2.1 Membrane

As was mentioned in the previous section, the finite depth of the pleats causes parallel stress components. These can be expected to cause stress concentrations at the region around the end fittings: at the points of fastening the deviation from an axisymmetrical surface is much larger than in the equatorial region and this will increase as the membrane bulges. Besides this, it was shown in §3.5 how the zero parallel stress condition led to the highest possible transfer of work when going from zero contraction to an intermediate contraction. Furthermore, strain energy lowers developed tension. For these three reasons, parallel stress components are to be minimized. This has an implication on the shape of the pleats: they have to be made as shallow as possible and arranged in such a way that membrane longitudinal fibers are kept as much as possible in meridional planes as the membrane bulges. This can best be done by using cartridge pleating, which is characterized by having the pleats pointing in the radial direction, as shown by a parallel membrane section in Fig. 4.3(a). The pleats are characterized by their depth t , their pitch b and their number n . Flattening the pleats, as in Fig. 4.3(b), would not be a good solution in this regard: the parallel displacement of a longitudinal fiber as the muscle inflates,

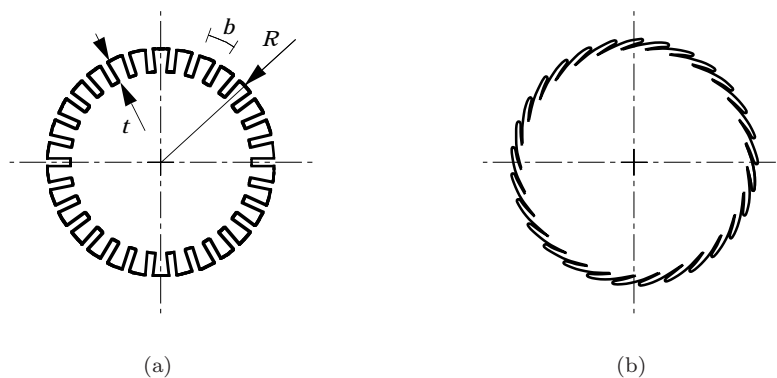


Figure 4.3: Radially (a) and tangentially (b) pointing pleat arrangement.

would be significantly greater with regard to cartridge pleating, and hence, parallel stress components would be equally greater.

In §3.1 it was seen how, in order to assure a uniaxial tension, the membrane's shape must be of a rotationally repetitive pattern. Consequently, the pleats have to be organized equidistantly and equilaterally, meaning all must have the same dimensions. The number of folds can be related to the fold depth, the original muscle radius R and the bulk diameter $ld_{0\max}$:

$$2\pi R + 2nt \geq \pi ld_{0\max} \quad (4.1)$$

If this condition is satisfied, enough material will be available for the membrane to be able to inflate to its full extent. The expression shows how the required number of folds increases as they get shallower. As an example, a muscle of $l = 10$ cm and $R = 1.25$ cm can be considered. With these dimensions and the zero parallel stress and inelastic condition, $d_{0\max} = 0.954$ and

$$\frac{nt}{R} \geq 8.85 \quad (4.2)$$

Choosing a depth of 2.5 mm (one tenth of the initial diameter) thus implies needing at least 45 folds, and a pitch of 1.75 mm ($b = 2\pi R/n$). Halving the depth leads to a doubling of the amount of folds. Due to membrane elasticity, the bulk diameter is somewhat higher than that predicted by the inelastic condition and, therefore, the calculated number of pleats will be slightly undervalued.

Other influencing parameters on the number of folds are related to the technical feasibility of folds of that size. Firstly, the smaller the depth, the harder it will

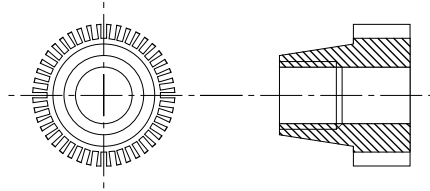


Figure 4.4: Basic end fitting plug.

be to fold the membrane. This is mainly due to the fact that the membrane has a finite thickness and a limited flexibility: a certain fold width is needed for the membrane to straighten out. Assessing this is not easy and is best done empirically. Secondly, during operation, the folds have to be kept in place at the end fittings. As will be shown further, this will be increasingly difficult to do as the pleats get shallower and narrower.

4.2.2 End Fittings

The design requirements that are set for the end fittings follow from their function. The proposed design consists of two parts: an inner part, a plug, that will function as closure, attachment to load and membrane, pressurized gas duct and arranger of the folds, and an outer part, a ring, that will merely serve to prevent the membrane from expanding at its ends.

The basic version of the plug, of which a top view and longitudinal central section is outlined in Fig. 4.4, has a conical side and a toothed side. The conical side serves to secure the membrane. As will be seen later, the membrane will be embedded in a resin between the outer ring and the conical part, making the cone carry most of the developed tension. The teeth's purpose is to have equidistant folds and to keep them in place during operation. By using this configuration the amount of folds is limited because each tooth needs a certain

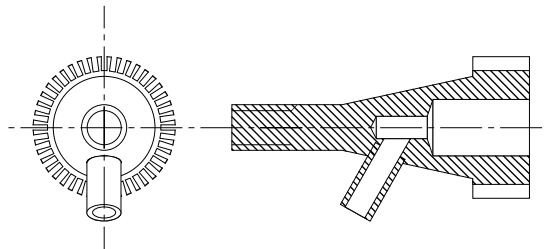


Figure 4.5: Inner part end fitting with gas duct.

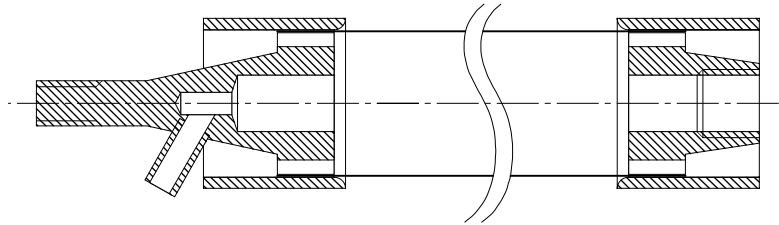


Figure 4.6: Assembly of the end fittings and membrane.

root width for easy machining and strength. The plug has a central bore which is threaded to fasten the muscle to its load. Care must be taken to seal this part in order to ensure gas-tightness.

At least one end closure has to conduct gas. This can be done through the part that is fastened in the bore of the basic plug. In that case care has to be taken to have a large enough bore since typical duct diameters will be at around 4 mm. As an alternative, an adapted version of the plug is designed: it has a prolonged conical part through which a pipe for gas conduction is inserted, and which tapers to a threaded rod for load attachment. This gas conducting version is shown in Fig. 4.5.

Both plugs are inserted in a ring, as shown in Fig. 4.6. This ring is mainly loaded by the lateral pressure load resultant. Since this has a relatively low value compared to maximum muscle tension, the ring will have a low wall thickness.

4.3 Materials Selection

4.3.1 Membrane

Criteria

The technical requirements that are to be met for the membrane material are set by the geometric design, the operational conditions and the assembling of the PAM.

The main design feature is the pleating, which demands a good flexibility and low brittleness, in order to fold easily and prevent cracks due to flexing. Furthermore, the material properties must not be altered due to the folding. A second important design feature is the separation of membrane and end closures. Because of this, the membrane has to be fixed to the closures and this has to be done easily and reliably. It can be done either by bonding or by clamping.

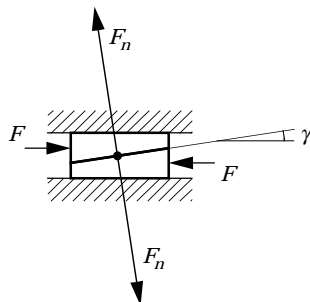


Figure 4.7: Clamp force F_n related to load.

Clamping could be done between two conical rings having a small enough inclination angle so that it will be self-gripping. The problem with this type of fixing, however, is the risk of having an exceedingly high clamping force when friction is too low. The relation between load F and clamp force F_n , cf. Fig. 4.7, as a function of cone angle γ and friction angle ρ is (Matek et al., 1993)

$$F_n = F \frac{\cos \rho}{\sin(\gamma + \rho)} \quad (4.3)$$

If friction between the cone walls and the membrane is low, a very sharp cone angle will be necessary and, consequently, the surface pressure acting on the membrane will rise enormously. This can cause problems with regard to material compressive strength. Choosing clamping as a fixing method would require the membrane to have a high transverse compressive strength and a reasonable friction coefficient between clamps and membrane.

Choosing bonding instead of clamping imposes other technical requirements. The bonding material has to stick firmly both to the membrane and to the plug. This way of fixing has been chosen for the Pleated PAM, as is clear from the design of the plugs.

The technical requirements set by the operational conditions are:

- high tensile stiffness and high strength, in order to minimize strain energy and membrane thickness;
- good wear and tear resistance, to ensure a long life under cyclic operation;
- low creep/relaxation, to retain initial sizes;
- good fatigue resistance, because of the cyclic operation;

- gas-tightness;
- safety, hazard free use;
- low influence of environmental factors, such as moisture, heat, light, oxygen, to ensure reliability;

Assembling all the parts needs the membrane to be easy to manipulate. This means it must be easy to fold, the folds must hold once they have been put, and, generally, the membrane must be easy to handle.

Finally, the commercial availability of the material can be considered: the purpose is to build the Pleated PAM using off-the-shelf parts as much as possible.

Selection

Structure. The first choice to be made in selecting the Pleated PAM membrane material concerns using a fabric or a sheet. The advantage of a sheet is its gas-tightness. Its disadvantage, however, is its lesser ability to handle the stress concentrations and non-uniformities that will be present at the ends. At these points the membrane will be folded about two lines when it bulges: a meridional line and the parallel circle. These will lead to small wrinkles in those locations, each of which will be a potential point of material failure, especially in cyclic operation.

A fabric is a woven or laid cloth made of yarns and, as such, it shows the ability to have small scale rearrangements of its yarns in order to adapt itself to the stress field it is exposed to. Therefore, a fabric is better qualified to handle the non-uniformities in stress at the end fittings.

The most common weave construction is the plain weave, shown in Fig. 4.8(a). It is characterized by a repeated pattern of one over and one under. The two weave directions are the warp and the fill or weft direction: warp is the long direction of the weave, while fill is parallel to the width of the weave. During weaving the warp yarns are tightly stretched, while the fill yarns are interwoven on them and, consequently, bent about them. As a result of this, the warp yarns usually are more straight than the weft yarns and therefore the warp direction should coincide with the Pleated PAM's longitudinal direction. Other types of weave are the basket weave (Fig. 4.8(b)), which is a plain weave of pairs of yarns, the satin weaves such as 5-harness satin, which has a one over, four under construction (Fig. 4.8(c)), and the unidirectional weave (Fig. 4.8(d)).

Weaving induces a non-linear tensional behavior because of the periodic interlacing. The yarns are not straight because of this and when tensioned they will gradually straighten out, depending on the direction of the load. In the

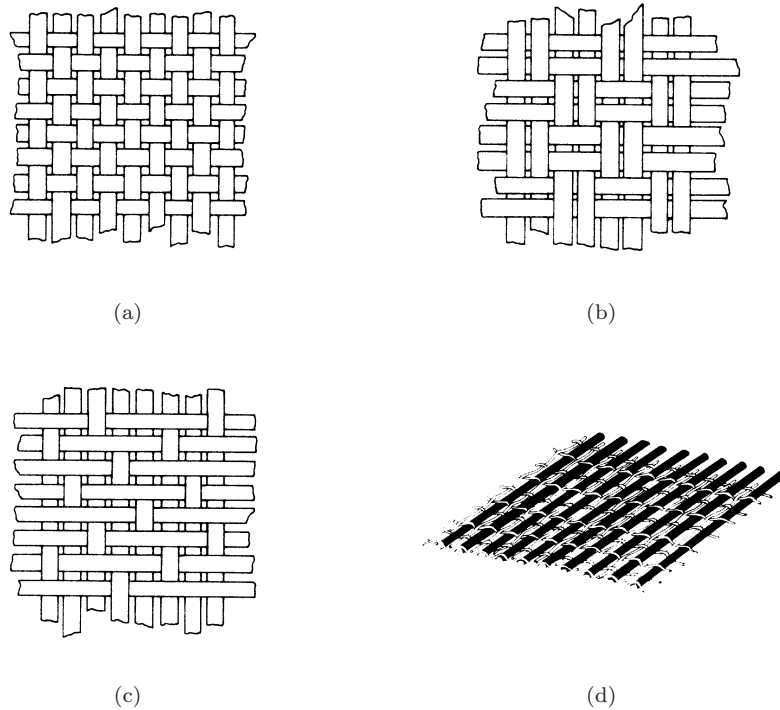


Figure 4.8: Plain (a), basket (b), 5-harness satin (c) and unidirectional (d) weave construction. (Reinhart et al., 1988)

case of the Pleated PAM stress will occur mainly along one yarn direction. As stress increases the yarns in this direction will be straightened but the yarns in the parallel direction will resist this. Because of this, the longitudinal yarns will always be slightly bent about the parallel yarns. The importance of this effect depends on the type of weave. Satin weaves and unidirectional weaves, obviously, are less influenced by warp yarn straightening than plain weaves.

A fabric is not gas-tight and has to be made so. To this end, it either has to be impregnated with a sealant or bonded to a lining. The latter does not bring about the same problems as using a sheet instead of a fabric would, because the lining can be chosen thinner and more compliant than the fabric and therefore it will not be exposed to the same amount of stress. A fabric is slightly more difficult to manipulate before it is sealed, because of the easy yarn slippage and fabric distortion. After lining, however, the fibers will be immobilized and handling the resulting membrane is the same as handling a sheet.

Fabric Material. The next choice concerns the fiber material. To make this choice, the fiber groups as presented in Reinhart et al. (1988) were considered. These are glass fibers, carbon/graphite fibers, boron and silicon carbide fibers, ceramic fibers, metallic fibers and organic fibers. All groups except the organic were rejected:

- glass fibers because of their brittleness and lesser wear and tear resistance;
- carbon or graphite fibers also show a high degree of brittleness and furthermore, they need to be fully embedded because of the hazards they induce (health, electronic short-circuit);
- boron and silicon carbide fibers are too expensive compared to other fiber types;
- ceramic fibers are intended to be used in high temperature environments and are usually too expensive;
- metallic fibers have a tendency for corrosion, although this could be minimized, their tensile elongation at break is only about 1%.

Organic fibers, which are polymer fibers and include e.g. Nylon, usually have a high creep and stress relaxation tendency. This would make this class of fibers equally unsuited. However, belonging to this group, a class known as liquid crystalline polymers delivers fibers whose polymer chains are aligned in the fiber axis direction. This has a beneficial effect on strength and creep behavior in the fiber direction. It also makes the structure anisotropic, with a higher strength and elasticity modulus in the fiber axis direction compared to the transverse direction, and fibrillar. One such polymer is an aromatic polyamide (aramid) that is generally known by one of its product names, Kevlar—another product name of the same para-aramid polymer is Twaron. Its chemical composition is poly para-phenyleneterephthalamide. It is also known as PPD-T resulting from the chemical reaction by which it is made, namely a condensation reaction of paraphenylene diamine and terephthaloyl chloride. A thorough description of this fiber and its characteristics can be found in Pipliacampi (1988), Shaeffgen (1983), Wilfong and Zimmerman (1977) and the data manual for Kevlar 49 Aramid.

Kevlar, which is fabricated by E. I. Du Pont de Nemours & Company, Inc., has a specific weight of 1440 kg/m^3 and is spun in filaments of $12 \mu\text{m}$ diameter. Three varieties exist, depending on the degree of molecular orientation: Kevlar 29, 49 and 149. They show linear elastic behavior with axial elasticity moduli at 83 GPa, 131 GPa and 186 GPa, respectively, their axial tensile strengths 3.6 GPa, 3.6–4.1 GPa and 3.4 GPa, and their axial tensile elongation at break

4.0%, 2.8% and 2.0%. These values differ slightly between references and should therefore be taken with care. As a comparison, a solid machinery carbon steel rod has a Young's modulus of 210 GPa, a tensile strength of, typically, 0.5 GPa. Its elongation at break, 10–20%, is much higher.

Para-aramid wear and tear resistance is very good. The material is described as very tough and general damage tolerant, non-brittle, and showing non-catastrophic failure (unlike glass and carbon). The reason for this seems to be the crack propagation mechanism: due to the fibrillar structure this will be along the filament axis and not across it. The non-brittleness and the 12 μm filament diameter make it an apt material to be folded. Its high parallel molecular arrangement results in an extreme smoothness. This is one of the reasons why an early Pleated PAM design using the pleating shown in Fig.4.3(b) and a conically clamping end fitting was rejected: a cone angle of 1° was not low enough to secure the membrane, but clamping pressure at this low an angle was so high that it damaged the membrane.

Creep is very low and comparable to that of glass fiber: at a loading of 50% of strength, creep equals 0.1% in 50 years. Most of the creep will happen more or less immediately, at a time scale of seconds and minutes rather than years. The reasons for such a low creep are to be found in the high polymer crystallinity and its high molecular weight. Fatigue resistance is very good: maximum allowable yarn stress diminishes from 2000 MPa for 10^3 cycles to 1750 MPa for 10^7 cycles.

As for safety and hazard free use, no special warnings or recommendations are reported. No problems are created for electrical equipment since para-aramid is an electric insulator.

The performance of the para-aramid fiber in hot conditions is very good: 80% retention of properties after 81 hours at 200 °C and nearly no influence at 150 °C for long time exposure is reported. Long exposures to higher temperatures causes a gradual oxidation of the filaments. The effect of moisture at room temperature on tensile properties is less than 5%. Exposure to strong acids and bases will cause a chemical degradation of the fibers. This does not pose a problem for this application since PAMS are not intended to be used in such an aggressive environment. Prolonged exposure to sunlight will cause a significant loss in strength. A value of 51% retention after a 5 weeks Florida sun exposure is reported by Du Pont.

Para-aramid fabrics are commercially available in many weave types, woven from many yarn sizes. Choosing one has to be done considering strength and structural stability. Too loose a weave will easily distort during manipulation before lining. On the other hand, the looser the weave, the more linear its tensile behavior.

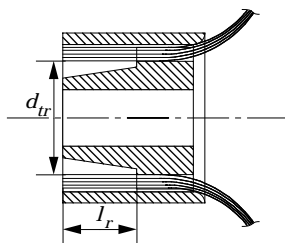


Figure 4.9: Epoxy shear stress surface.

Bonding Material. Bonding the membrane to the end fittings can easily be done by using an epoxy resin. Using diglycidyl ether of bisphenol-A epoxy (DGEBA epoxy) and an anhydride or aromatic amine as a curing agent is recommended by Du Pont. As a measure of filament to resin adhesive quality a short beam shear strength of 50–70 MPa for a unidirectional reinforced composite of fiber fraction 0.6 is given by Du Pont. A number of factors influence this value, e.g. curing procedure and void content, and therefore they should be used with caution. Curing can be done at room temperature and takes about 48 hrs. Adhesion of this resin to metals, such as aluminum, is very good.

Membrane tension is guided from the membrane to the epoxy resin. The epoxy and the para-aramid fibers form a unidirectional composite that is mainly loaded by shear stress parallel to the fiber direction. It is unidirectional because in this embedded region the fabric's weft yarns are removed to ensure a better contact between fiber and resin. It is loaded mainly by shear stress because the outer ring forces the fibers to enter the resin in a line parallel to the long axis, whatever the state of muscle inflation, as shown in Fig. 4.9. Assuming the fibers to be uniformly arranged in a ring whose thickness is the same as the tooth height, the highest shear stress will occur on the inner surface of this ring, whose diameter coincides with the teeth's root diameter d_{tr} and whose height is represented by l_r . Assuming furthermore a uniform stress distribution across this cylindrical surface, the shear stress can be calculated and compared to the shear strength:

$$\tau_{sr} = \frac{F_t}{\pi d_{tr} l_r} \leq 50 \text{ MPa} \quad (4.4)$$

Actual stress levels will be lower than the value thus calculated because of the supportive action of the teeth. Eq. 4.4 will however be used because of the uncertainty concerning the exact value of shear strength and stress concentrations.

Lining. In order to seal the fabric it has to be lined. The lining has to be extremely thin if fabric behavior is to be maintained. At the same time it must have enough strength to withstand the pressure load acting on the surface. Thirdly, it must be able to deform substantially in order to allow the local yarn rearrangements to happen. It must have a good wear and tear resistance because of the repeated folding and unfolding along the same lines. Finally, it must be securely and reliably bonded to the Kevlar fabric.

A biaxially oriented polypropylene film backing and pressure sensitive rubber-resin adhesive have been chosen to meet these demands. The backing's thickness is $28\ \mu\text{m}$ and that of the adhesive layer $20\ \mu\text{m}$. As the adhesive will penetrate somewhat between the yarn fibers, the lining's thickness when applied will be even lower. It has a minimum elongation at break of 80% and a tensile strength of 50 N/10 mm. Fabric gap sizes are typically a few tenths of mm wide and a few mm long, so their surface area is in the range of $0.1\text{--}1\ \text{mm}^2$. At a gauge pressure of 500 kPa, this would mean a surface load of 0.05 N to 0.5 N for a surface circumference of a few mm. These values are very small compared to the tensile strength so only marginal interyarn bulging of the lining will occur. Because of the biaxial orientation, the extreme thinness and the high elongation at break, this lining has a very good wear and tear resistance and is well suited to be folded.

The film's resistance to moisture and chemicals is good. The adhesive on the other side has a low resistance to solvents, but these are presumed not to be present in the PAM's operational environment. An acrylic adhesive could be chosen instead if this would be the case. Temperatures of up to 100°C are withstood by the rubber adhesive.

A thus obtained lined Kevlar fabric is very easy to handle. In fact, it could be compared to handling paper sheets.

4.3.2 End Fittings

Strength, low weight and ease of fabrication are the most important criteria for the end fittings. In order to assess strength, loads have to be identified first. This is by no means easy: membrane tensile stress is transferred via a path running through the epoxy filling and the plug. What the resulting stresses will be at all plug locations is difficult to predict. Not only because of the complexity of composition but also because of its dependance on the quality of assembling. The threaded part of the plug carries the full muscle tension and this is the only part whose load can be accurately determined. The distribution of load to the other parts is less clear. If the plug and the resin filling would be a uniform entity, this would mainly be loaded by shear stresses parallel to the muscle axis. Using different materials that are bonded induces extra stress

components and, depending on the bonding behavior and on the difference in material behavior, their importance will vary.

If the bonding is very compliant with regard to the rest of the materials, strain along the boundary surface between cone and resin will be significant and, consequently this surface will be loaded by a clamping force (cf. Fig. 4.7). Part of the muscle pulling force will then be put onto the teeth's faces and the narrow ring-shaped surface at their root, and this will add shear and bending stress components in cylindrical sections of those parts of the plug. Support will also be given by the outer rings, which will be loaded by the transverse component of the total membrane surface pressure and, to a lesser extent, by the clamping force. How much each stresses contribution is, depends on the geometry, the material constants, the adhesion quality and the quality of the resin filling, and is therefore difficult to predict.

In view of the numerous notches—two for every tooth—a ductile material is advisable for the plug. This has the property of local plastic deformation to relax peak stress levels. In order to keep the weight and cost low, aluminum alloys seem adequate: tensile strengths of 300 MPa at a density of only 2700 kg/m³ and moderate cost are possible (Matek et al., 1993; Carvill, 1993). Machinability can be very good if the right alloy is chosen. Aluminum alloys are characterized by having an oxide coating which protects them against water and atmosphere, therefore, corrosion is not a problem. Ductile behavior, good machinability, low corrosion and high strength are also characteristics of copper and its alloys. The drawback of copper, however, is its high specific weight of 8900 kg/m³. For small parts this is not very critical and the use of copper could then be justified. Using plastics or composites would not reduce the weight much further because tensile strength of these materials with regard to their specific weight is often lower than that of aluminum alloys.

Muscles of the same slenderness and scaled membrane thickness are subjected to identical stresses, as was seen in §3.4, Eq. 3.51, and therefore, strength calculations and material choices only have to be performed once for each slenderness. If muscle broadness increases, it was seen that force per end fitting circumference length decreases and, therefore, the cross-sections of plugs of broader muscles can be taken smaller.

4.4 Assembly

When putting all parts together, special attention has to be given to fold and yarn alignment with the actuator axis. First of all, the direction of weave has to be such that its warp direction will be parallel to the actuator axis and its weft direction perpendicular to it. All warp yarns must be cautiously kept

perfectly parallel to each other before attaching the lining to the fabric. Once the lining is attached, the fabric will be stabilized and more robust handling will be allowed.

The folds are then put in along the yarn direction. This leads to a folded piece of membrane that needs to be cylindrically closed. This is done by overlapping two or three folds which are fixed together by a layer of the same adhesive used for the lining. Because of the minor parallel stress, only one fold overlap would be sufficient. Using two or three is done as a precaution: if during the assembly the yarns of the overlap are not equally taut an enhanced bulging of the slacker yarns can occur when the actuator is pressurized and this will break the overlap adhesion and thereby destroy the fixing and the gas-tightness. The end fitting teeth gaps that guide the overlapping folds are widened in order to insert the double amount of membrane material. This will not create a problem of tooth strength because the tooth's face and, consequently, its load will decrease accordingly.

The end plugs are inserted in the thus obtained sleeve which is then stuck into the outer rings. Taking care of alignment is done by using a threaded mandrel onto which the plugs can be exactly positioned. The lining is not applied in the greater part of the zone that is to be embedded in the epoxy resin, since it would only deteriorate impregnation and adhesion. To ensure gas-tightness a 2 mm wide strip of the lined fabric is embedded. The weft yarns are removed from the impregnated part to assure an optimal bonding between the epoxy resin and the para-aramid fibers. Curing takes about 48 hrs and is done at room temperature, no post-curing is necessary.

4.5 Summary

The concept of the Pleated PAM was introduced in this chapter. It was seen to be an approximation of the zero parallel stress case of axisymmetrical membranes, which was derived in Chapter 3. The muscle can expand and contract by unfolding axially arranged pleats, the more pleats it has the better the approximation is. The design of the Pleated PAM was discussed, in particular the end fittings design and the type of folding. Cartridge pleating was suggested to be the best type of folding.

The materials for the end fittings and membrane were selected considering criteria set by design, strength, operational conditions and assembly. A fabric composed of high tensile stiffness para-aramid fibers—product names Kevlar, Twaron—was chosen as main membrane constituent. Because a fabric is not gas-tight, a liner has to be applied to it in order to seal it. For this a polypropylene film was selected. Bonding by an epoxy resin was proposed as a good

solution for connecting the membrane to the end fittings. As end fitting materials aluminum or even copper were seen to be good choices, the advantage of aluminum over copper off course being its low weight.

This chapter was concluded by a short discussion about the assembly of all muscle parts. Yarn alignment, fold overlap at the seam and resin casting were shown to need special care.

Chapter 5

Prototype: Design and Characteristics

Pleated PAM trial models of the two basic pleat arrangements—cartridge and flattened, cf. §4.2.1—were built and tested. It has already been mentioned earlier that the flattened pleats arrangement was rejected because of the exceedingly high clamping pressure, cf. §4.3.1, p. 69, and the enhanced parallel stress inherent to this type of pleating, cf. §4.2.1. These effects were observed experimentally as membrane slipping between the clamping cones and as early membrane failure near the clamping. A number of cartridge pleated muscles of sizes ranging about a rest length of 10 cm and diameter of 3 cm and of different weave sizes and end fitting designs were tried. This led to the final design discussed §4.2.2, of which prototypes of $l = 10$ cm and $R = 1.25$ cm were made. These were used as actuation elements in a dynamic antagonistically operated effector and therefore their design specifications and characteristics will be fully covered in this chapter.

Choosing their size resulted as a compromise between a number of considerations. Slenderness was maximized in order to have a high travel at a fairly low tension. That way, when covering full travel, a fixed amount of work can be transferred at a minimum stress load for the structure onto which the muscle actuators are connected. Slenderness has to be limited, however, because of practical considerations. As slenderness increases, the folds will need to be more tightly packed because, due to the increasing ratio of expansion, more material has to be gathered onto a relatively smaller diameter. At a certain point, this will not be technically feasible any more: fold width or tooth width will become too low and the assembly of the membrane and the end fittings will be impracticable. As slenderness increases, stress levels in the end fittings and resin filling increase and, consequently, material strength problems will arise.

The values of actuator volume had to be high enough to transfer a reasonable amount of work. On the other hand, the actuators are controlled by servo-

valves, regulating gauge pressure (cf. §2.3.2), which determine the dynamic behavior of the actuator. Too high a volume will slow down the building up of pressure by the valves.

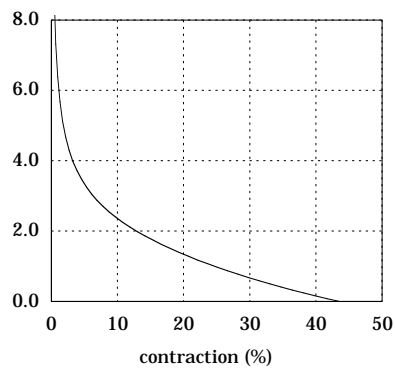
From the inelastic state (cf. §3.4) a number of actuator characteristics can be estimated. From these, a choice of fabric size was made. Once the membrane sizes are known, its parallel cross-sectional area and therefrom its compliance a , as defined in §3.3.1 can be determined. That way, the influence of membrane compliance can be checked and, if necessary, corrections can be made.

5.1 Membrane Size

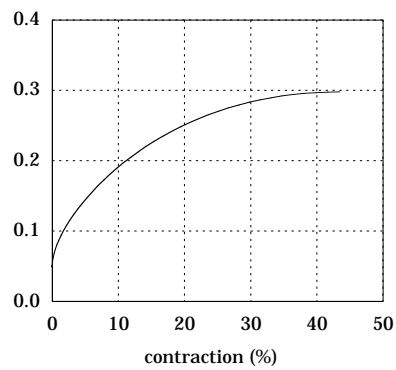
Figs. 5.1(a) to 5.1(d) show the results of calculations under the assumption of inelastic behavior and at a gauge pressure of 300 kPa. Travel is found to be at 43.5%. The diameter increases from 2.5 cm to 9.54 cm, which would require at least 45 folds, as was already mentioned in §4.2.1, if fold depth is 2.5 mm. A shallower fold would impose practical problems: at 2.5 mm depth and a resulting pitch of 1.75 mm, the distance between the folds along the membrane is 6.75 mm and this is found to be very close to the limit of practicability. Moreover, machining the toothed side of the plugs will become increasingly difficult as the pitch gets smaller. Because the prototype folding is done by hand, a fold width of 7 mm instead of 6.75 mm was chosen. This means that 44 folds would allow for a bulk diameter of 9.8 cm and should therefore suffice.

The stressed length or total membrane circumference was thus set at a value of $44 \times 7 = 308$ mm. From this and from the stress resultant—meridional stress integrated throughout a membrane parallel cross-section—the minimum membrane thickness can be calculated. Since a fabric is used, fiber cross-sectional area per unit length rather than thickness is used. At a contraction of 2% and gauge pressure at 300 kPa, the stress resultant is 5.3 kN, cf. Fig. 5.1(d), which results in a tensional membrane load of 172 N/cm. With tensile strength of Kevlar 49 at 3.6 GPa, this would mean a fiber cross-sectional area of 0.048 mm² per cm would be the lower limit. This is an extremely low value and was rejected for several reasons. First of all, care has to be taken because of stress non-uniformity. Secondly, the material properties' values presented by the data manual and other sources are standardly obtained from tests performed on resin impregnated strands. In this application, however, the filaments are only impregnated at their ends. Not only is the behavior of a naked yarn different from that of an impregnated but, more importantly, at the boundaries of impregnation, notches are created by fixing and by possible sharp resin edges. These effects were observed experimentally as the gradual snapping of yarn filaments as the load was increased above a certain point.

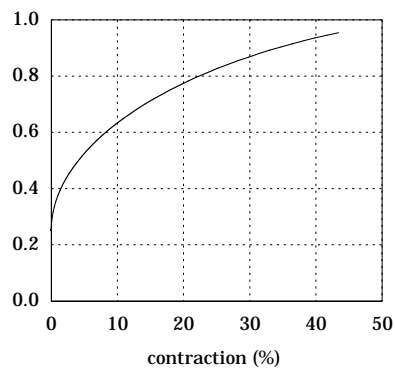
A plain weave of 13.5 yarns per cm in both weave directions and a fiber cross-sectional areas of $0.21 \text{ mm}^2/\text{cm}$ was the first choice. The thickness of this fabric is only 0.13 mm, which would make it ideally suited. The total membrane cross-sectional area A , using this weave equals 6.5 mm^2 . At an unpressurized state, this weave would break, according to the Kevlar manual data, at a tensional load of 23.4kN. Experiments showed a gradual failure at much lower loads: fiber snapping started at a load of 1.5–2.0kN.



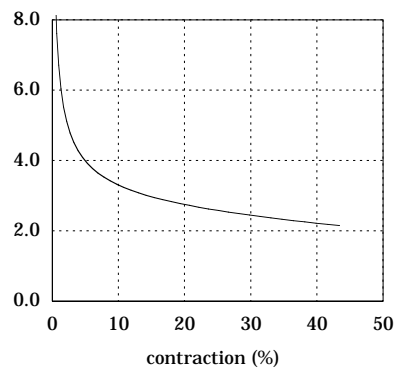
(a) Tension (kN).



(b) Volume (l).



(c) Equatorial Diameter (dm).



(d) Stress Resultant (kN).

Figure 5.1: Prototype muscle characteristics.

For these reasons a plain weave of 9 warp yarns per cm and 5.5 weft yarns per cm and fiber cross-sectional areas of $0.98 \text{ mm}^2/\text{cm}$ warp and $0.08 \text{ mm}^2/\text{cm}$ weft was chosen. The total membrane cross-sectional area A then equals 30.2 mm^2 . Warp yarns are tightly packed at an inter-yarn gap of less than 0.1 mm, whereas the fill inter-yarn gap is about 1.7 mm wide. At these small sizes, no problems are to be expected regarding inter-yarn bulging of the lining. Warp yarns contain roughly 1000 filaments each, while weft yarns only contain 134 filaments each. The strong difference between warp and weft yarn sizes and density is allowed since parallel stresses are very low. It has the beneficial effects of lowering the overall fabric thickness and making the fabric behave more like a unidirectional weave. Fabric thickness is 0.2 mm, to which the lining's thickness has to be added. Using a double layer of the lining a total membrane thickness of 0.28 mm was measured.

Membrane compliance can now be determined: $a = \pi p R^2 / A E_1 = 3.9 \times 10^{-5}$ at a gauge pressure of 300 kPa. This is a very low value (cf. §3.4) and even if the actual elasticity modulus has to be taken at only a tenth of its data manual value, a will still be sufficiently small to disregard elasticity effects.

5.2 End Fitting Sizes

Assuming a uniform distribution of load, single filament shear stress at the interfacial bond can be estimated as the muscle tension divided by the number of filaments and the filaments facial surface. From the values cited earlier the number of filaments equals $30.8 \times 9 \times 1000$ and the filaments embedded facial surface $\pi \times 12 \times 10^{-6} \times l_r$. Shear stress is thus

$$\tau_{sf} = \frac{F_t}{10.45 l_r} \quad (5.1)$$

For a maximum muscle tension of 5 kN (gauge pressure 300 kPa and contraction 2%) and an impregnated length of 10 mm, this yields $\tau_{sf} \approx 50 \text{ kPa}$. As is the case for all fixings, the gripping force acting interfacially will be non-uniformly distributed, with a maximum near its edge. Allowing a factor of 10 to take this effect and other non-uniform load distributions into account still yields a very low shear stress on each filaments face.

In order to have an adequate support of membrane folds and to keep the fibers' inclination at their resin fixing at a minimum, a tooth length $l_t = 10 \text{ mm}$ was chosen. The outer ring projects 2 mm from the toothed edge of the plug and is rounded off to prevent sharp filament flexing. The radius is set at 2 mm, this way the bending strain resulting from a right angle flexion of a filament about the ring's edge will be equal to the ratio of the filaments shaft radius to

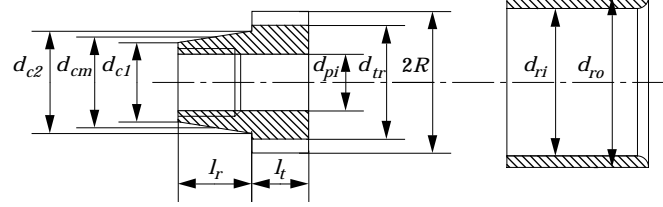


Figure 5.2: End fitting size definitions.

the rounding-off radius, which equals 0.003 and is very low compared to the tensile strain at break (0.029). A total ring height of 25 mm was chosen, making $l_r = 13$ mm. The lined part of the membrane can, consequently, protrude a few mm into the resin, which is necessary to seal off the membrane.

Resin shear stress can be determined from Eq. 4.4 and the sizes chosen thus far: $\tau_{sr} = F_t \times 1.2 \times 10^3$, which would limit muscle tension to 40.8 kN. In principle, the membrane itself can withstand a still higher force: its total section is 30.2 mm^2 and its ideal tensile strength 3.6 GPa and thus it should only break at a load of 108.7 kN. As explained earlier, these values should be taken with caution but they do indicate that the snapping of filaments at their resin fixing and the failure of the resin filling due to shear stress loading will cause muscle failure at increasing muscle tension rather than membrane yarn failure at other locations.

The tooth gap width was chosen at 1 mm, which allows an easy assembly of membrane and plugs. The root sections of the teeth thus have a surface of $(\pi d_{tr} - 44)/44 \times l_r = 4.3 \text{ mm}^2$ each, which makes a total of 188 mm^2 . They are loaded by part of the pulling force due to the contact between their faces and the resin. This causes shear stress and normal bending stress acting on the root sections. At a loading of 5 kN and assuming a uniform distribution, shear stress would thus equal 27 MPa. The normal stress, under the assumption of a linear distribution ranging from maximum to zero along the roots length, can be found from expressing the bending moment equilibrium about the far end of the root and would be 11.5 MPa. These values are sufficiently low for a high strength aluminum to be regarded as harmless. Moreover, a small ring 1 mm wide was added at the transition of cone to teeth in order to increase the load carrying surface and thus relax the axial tooth load.

If the tooth support and the bonding of epoxy resin to aluminum would fail completely, the epoxy filling and the conical part of the plug would be loaded by a clamping force and surface pressure p_S , as was explained at the beginning of this section (cf. Fig. 4.7). Besides the surface pressure at the boundary of the filling and the cone, this results in a tensile normal stress acting on the

meridional sections of the filling, and in a compressive normal stress acting on a meridional section of the plug. It is difficult to predict their exact value since the friction coefficient between the metal surface and the epoxy surface is not well known. It is safe, however, to neglect the influence of friction—putting $\rho = 0$ in Eq. 4.3—since this leads to an overestimate of the surface pressure. The maximum of the normal stress acting on the resin, assuming uniform surface pressure, will occur at the boundary of epoxy and plug near the teeth and will be (Matek et al., 1993)

$$\sigma_{nr} = p_S \frac{d_{ri}^2 + d_{c2}^2}{d_{ri}^2 - d_{c2}^2} \quad (5.2)$$

with the surface pressure determined from Eq. 4.3 and the cone surface area

$$p_S = \frac{F_t}{\pi d_{cm} l_r \tan \gamma} \quad (5.3)$$

and the diameters defined as in Fig. 5.2. The maximum of the normal stress acting on the plug will occur at its inner narrow end and will be (Matek et al., 1993)

$$\sigma_{np} = p_S \frac{2d_{c1}^2}{d_{c1}^2 - d_{pi}^2} \quad (5.4)$$

again with the diameters defined as in Fig. 5.2. These values are too high an estimate, not only because of the above mentioned reason, but also because the plug is supported on its inner side by the part via which power is transferred to the load and which is fastened in its narrow side, and because the resin is supported on its outer side by the outer ring. The sizes, as chosen, are: $d_{pi} = 10$ mm, $d_{c1} = 14$ mm, $d_{cm} = 16$ mm and $d_{c2} = 18$ mm. The outer ring inside diameter is $d_{ri} = 26$ mm, that way a 0.5 mm clearance is created to allow the membrane to fit between the teeth's heads and the outer ring. With these values, $p_S = F_t \times 10^4$, $\sigma_{nr} = 2.84 p_S$ and $\sigma_{np} = 4.08 p_S$. For $F_t = 5$ kN, this yields $p_S = 50$ MPa, $\sigma_{nr} = 142$ MPa and $\sigma_{np} = 205$ MPa. For the plug, this poses no problem, but the resin can be loaded excessively this way. A typical value of the tensile strength of a unidirectional epoxy perpendicular to the fiber direction, from the data manual Kevlar 49 Aramid, is only 30 MPa (the compressive strength in the same direction 140 MPa). This means that, although the calculated stress values are overestimated, care has to be taken to get a good bonding at the cone's face and force has to be limited.

The last part of the plug that had to be checked is the thread. ISO metric thread of 10 mm nominal diameter and 1 mm pitch (M10×1) and a height of 10 mm was chosen for the basic plug. M8×1 was chosen for the gas conducting plug.

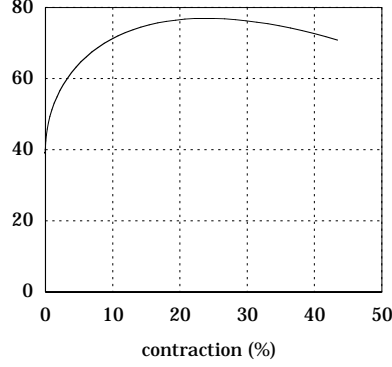


Figure 5.3: Radial component of meridional stress at end fittings (MPa).

The threads carry the full pulling force and are thereby mainly loaded by shear stress and by surface pressure. Using nuts of 5 mm height on the M8×1, the shear stress will be 40 MPa at 5 kN tension. This value is well within material strength limits. M8×1's thread depth equals 0.54 mm and thus thread surface $5 \times 0.54 \times \pi \times 8 = 68 \text{ mm}^2$. Surface pressure will then equal 74 MPa, which, by all standards, is a low value. Nut height will actually be larger than 5 mm, reducing thread stresses even further.

The outer ring's outside diameter was chosen at 30 mm, this way it has a wall thickness of 2 mm. The ring is loaded by an internal surface pressure due to the radial strain of the resin filling and a normal tensional stress acting on meridional sections due to the same strain and to the radial component of the membrane gas pressure. This component equals the integral of the radial component of meridional stress throughout an end closure half circle:

$$F_r = \int_0^{\pi} (\sigma_1 s \sin \beta_R) \sin \alpha R d\alpha = 2sR \sigma_1 \sin \beta_R = \frac{A}{\pi} \sigma_1 \sin \beta_R \quad (5.5)$$

with s the equivalent membrane thickness at the end fittings. The evolution of $\sigma_1 \sin \beta_R$ with contraction for the inelastic case, is plotted in Fig. 5.3. It has a maximum of 77 MPa at an actuator contraction of about 24%. F_r loads a meridional cross-section of the ring, which has an area of $2 \times 50 \text{ mm}^2$. This leads to a normal tensional stress of only 7.4 MPa, which leaves plenty of margin to support the resin.

From the sizes and the material densities, which are 2700 kg/m^3 for aluminum, 1230 kg/m^3 for epoxy resin and 158 g/m^2 for the fabric, the weight of all parts can now be determined:

- fabric: 7.3 g for 0.046m²;
- basic plug: 12.5 g for 4630mm³;
- resin filling: 1.8 g for 1457mm³;
- outer ring: 11.2 g for 4400mm³.

The total prototype weight, using two basic plugs is thus 58.3g. Using the alternative plug increases the weight somewhat, but if the connecting parts of actuator and structure are included, this will not make any difference. Using copper (density 8900kg/m³) instead of aluminum for the plugs the weight is increased to 115.7g. This still is a low value for an actuator capable of transferring forces as high as 5 kN.

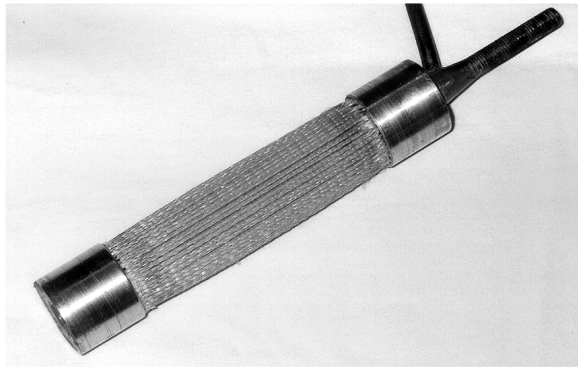


Figure 5.4: Pleated PAM photograph.

A photograph of a prototype Pleated PAM having one basic plug and one gas conducting plug, as in Fig. 4.5, is shown in Fig. 5.4.

5.3 Characteristics

The prototype Pleated PAM was tested on a draw bench at static and isobaric conditions to obtain its traction and equatorial diameter as a function of contraction and gauge pressure. These are in fact the only characteristics that are easily measured; how to determine volume and membrane stress is not at all straightforward. Comparing the experimental data of force and diameter to the calculated will, however, allow to appraise the model. If the model is found to be accurate enough, the calculated estimates of volume and stress can be

taken as reliable. It will not be possible, this way, to determine the parallel stress components. The stronger the deviation between the predicted and the measured values, the more important the parallel stress will be.

5.3.1 Experimental Set-up

The prototype muscle was clamped in the draw bench and fed with pressurized air through a pressure regulating servo-valve. The valve type is KPS 3/4 manufactured by Kolvenbach KG, its specifications, as is the case for all other instrumentation, are listed in Appendix C. The value of the output pressure, expressed in bar, of this valve will equal that of signal input voltage, expressed in volts. Its accuracy, according to the manufacturer, is better than 10 mbar or 1 kPa. The valve has a pressure reading output but the manufacturer mentions an error of 2% on this signal and an offset of approximately 150 mV. In order to have reliable and reasonably accurate measurements, monitoring the pressure is therefore necessary. A silicon diaphragm strain gauge pressure sensor, type Data Instruments XCA5-60GN was used to this end.

The pulling force was measured using a piezoelectric load washer Kistler Type 901A together with a charge amplifier Kistler Type 5001. The output of the amplifier can be set according to the sensor. In this case an output of 1.0 V for a load of 100 kg or, since the washer's sensitivity is 43 pC/kg, 1.0 V per 4.3 nC, has been set. A piezoelectric sensor is not normally used for static measurements, but the input resistance of the amplifier can be set at so high a value that time constants of 1000 s to 500000 s are reached. This is due to the high input resistance of the amplifier, $> 10^{14} \Omega$, and the high insulation resistance of the load washer, $10^{14} \Omega$, leading to a maximum charge leakage of 0.03 pC/s. Because of the value of sensitivity and because each run—measuring traction throughout the actuator travel—takes about one to two minutes, the quartz sensor and charge amplifier could effectively be used as a force sensing equipment in these experiments. This was also observed experimentally: at the end of each run the muscle and washer were completely relaxed and the remaining output of the amplifier was checked, this never exceeded 10 mV or 1 kg.

The equatorial diameter was measured using a Vernier caliper gauge. Measuring circumference or using an outside micrometer were also tried but these methods were rejected because of their unwieldiness and inaccuracy. Using a Vernier caliper proved to be a reliable, quick and accurate way of determining the diameter. The flattened jaws allow measuring the diameter at the ridges of the surface at all times, which improves the consistency of the measurement. Furthermore, by slightly moving the gauge up and down one can assure oneself of having a contact at both sides of the gauge that's loose enough not to squeeze

the membrane and thereby influencing the measured quantity. Squeezing will be less of a problem as gauge pressures increase. All in all, care has to be taken when measuring the diameter this way.

Displacement was measured using a 50 mm dial gauge. A problem that arises when measuring this quantity is the exact determination of the actuator's full length and hence the point of reference for displacement. During the assembly, small misalignments can cause deviations on the sizes that make it difficult to determine the exact length at rest. A declination of only 2° of one end fitting ring with regard to the long axis leads to a deviation of 0.5 mm on the length on each side of the muscle with regard to the nominal length. This will already cause a possible absolute error of 1% on the determination of contraction (expected to be near 43%). Besides axis inclination, misalignments of membrane yarns or unequal stretching of the yarns can occur. This will lead to slightly different yarn lengths along the membrane and thus to a small change in muscle length at different locations along a parallel. For these reasons, the muscle was always prestretched at a force of 70 kg before each test in order to fix the point of reference. At this load all yarns were aligned and taut.

5.3.2 Traction

Traction was measured in several runs at isobaric conditions. Gauge pressures were set at 10 kPa, 50 kPa, 100 kPa, 150 kPa, 200 kPa, 250 kPa and 300 kPa. For every run, readings of traction were taken every 0.5 mm for the first 10 mm of displacement, every 1.0 mm between 10 mm and 20 mm of displacement and every 2 mm thereafter. These were chosen in view of the gradients of force with regard to displacement. Traction was limited at 3.5 kN and, consequently, contractions of 5.0% for a gauge pressure of 300 kPa, 3.5% for 250 kPa, 1.5% for 200 kPa, 0.5% for 150 kPa and 0.0% for lower pressures were taken as a lower limit. The pressure was monitored during each run, but adjusting was never needed.

Fig. 5.5 plots the experimental mean values of traction at the various gauge pressure levels. Each run was repeated five times in view of the accuracy of the instrumentation. Scattering of about 5% of individual measured values from mean values were observed. Travel, which was predicted to be 43.5%, was experimentally found to be 41.5%. At this contraction, the equatorial section is not fully stretched or circular, indicating that further inflation is not hampered by lack of membrane circumference or shortage of folds. The deviation of 2% or 2 mm—similar values were found in all tested muscle models—is probably to be attributed to the pleating. An exact determination of the mechanism responsible for this is, however, not possible from the theory discussed in Chapter 3.

Fig. 5.6 shows the mean values of the measured dimensionless force function for each gauge pressure. The characteristic of f_t at a pressure of 10 kPa strongly departs from those at higher pressures. This divergence gradually decreases as the pressure increases. As from a gauge pressure of 150 kPa the characteristics practically coincide. The main reason for this seems to be the closed membrane's limited flexibility, which results from the pleating. A bare and unpleated piece of lined fabric is easily bendable. When it is pleated, however, it gains a structural stability and lateral supporting ability needing some work to be overcome. This can be visually observed: at low pressures the membrane yarns are clearly non-uniformly stressed, some regions even remain slack to some degree and this gives its surface a rough and dented appearance, at higher pressures, the membrane is more strongly forced outwards, which makes it taut at every point and gives it a smooth and very tense appearance. This means a threshold-like behavior is present in this type of PAM as well. The difference, however, between this threshold behavior and the one exhibited by the McKibben PAM is its limited action: it diminishes the developed force rather than prohibiting it from developing below the threshold pressure.

Fig. 5.7 plots the measured values of the dimensionless traction function f_t , averaged for all tests at pressure levels above 100 kPa. They are compared to the calculated values. The calculated values agree very well with the experimental values within a contraction range of 3% to 25%. At lower contractions, the membrane compliance lowers traction to finite values. At higher contractions

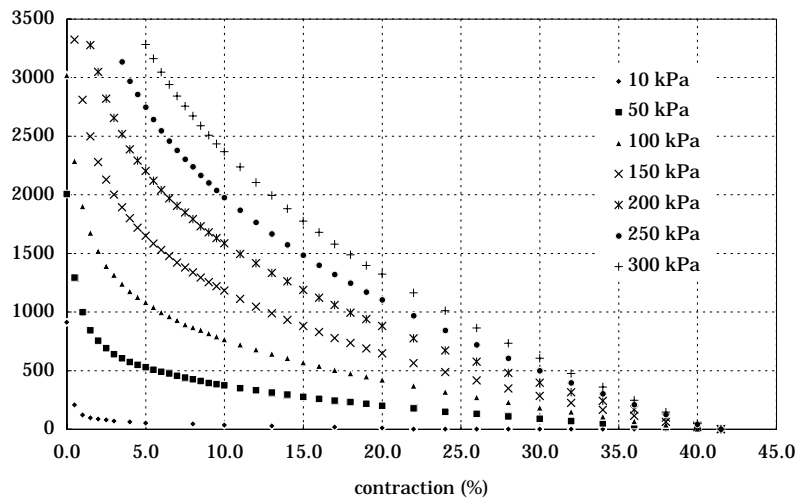
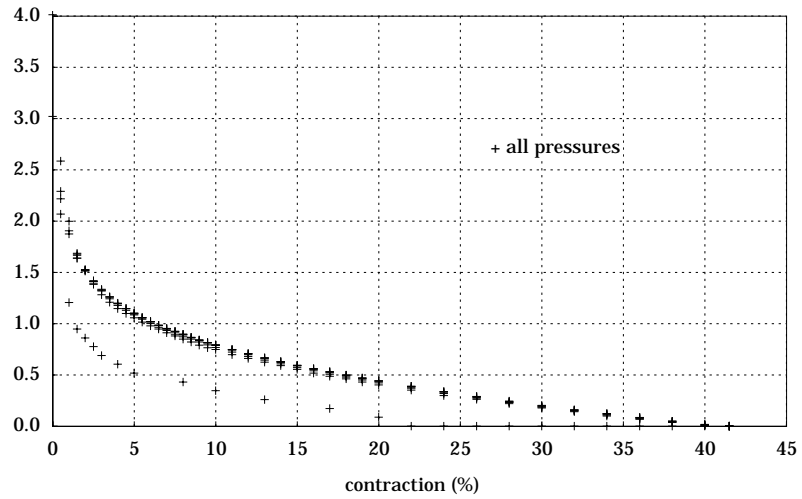
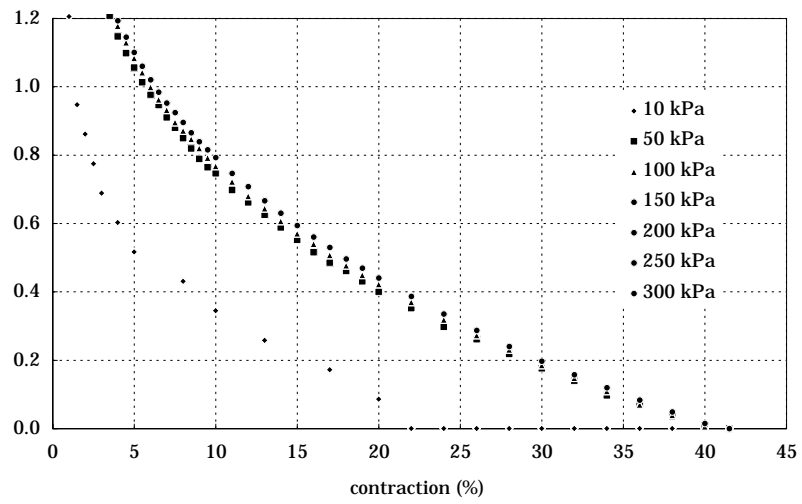


Figure 5.5: Prototype Pleated PAM measured traction F_t (N).

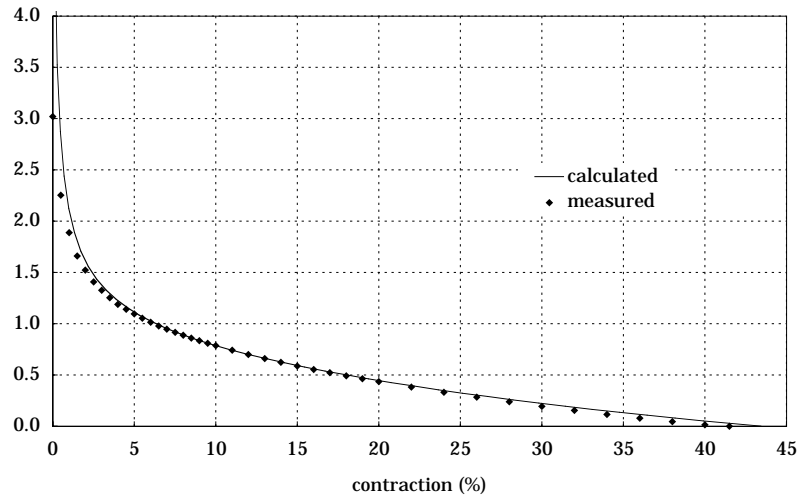


(a)

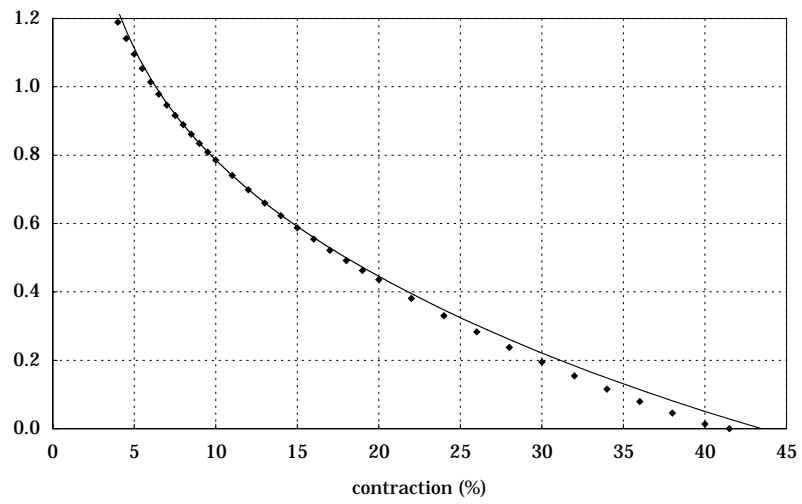


(b)

Figure 5.6: Prototype Pleated PAM measured dimensionless traction f_t , averaged values at various gauge pressures.



(a)



(b)

Figure 5.7: Prototype Pleated PAM averaged measured dimensionless traction f_t , compared to calculated values.

the value of traction drops to zero at a slightly steeper pace than predicted by the inelastic model. As explained above, this is probably due to the finite value of pleat depth.

5.3.3 Diameter

Together with traction, the value of the equatorial or maximum muscle diameter was measured. This was not done at 10 kPa gauge pressure because at that low a pressure the muscle is generally too slack and non-uniformly bulged along a parallel to identify the location of the maximum diameter. The results of these measurements are diagrammed in Fig. 5.8 as the values of the dimensionless diameter function d . Together with these, the calculated values are plotted. Only the mean values of maximum diameter at a gauge pressure of 50 kPa and of 300 kPa are shown because the change in diameter is too small to be discernible on this scale. The coincidence of calculated and measured values is very good.

Fig. 5.9 shows the ratios of the measured diameter to the calculated. On this scale the effect of pressure and the deviation from the calculated values can be checked more easily. At low contractions the effect of membrane compliance is clear at all pressures. At zero contraction the diameter at a gauge pressure of 50 kPa is 3.1 cm and at 100 kPa it is 3.95 cm. The influence of pressure

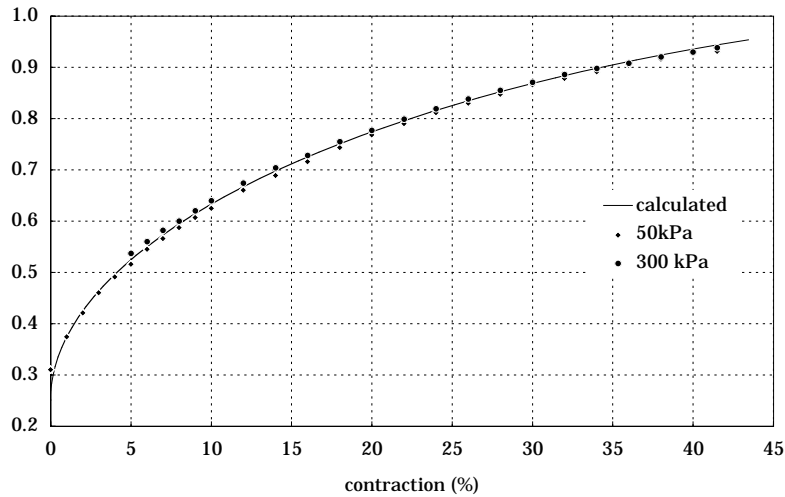


Figure 5.8: Measured dimensionless diameter function d compared to calculated values.

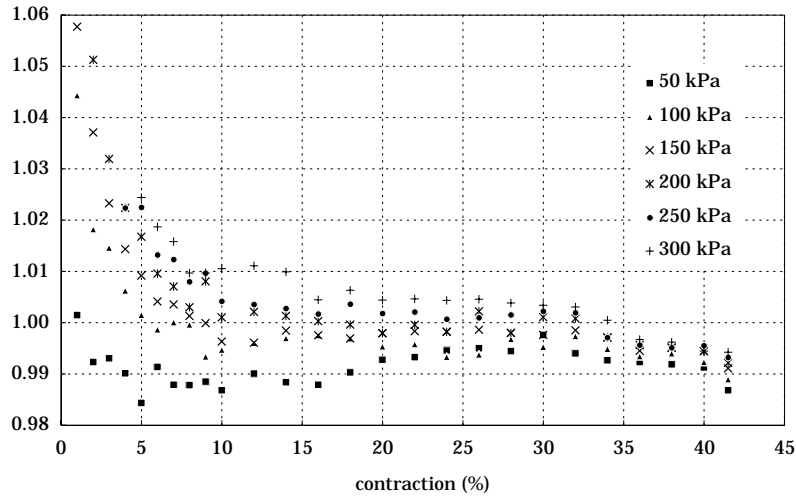


Figure 5.9: Ratio of measured diameter to calculated.

on diameter is much lower at high contractions: above 35% contraction, the difference in diameter between the lowest and the highest pressure cases is only 0.3–0.4 mm. As from a contraction of 30% the maximum diameter drops to lower values than predicted. Although this is a minor effect it is consistent for all tests and can be related to the drop in traction at these contractions.

5.3.4 Concluding Remarks

Overall, one can conclude from these tests that the theoretical inelastic model, which was derived in Chapter 3, can effectively be used to describe the Pleated PAM characteristics. The approximation of the zero parallel stress condition by using the pleated structure is proved to be satisfying. Slight deviations do occur at extreme conditions, i.e. small and high contractions and low pressures, but these are not of great practical importance in normal operating conditions.

5.4 Summary

A full prototype Pleated PAM design was presented in this chapter. The prototype has an initial length of 10 cm and initial diameter of 2.5 cm. The membrane has 44 folds, each 7 mm wide, and is made of a Kevlar fabric having 9 yarns per cm in the meridional direction. The stressed membrane section thus

equals 30.2 mm^2 and membrane thickness 0.28 mm . The end fitting sizes were chosen in order not to exceed allowable stresses—mainly epoxy resin stresses, fiber-epoxy shear stress and end fitting plug stresses. The prototype's weight was found to be only 58 g if aluminum is used as end fitting material and 116 g if copper is used.

Prototype muscle characteristics—travel, traction and equatorial diameter—were derived from the inelastic zero parallel stress approximation and experimentally checked. This prototype Pleated PAM is capable of developing pulling forces of nearly 3500 N at an operating gauge pressure of 300 kPa . The agreement between the model predicted values and the experimentally determined values is very good. The deviations were only noticeable at contractions of less than 3% , due to membrane compliance, and above 25% , probably due to the finite fold depth. The deviation at high contractions is only slight, but results in a travel of 41.5% whereas a value of 43.5% was predicted. The merit of the mathematical model was thereby confirmed.

The Pleated PAM was thus found to be a reliable actuation device with a good degree of repeatability and predictability.

Chapter 6

Antagonistic Rotative Actuator

6.1 Brief Description

In order to generate two-way motion using Pleated PAMs, at least two need to be set up antagonistically, as was explained in Chapter 2. The motion can be linear or rotative. Powering a revolute joint seems the most straightforward and natural use of PAMs. Their linear displacement is only moderate relative to their force and, therefore, some kind of transformation that increases the range of motion and decreases the force to more moderate levels will often be necessary. This is easier done in case of rotative motion of a revolute joint, using a direct transmission, than in case of linear motion. Hence, the actuation of a revolute joint was studied.

The actuation consists of three distinctive elements: the muscles, the linkage mechanism and the muscle controlling elements. The PAMs and the linkage mechanism determine the static characteristics of the joint. A rod transmission was chosen because of its ease of muscle connection and inherent asymmetrical operation about its central position. The muscle controlling elements regulate the gauge pressure of each muscle: as was seen in §2.3.2, the individual values of muscle gauge pressure determine the position and the compliance of the antagonistic actuator. Pressure regulating servo-valves, an angular position sensor and a software implemented control algorithm were used to this end. Each valve has a built-in pressure sensor and control electronics to set the pressure at the desired value. Its gauge pressure output is directly proportional to the command input voltage. This is calculated by the control software from the desired values of position and mean muscle gauge pressure and the value of angular position, which is measured by a precision potentiometer. Pressure feedback is not used by the control software since it is already used by the electronic feedback control system of the valves.

6.2 Linkage Mechanism

The simplest way of coupling the muscles to the links is by using a tendon-like system. Typical transmission problems like backlash can then be avoided. The tendons can either be flexible or rigid, depending on the type of drive. Basically, there are two types of tendon drives: a pulley drive and a lever drive. Various configurations or combinations of both can be designed.

The pulley mechanism was rejected for two reasons. Firstly, a pulley's lever arm has a constant length, whatever the angular position. The Pleated PAM is characterized by a non-linear force-contraction relationship, exhibiting very low values of force at one end of the contraction scale and very high at the other. At a fixed lever arm, this would imply that pressure ratios will have to be very high to reach the outer regions of angular displacement. With a maximum allowable gauge pressure of 300 kPa, the pressure to be set and maintained on the low pressure side will risk to drop to values too low to be set accurately and reliably. A lever drive, on the contrary, has a varying lever arm and an asymmetric operation and can be designed in such a way that the lever arm length increases for the contracting muscle and decreases for the elongating muscle.

Secondly, technological problems would arise when using a pulley drive because it requires the use of flexible tendons. These have to be easily connected to the muscle and flexible enough to bend smoothly about the pulley wheel. Because of the strong muscle forces and the periodical bending and stretching, the tendons are intensely loaded and need to have a big cross-section. For this type of loading flat tendons are preferable, but these are not easily fixed to the muscle. Furthermore, using a continuous belt or chain drive would induce backlash and possibly slip, so each muscle's tendon has to be fixed individually to the wheel at some point if these effects are to be avoided. In addition to these, a flexible tendon will cause an extra series elasticity to enter the actuator's behavior.

A lever arm mechanism was thus chosen as a power conveying system. Rigid pull rods were chosen as tendons because of their ease of connecting: they can be screwed to the muscle end fittings on one side and to the lever mechanism on the other. Securing flexible tendons, on the other hand, would need them to be glued or clamped, which makes for a much more delicate fastening. Each pull rod adds extra weight to the actuator, but this can be limited to acceptably low levels.

The drive is shown in Fig. 6.1 at its neutral or central position and at a clockwise rotation of 30° . As the link rotates about its pivot, the values of lever arm lengths, r_1 and r_2 , change, as can be seen from the figure. The kinematic characteristics of the joint can be influenced by adjusting the pivot eccentricity,

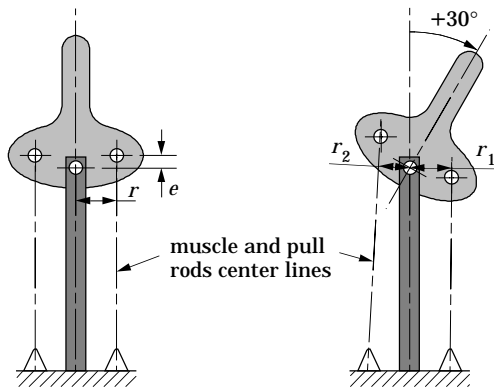


Figure 6.1: Lever drive.

which is notated as e .

The complete set-up of two links and two muscles is outlined in Fig. 6.2. It shows a side view of the set-up and three detailed views of the muscles and joint at the extreme and central positions. The static behavior of the revolute joint is determined by the values of the neutral lever arm r , the eccentricity e , the foot eccentricity r_f , which is the distance of the foot connection to the central line of the first link, the first link's compressed length L , which is the length of the part of the link situated between the joint and the muscles' foot connections and thus compressed by the muscle tension, the total angular displacement and the muscles' contractions at the central and extreme positions.

The prototype muscle's tension rises sharply at contractions below 5% and causes a risk of muscle overloading. At contractions beyond 35%, on the other hand, the tension drops to very low levels. Consequently, the nominal travel

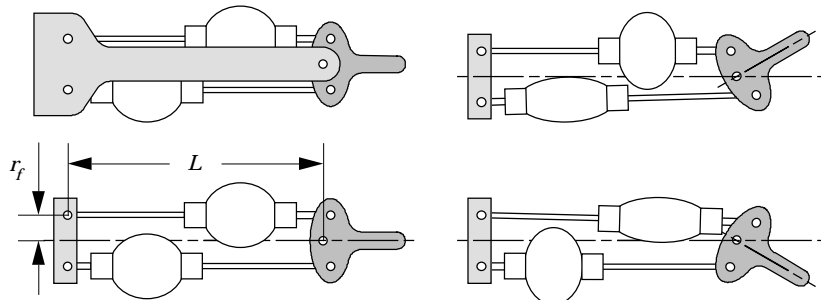


Figure 6.2: Antagonistic set-up.

of the muscles in the rotative actuator was limited between 5% and 35% contraction, or a length of 30 mm. At these values of contraction, the muscles' equatorial diameters are 54 mm and 90 mm, respectively (cf. Fig. 6.4(h)). This imposes constraints of space on the construction, since the muscles must not touch each other during operation. If the muscles are positioned wider apart the neutral lever arm will increase and the angular travel will decrease accordingly. This can be countered by connecting two PAMs in series at either side of the joint. Leaving slenderness and total volume—which is a measure of the work transferred when covering the full motion range—unaltered these will each have a length of $1/\sqrt[3]{2} \approx 0.79$ times the single case length since volume was found to be proportional to the third power of length at equal slenderness. Force will drop to a fraction of $0.79^2 \approx 0.62$ of its initial values. Displacement, however, is proportional to the total length and therefore increases by approximately 58% and, thus, the lever arm and the muscle spacing can be increased by the same value.

An alternative way of avoiding contact while keeping the lever arm at sufficiently low values is shifting the muscles from each other in their longitudinal direction. That way, the contact that is to be avoided is the contact between the membrane of one muscle and a pull rod of another. Since the latter has a low and fixed value, this adds extra room for placing the muscles.

As can be seen from Fig. 6.2, this method was applied in the set-up. Angular travel was chosen at $0^\circ \pm 30^\circ$ and r and r_f at 30 mm. At these values the muscles would surely touch and, therefore, they were shifted with regard to one another. When one muscle is fully inflated it crosses the first link's center line by about 15 mm, which is little enough to avoid contact with the other's pull rod. The design of the first link has to reckon with the muscle swelling: its frame either has to be built surrounding the muscles or running between them, leaving the necessary protuberance space. The design used in this work is of the former kind, as can be seen from Fig. 6.2.

The lever drive eccentricity was set at $e = 9$ mm and the link's compressed length at $L = 300$ mm. At the center position, both muscles are equally inflated to a contraction of 19%. These values were chosen so as to have a coincidence of the desired angular actuator travel and linear muscle travel. Additionally, a linear torque to angle relationship and the lowering of the ratios of muscle torques at the extreme positions were aimed for, as will be explained in the next section.

In view of the high maximum tension forces and torques, the links need a structural strength that can withstand this loading. Care has to be taken mainly about buckling of the first link, which can occur because of the compressive loading caused by the muscles' tension. Bending moments are caused by the components of the loading and the muscle tensions perpendicular to the first

link's axis. These were found to lead to only weak total transverse link loading, never exceeding 200 N (with the second link loaded perpendicularly to its axis at a distance of 30 cm of the pivot). Bending moments at the foot of the first link, whose length is about 30 cm will thus not exceed 60 Nm. Buckling resistance will then be the most stringent demand on the structure. On either side of the muscles a rectangular aluminum bar of $40 \times 10 \text{ mm}^2$ cross-section and 300 mm loaded length makes up part of the frame. Both bars are laterally connected at the foot, the middle and the top to increase buckling stability.

The prototype Pleated PAMs that were used have gas conducting end fittings on one side, as shown in Fig. 4.5. One muscle has this side connected to the foot while the other has it connected to the joint. The reason for this is to keep these end fitting short in order not to complicate their machining.

Fig. 6.3 shows photographs of the antagonistic actuator. Side and top views at the central and one extreme position are displayed. The construction of the link, the connection of the muscles and the operation are discernible from these.

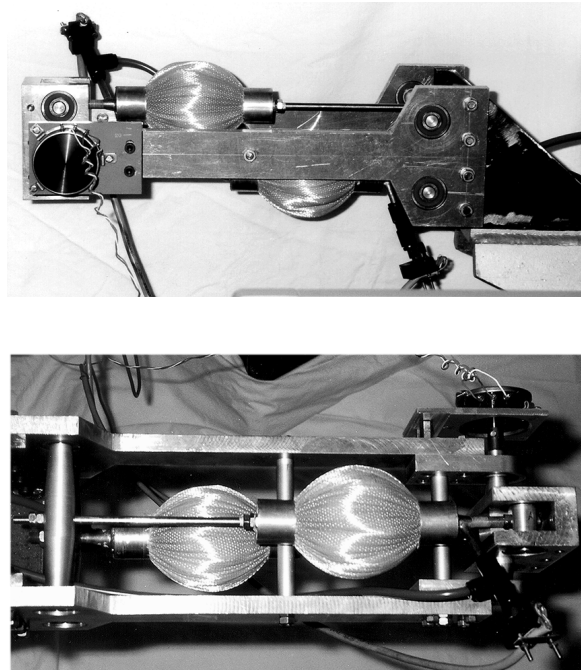


Figure 6.3: Rotative actuator photographic pictures.

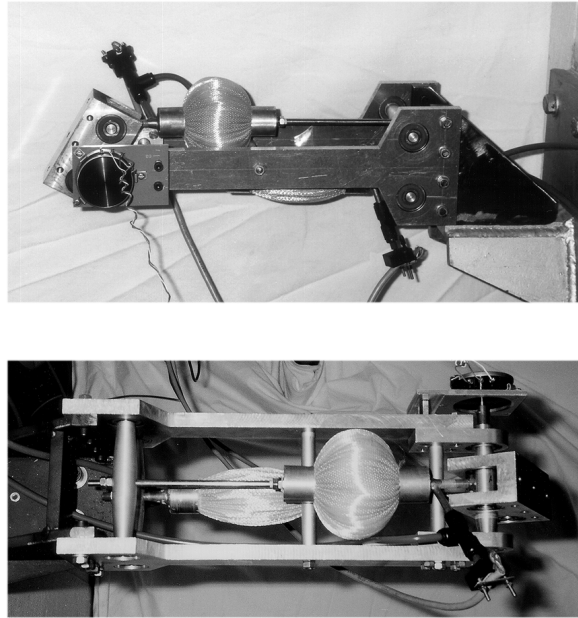


Figure 6.3: Rotative actuator photographic pictures. (cont.)

6.3 Static Actuator Characteristics

The values of joint geometry and muscle force to length relationship lead to the characteristics diagrammed in Fig. 6.4. It can be seen how the lever arm grows for the contracting muscle and shortens for the elongating muscle. As from an angle of about 10° the leverage remains more or less constant for the shortening muscle. Increasing the lever eccentricity could further increase the lever arm, but at the same time this would lower the value of the other lever arm and, as a result, the developed torque of the long muscle would drop too strongly. The torques are diagrammed in a first instance as dimensionless functions m_i . These are related to the actual torques M_i as

$$M_{1(2)} = p_{1(2)} l^3 m_{1(2)} \quad (6.1)$$

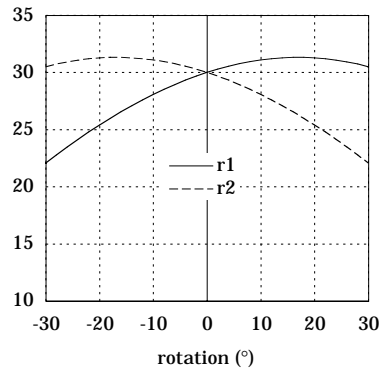
or to the dimensionless force functions as

$$m_{1(2)} = f_{t1(2)} \frac{r_{1(2)}}{l} \quad (6.2)$$

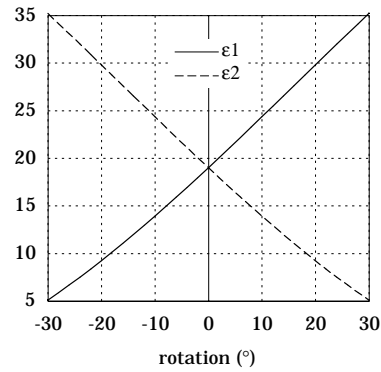
From a balance of work, in quasi-static conditions and assuming no energy losses to occur, these can be related to the dimensionless volume functions:

$$m_{1(2)} = \frac{dv_{1(2)}}{d\alpha} \quad (6.3)$$

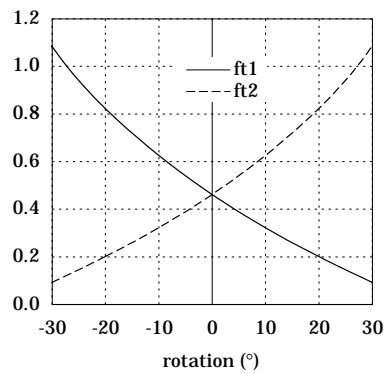
A quasi linear torque to angle relationship can be clearly seen from Fig. 6.4(d). This will simplify control, as will be seen later; if the sum of both muscle



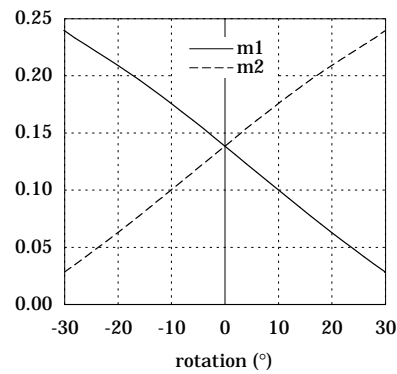
(a) Lever arms (mm).



(b) Contractions (%).

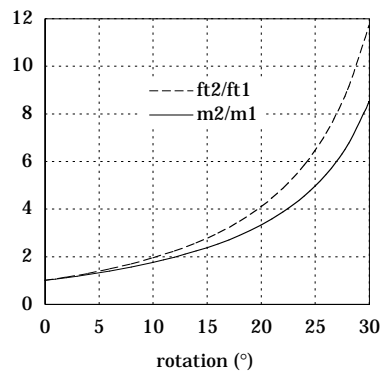


(c) Force functions ().

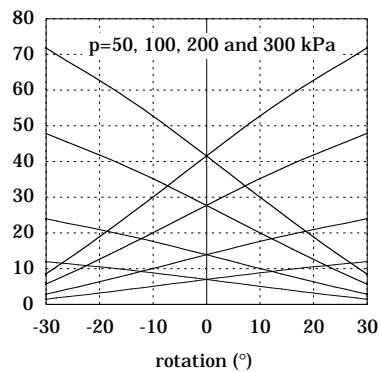


(d) Torque functions ().

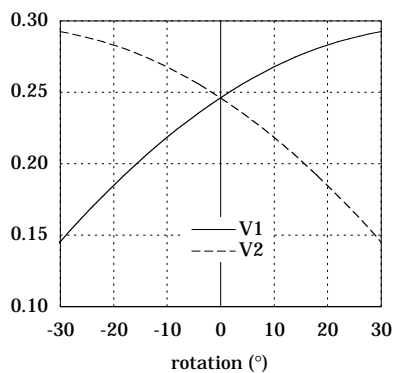
Figure 6.4: Rotative actuator static characteristics.



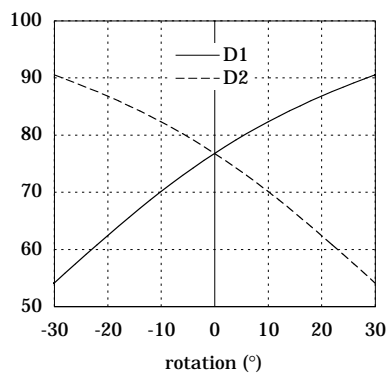
(e) Force and moment ratios.



(f) Torques at various pressures (Nm).



(g) Volumes (l).



(h) Equatorial diameters (mm).

Figure 6.4: Rotative actuator static characteristics. (cont.)

pressures is kept at a constant level, the position, in the absence of external and inertial loads, will be directly proportional to the difference of both pressures. In a linear approximation the torque functions can be written as:

$$m_1 = m_0 - k\alpha \quad m_2 = m_0 + k\alpha \quad (6.4)$$

with α the angle of rotation (positive in the clockwise direction). Expressing

torque equilibrium $M_1 = M_2$, consequently leads to

$$\alpha = \frac{m_0}{k} \frac{p_1 - p_2}{p_1 + p_2} \quad (6.5)$$

From a linear regression the values of m_0 and k were found to be 0.138 and 0.207 rad⁻¹, respectively, for the prototype muscles and the proposed geometry.

Fig. 6.4(e) shows the ratio of dimensionless force functions and torque functions as a function of the angular displacement. This ratio determines the position in the absence of load:

$$M_1 = M_2 \Rightarrow \frac{m_1}{m_2} = \frac{p_2}{p_1} \quad (6.6)$$

Whereas a pulley drive would have the maximum of this ratio (displacement of 30°) at a value of about 12, the lever drive has it at about 8.5. Lowering this ratio increases the range of operation because the setting of stable low gauge pressures will be increasingly difficult and critical as they drop to values below ≈ 5 kPa and maintaining an equilibrium position requiring such low pressures will hence be equally difficult. On the other hand, the overall values of this ratio must not drop too far as this will increase the actuator's sensitivity to pressure change, as can be seen from the diagram.

Fig. 6.4(f) plots the actual values of torques at various gauge pressures. At the central position, the maximum torque developed by an individual muscle is about 40 Nm at a gauge pressure of 300 kPa. The absolute maximum torque is over 70 Nm and is developed by the long muscle in either of the extreme positions. This torque cannot be balanced by the short muscle due to the imposed pressure limitation and will hence only occur to generate a position restoring acceleration or to keep an external load at an equilibrium position.

Fig. 6.4(g) shows the values of the muscle volume as calculated by the inelastic zero parallel stress condition, presented in §3.4. It can be seen that the individual muscle volumes range from about 0.151 to 0.31.

Fig. 6.4(h), finally, plots the values of the maximum muscle diameter as measured for a gauge pressure of 300 kPa (cf. §5.3.3). At their narrowest, the muscles have a diameter of 54 mm and at their highest contraction they will have swollen to 90 mm.

Joint rotation is accompanied by small rocking movements of the muscle axes as can be seen from Figs. 6.1 and 6.2. Although for the chosen dimensions their range is small, from -0.25° to 1.51° , they do impose that the muscles be hinged at their feet. Some kind of bearing is required to this end.

Static tests were carried out measuring the value of the angle and the gauge pressures of both muscles. The angle was measured by a potentiometer, Sakae

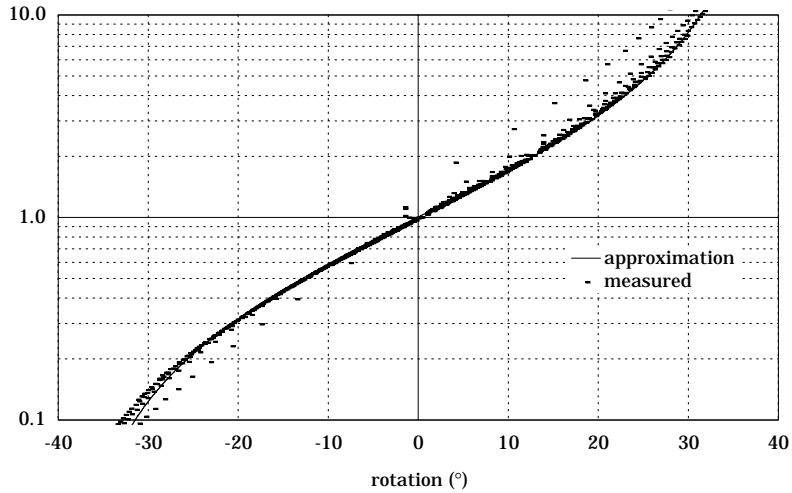
type FCP50A, and the gauge pressures by the silicon sensors Data Instruments XCA5-60GN. Appendix C lists the technical specifications of both devices. Gauge pressures were set at values ranging from 10 kPa to 300 kPa in discrete steps of 10 kPa. All possible combinations of gauge pressures were set.

Fig. 6.5(a) plots the values of measured gauge pressure ratios as a function of angular displacement. The measured values are compared to the approximations according to Eq. 6.4:

$$\frac{p_1}{p_2} = \frac{m_2}{m_1} \approx \frac{0.138 + 0.0036\alpha}{0.138 - 0.0036\alpha} \quad (6.7)$$

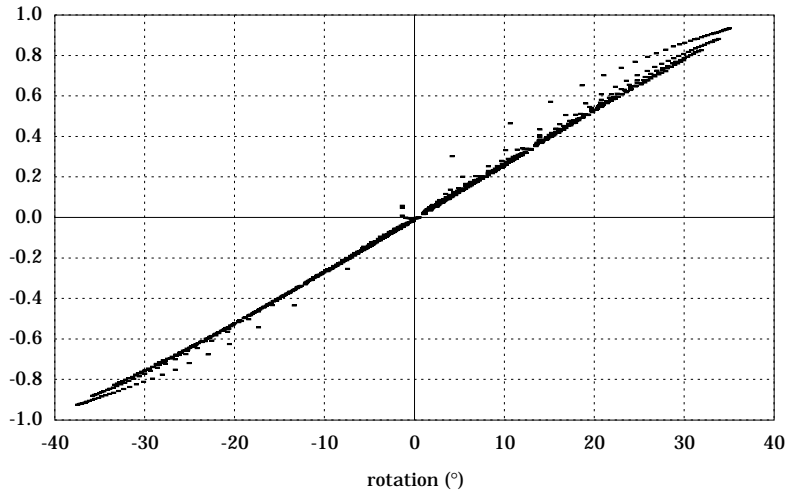
Fig. 6.5(b) plots the values of the ratio of the difference of the measured gauge pressures to their sum as a function of angular displacement. This representation evaluates the approximation made by Eq. 6.5. The points that deviate markedly from the general trend are those which have a low value of pressure in either muscle. This could be expected from the discussion in §5.3.2. Performing a linear regression on the measured values leads to a ratio of $m_0/k = 37.9^\circ$ whereas a value of 38.3° was predicted.

A slight asymmetry of behavior about the central position occurs. This is due to the fact that the muscles are not perfectly equal. This was already explained



(a) Gauge pressure ratios.

Figure 6.5: Measured static pressure to angle relations.



(b) Ratio of gauge pressure difference to sum.

Figure 6.5: Measured static pressure to angle relations. (cont.)

in §5.3.1 as resulting from small misalignments during assembly. Setting both muscles at a contraction of exactly 19% is therefore impossible. The effect is very small, however, and will hardly be of any importance.

6.4 Valves

6.4.1 General

The use of valves is inherent to all fluid actuators. They distribute the fluid power by controlling the flow of pressurized fluid to the actuator fluid chambers. In this case, the gas flow to either muscle needs to be controlled in order to set the gauge pressures at the desired values. Not taking into account power limiting phenomena affecting the actuator, e.g. pneumatic cylinder push rod buckling due to overload, the valves' maximum flow and outlet gauge pressure determine the maximum power conveyed by the actuator.

Controlling pressure implies controlling the gas flow in such a way that the gauge pressure level reaches the set value. This can be done by proportionally operated valves or on-off operated valves. The latter method uses fast switch-

ing valves that are driven by either pulse width or frequency modulated signals. Pneumatic valve switching times are typically in the range of 10–30 ms, depending on the valve actuation system and on the valve nominal flow (Lü, 1992). Faster switching times, 5 ms and less, can be reached by using low mass valve plungers or by using pneumatically instead of electrically actuated plungers. Matrix S.p.A., Italy, manufactures solenoid actuated valves that have an extremely low switching time of 1 ms and can be operated at switching frequencies of several hundred Hz.

Proportionally operated valves have an orifice section that is continually adjusted through an electronic control circuit. This uses feedback of the variable that needs to be set and which, in case of an antagonistic PAM actuator, is the gauge pressure. In an antagonistic or two-way cylinder positioning system, on the other hand, servo-valves use the value of position as feedback signal. Fast acting pressure proportional valves have a delay time of about 5 ms to 10 ms. Their dynamic behavior depends mainly on their flow section relative to the volume on which they act and on the dynamic behavior of the plunger and its actuation.

The valves' nominal flow has to be sufficiently high in order to get fast actuator response times. As the nominal flow increases, however, the valve weight and power consumption will augment accordingly: the plunger will enlarge because of the wider flow sections and this will necessitate a more powerful and, hence, heavier valve actuation, which, in turn, will increase the valve casing size and weight. A second detrimental effect occurring at an elevated flow is enhanced valve nervousness. The reason for this is the reduced volume with regard to orifice section, which makes an equal action of the valve controller and plunger lead to stronger pressure changes.

Valve flow can be characterized in several ways. One is using the flow coefficients b (dimensionless) and C (usually given in Std.l/minbar) at full orifice opening. The flow path through a valve can be modelled as a series of orifices (Schwenzer, 1983). Assuming frictionless and adiabatic flow of dry air as an ideal gas, each orifice flow is characterized by (Ezekiel and Shearer, 1960)

$$\dot{m} = \begin{cases} AP_u \sqrt{\frac{2}{rT_u}} \sqrt{\frac{\gamma}{\gamma-1} \left(\left(\frac{P_d}{P_u} \right)^{2/\gamma} - \left(\frac{P_d}{P_u} \right)^{(\gamma+1)/\gamma} \right)} & \text{if } \frac{P_d}{P_u} \geq 0.528 \\ 0.484 AP_u \sqrt{\frac{2}{rT_u}} & \text{if } \frac{P_d}{P_u} \leq 0.528 \end{cases} \quad (6.8)$$

with $P_d/P_u = 0.528$ the critical pressure ratio, A the orifice flow section area, r the gas constant for dry air, γ the isentropic coefficient and the indices u and d

referring to upstream and downstream, respectively. At subcritical conditions the orifice is said to be choked: downstream conditions will not affect the flow or the pressure in the vena contracta. A series of orifices will bring down the value of the overall critical pressure ratio to a value, notated as b , smaller than 0.528. For these real conditions a normalized approximation of flow is given by ISO 6358 and CETOP RP 50P:

$$\dot{m} = \begin{cases} CP_u \rho_0 \sqrt{\frac{293}{T_u}} \sqrt{1 - \left(\frac{P_d/P_u - b}{1 - b}\right)^2} & \text{if } \frac{P_d}{P_u} \geq b \\ CP_u \rho_0 \sqrt{\frac{293}{T_u}} & \text{if } \frac{P_d}{P_u} \leq b \end{cases}$$

$$= CP_u \rho_0 \sqrt{\frac{293}{T_u}} \Psi(P_d, P_u, b) \quad (6.9)$$

with ρ_0 the air density at standard conditions (20° C and 100 kPa). This expression will yield the value of mass flow at full orifice opening, if the valve is only partly opened, it has to be multiplied by the fraction of opening.

Another way of valve flow characterization frequently used by manufacturers is determining the flow at two conditions, namely at a pressure drop of 700 kPa to 600 kPa (absolute) and at a pressure drop of 700 kPa to 100 kPa (absolute). From these two values the flow coefficients can be calculated in order to predict valve flow at any condition.

Off-the-shelf pressure regulating valves include both proportional and pulse width modulated systems. The following have been considered:

- Tecno proportional valve, manufactured by Hoerbiger-Origa, GmbH, Germany;
- KPS 3/4 proportional valve, manufactured by Kolvenbach KG, Germany;
- EPR 100, pulse width modulated valve, manufactured by Matrix S.p.A., Italy;

They represent the main pressure regulating valve categories with regard to plunger actuating principle (electropneumatic and electromagnetic) and to control type (continuous and discontinuous). Their technical specifications and characteristics are listed in Appendix C. The pulse width modulated system was rejected because of its low flow and hence fairly slow behavior: at a supply pressure $p_s = 800$ kPa and loaded by a volume of 0.031 a pressure rise time

(200 kPa to 400 kPa) of 60 ms and fall time (400 kPa to 200 kPa) of 100 ms is reported by the manufacturer. With the Pleated PAMS volumes ranging from 0.15 l to 0.3 l these valves will be inadequate. Both the Tecno valve and the KPS 3/4 were tried, as will be discussed in the next section.

6.4.2 Servo-Valves Characteristics

The main difference between the Tecno and the KPS 3/4 servo-valves is their actuation principle: the former is electropneumatically actuated, the latter electromagnetically. The Tecno valve has a two stage concept: its first stage is a miniature piezoceramic flapper-nozzle pneumatic valve that actuates the main stage plunger by way of a diaphragm. The restoring plunger movement is caused by spring action. Due to the piezoceramic action its reaction time is fast, 5 ms, and its electric power consumption is very low at only 0.25 W. The KPS 3/4 valve has a solenoid actuated plunger designed for dynamic performance, the bandwidth of its full range motion is reported to be 70 Hz and its switching time (0 . . . 100% opening) is 5 ms. Both valves have built-in feedback control electronics and a pressure sensor.

The Tecno valve flow constants are $C = 29.9 \text{ Std.l./min bar}$ and $b = 0.132$. At a pressure drop of 7 bar to 6 bar (absolute) the nominal flow is 115 Std.l./min. The KPS 3/4 valve's specified flow values are 300 Std.l./min at a pressure drop of 7 bar to 6 bar (absolute) and 550 Std.l./min at a pressure drop of 7 bar to 1 bar (absolute). From these the flow constants can be calculated: $C = 78.6 \text{ Std.l./min bar}$ and $b = 0.116$. The higher values of flow of this type of servo-valve with regard to the Tecno are reflected by their weights, 225 g for the Tecno and 1 kg for the KPS 3/4, and, together with the operating principles, by their electric power supply, (nominally) 0.25 W for the Tecno and (maximally) $\approx 20 \text{ W}$ for the KPS 3/4.

In order to evaluate the dynamic behavior, the servo-valves were tested on a single muscle that was contracted by 35%. This was chosen because at a rotation of $\pm 30^\circ$ the inflated muscle is 35% contracted and thus at a maximized volume, the value of which is 0.3 l. The muscle was clamped in a draw bench at the appropriate clamp distance. The initial muscle gauge pressures were set at values of 10 kPa, 50 kPa, 100 kPa, 150 kPa, 200 kPa, 250 kPa and 300 kPa, which was done by setting the servo-valve command input voltages at 0.1 V, 0.5 V, 1.0 V, 1.5 V, 2.0 V, 2.5 V and 3.0 V, respectively. Servo-valve input signal steps taking the command voltages to 0 V, 0.5 V, 1.0 V, 1.5 V, 2.0 V, 2.5 V and 3.0 V were subsequently imposed and the response, which is the muscle gauge pressure, was read at a sampling period of 10 ms. The pressure sensor was set in the tubing between muscle and valve. The length of the tubing was 10 cm and its internal diameter 4 mm. This way the tubing does not noticeably

influence the fluid flow. The setting and reading were done by a PEP Modular Computer VM30, using a VME bus onto which an eight channel analog to digital converter, PEP ADC3, and a four channel analog to digital converter, PEP DAC3, are connected. This system is managed by the OS/9 operating system, which allows sampling periods of any multiple of 10 ms for reading and setting.

Tecno Servo-Valve

Fig. 6.6 shows results of these tests for the Tecno servo-valve. The system comprised of the valve and muscle is clearly non-linear: the pressure rise and drop times depend on the amplitude of step change and on the value of initial gauge pressure. The diagram showing responses from a start gauge pressure of 10 kPa indicate a steep initial pressure rise, which rapidly slows down. With supply pressure P_s at 800 kPa, and muscle pressure between 100 kPa and 400 kPa, the valve is always choked or close to being so during pressure build-up and in a first approximation the valve mass flow can be regarded as being directly proportional to the orifice flow section (cf. Eq. 6.9). Assuming a polytropic change of state inside the muscle, as is described in Appendix B, the pressure change is proportional to mass flow:

$$dP = \frac{n}{V} r T_s dm \quad (6.10)$$

which follows from Eq. B.26, with T_s the compressed gas supply temperature and n the polytropic coefficient. Consequently, the pressure gradient is directly proportional to the orifice section and a direct indication of the valve servo-action.

During the first 20 ms the responses to step inputs of 10 kPa to 200 kPa, 250 kPa and 300 kPa coincide and their gradient is at about 30–35 kPa per 10 ms. Therefore, one can assume the valves to be fully opened at the onset of pressure regulation. After a few tens of ms, however, the controller starts adjusting the orifice section. At smaller step inputs the valve is never maximally opened, as is clear from the smaller gradients.

At low values of initial gauge pressure, the rise time for an equal pressure increase is apparently greater than at more elevated values, indicating a stronger valve actuation at higher levels of pressure. This can be seen by comparing the responses for the 10 kPa to 50 kPa step, the 100 kPa to 150 kPa step and the 200 kPa to 250 kPa step.

The valve shows a distinct asymmetry in behavior with regard to charging and discharging. The start of pressure decrease is much gentler and slower than that of build-up. This is a consequence of the asymmetrical valve actuation:

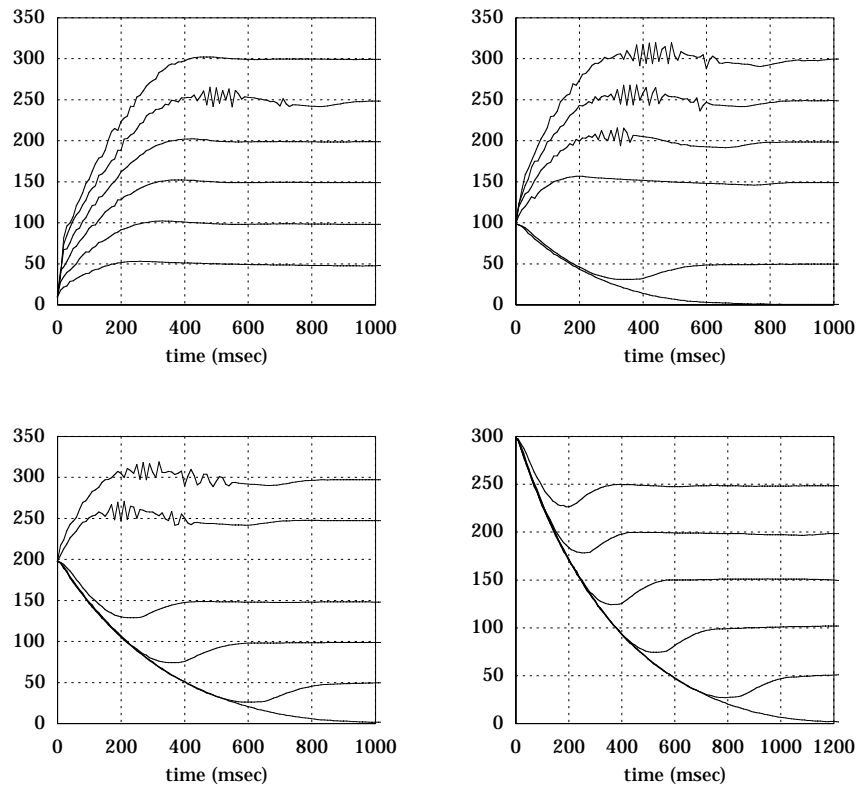


Figure 6.6: Pleated PAM, 35% contracted, gauge pressure (kPa) set by Tecno servo-valve, command step input response.

in order to pressurize its load volume the flapper-nozzle first stage valve will pneumatically move the plunger, to let off its load volume the first stage has to be let off itself which is a slower process since it will usually happen at unchoked conditions. After a few sample periods the gradient is at its maximum level, which is equal for all step inputs. Only for pressure drops ranging to about 50 kPa the orifice section is somewhat narrower. The slower pace of venting relative to inflating is caused by the lower upstream pressure and by the high valve pressure ratios, always superior to $100/400 (> b)$, during discharging, preventing at all times the valve from being choked. As the pressure drops, its gradient drops as well because of the drop in upstream pressure and the growing valve pressure ratio. The asymmetrical behavior is highlighted by the process time difference between a full inflation and a complete venting of the

muscle: 400 ms to 1200 ms.

The built-in pressure controller is sensitive to disturbances as can be concluded from the ripple occurring during the period of overshoot when pressurizing. This effect does not happen when letting off the muscle, although the signal overshoot in this case is much higher. Nervousness of the valve during the pressure rise or drop is not witnessed.

KPS 3/4 Servo-Valve

Fig. 6.7 plots readings of the same tests performed with the KPS3/4 valves. Compared to the previous valve type, its nervousness during charging is strik-

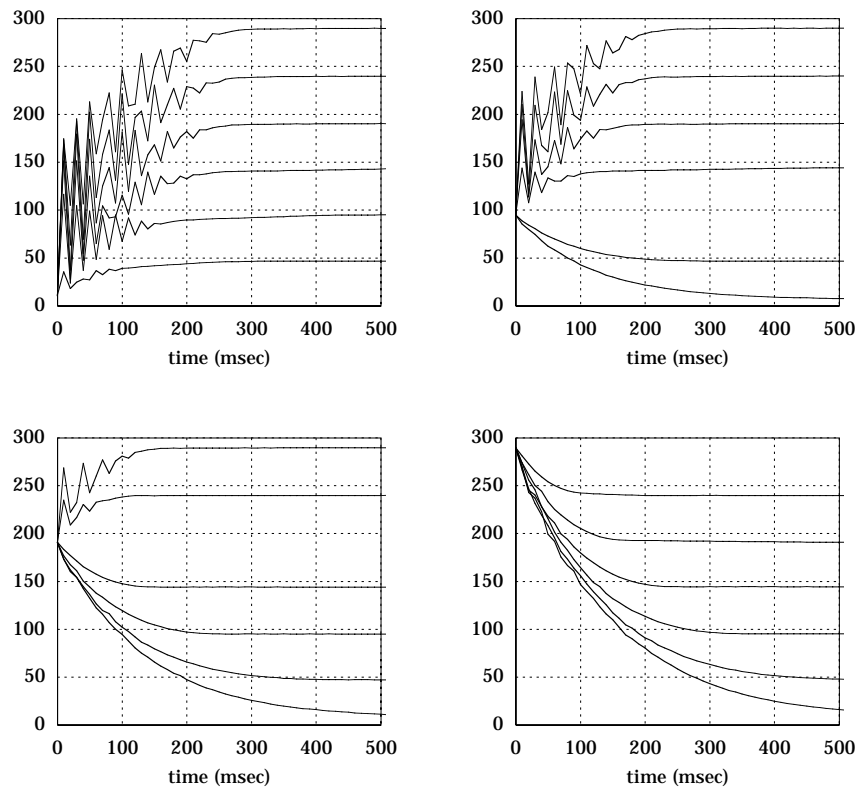


Figure 6.7: Pleated PAM, 35% contracted, gauge pressure (kPa) set by KPS 3/4 servo-valve, command step input response.

ing. Strong oscillations having frequencies ranging around 40 Hz to 50 Hz (or multiples of these since the sampling period is 10 ms) occur and this is also audible during the test as a pulsating sound. If these were to be caused by pressure waves traveling back and forth in the muscle and tubing their frequencies would have an order of magnitude equaling the ratio of the speed of sound to a typical value of length: $300 \text{ m/s} \div 25 \text{ cm} = 1.5 \text{ kHz}$. This was rejected as a possible cause of the oscillations because of the apparent consistency of the oscillations at varying values of step input and initial gauge pressure, because of the absence of this effect at discharging, because of the absence of the effect when using the Tecno valve, because of the accordance of the apparent frequencies with the manufacturers specifications (plunger motion bandwidth of 70 Hz) and because pressure waves of such high frequencies would not be

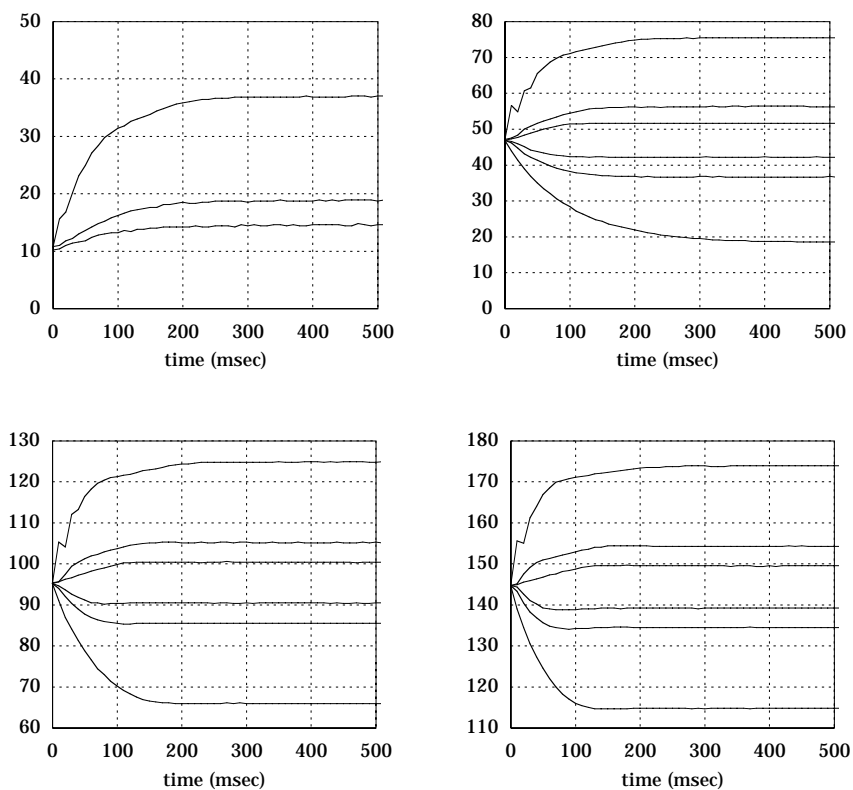


Figure 6.8: Pleated PAM, 35% contracted, gauge pressure (kPa) set by KPS 3/4 servo-valve, small command step input response.

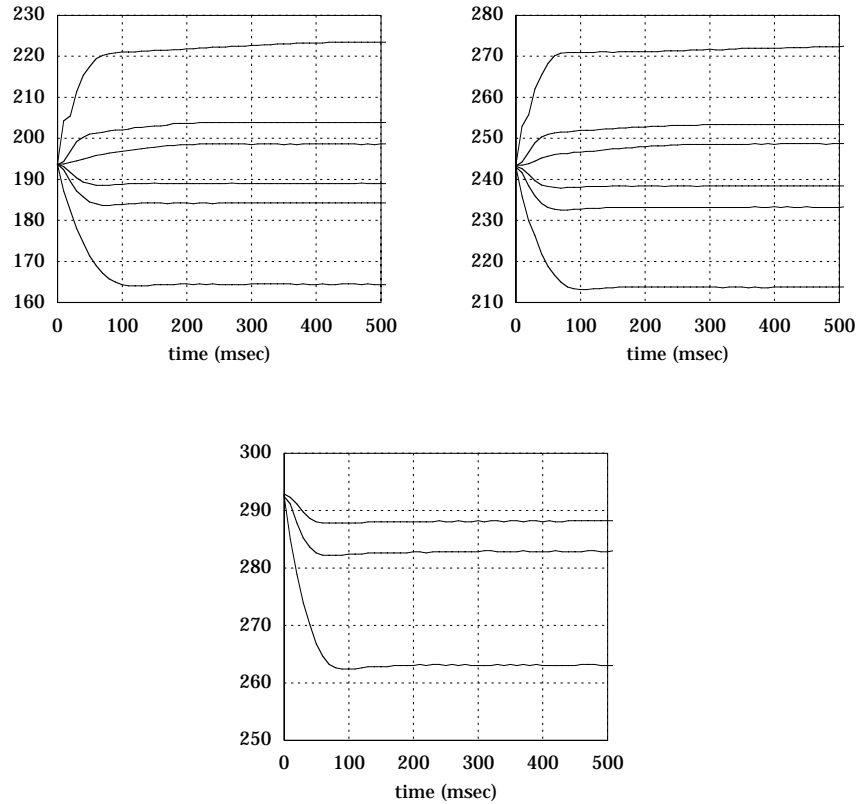


Figure 6.8: Pleated PAM, 35% contracted, gauge pressure (kPa) set by KPS3/4 servo-valve, small command step input response. (cont.)

audible as a pulsating but as a continuous sound.

An end error of 4% to 5% between the set value and measured value of gauge pressure is observed from the readings. This is not a very strong deviation, but, if necessary, it can be adjusted through the gain used in the software control.

The asymmetry with regard to filling and venting is less clear for these valves than for the Tecno valves. As the start pressure increases the valve reacts slightly faster to a similar input step change. There is no overshoot in either pressurization or decompressing, as opposed to the Tecno valve responses. Besides this, a stable output is faster reached and disturbance sensitivity is not apparent from the diagrams. It is also clear from these diagrams that the valve

actuation operates also during discharging as can be seen from the small oscillations and from the difference in pressure gradient for varying step input signals, which the Tecno valve showed only for pressure drops inferior to 50 kPa.

Overall, one can say that the KPS3/4 valve operates at a speed nearly the double of the Tecno valve's for charging and, taking into account overshoot, approximately triple for discharging.

Fig. 6.8 shows the responses to small steps of the command signal (0.05 V, 0.1 V and 0.3 V). These are somewhat faster for these low variations except for the increase of 0.05 V, to which the valve reacts consistently slower as from a gauge pressure of 100 kPa. A possible reason for this behavior is plunger friction becoming more important at small pressure changes, as its required displacement becomes increasingly smaller. To let of 5 kPa, the plunger displacement needs to be greater than to charge by an equal amount, because of the absence of choking, which could explain why this phenomenon does not occur at discharging. It is also clear how the pressure step settling time drops for an increasing value of gauge pressure.

Fig. 6.9 shows some results of the same tests performed at a muscle contraction of 5%, occurring at the other end of the rotative actuator displacement range. At this point the muscle volume is 0.151, which is halve of its maximum value and this is clearly reflected by a halving of settling times.

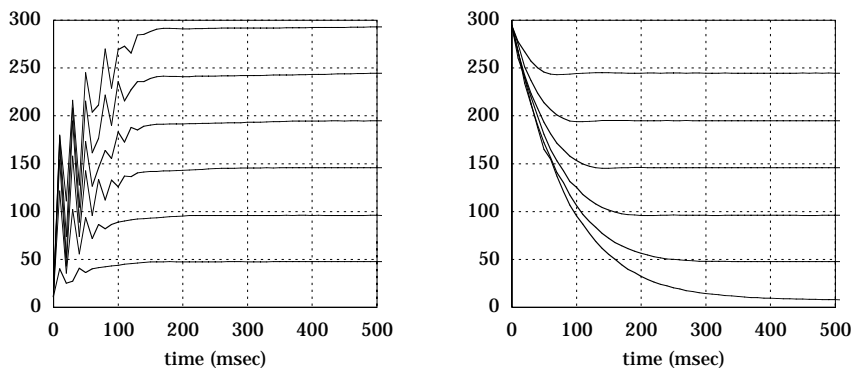


Figure 6.9: Pleated PAM, 5% contracted, gauge pressure (kPa) set by KPS 3/4 servo-valve, command step input response.

Concluding Remarks

The tests discussed above give a general idea about the dynamic pressure regulating behavior of the servo-valves in combination with one Pleated PAM at a fixed contraction and volume. In the set-up of the antagonistic actuator, however, the contractions and volumes of both muscles are not fixed and this will affect that dynamic behavior. Generating a small actuator displacement at a fixed sum of the individual values of muscle gauge pressures can be done by increasing the shortening muscle pressure by an amount Δp and decreasing the lengthening muscle pressure by the same amount, as can be seen from Eq. 6.5. Under polytropic and ideal gas assumption, the required change of muscle air mass contents can be derived from Eq. B.26, and will be

$$\Delta m_1 = \frac{1}{nrT_s} (V_1 \Delta P + P_1 \Delta V_1) \quad (6.11)$$

for the contracting muscle, and

$$\Delta m_2 = -\frac{1}{nrT_2} (V_2 \Delta P + P_2 \Delta V_2) \quad (6.12)$$

for the elongating muscle. This shows that the flow will be larger if not only pressure but also volume changes.

From the characteristics presented in this section one can also predict a varying behavior of the actuator with regard to rotation, as will be confirmed in the next chapter: if the actuator is nearing either extreme of its displacement range, it will tend to slow down. Moving towards an extreme, the shortening muscle will be the powering muscle and is therefore charged. As its volume increases, the valve-muscle combination operates slower, as was clear from comparing Fig. 6.7 to Fig. 6.9. The elongating muscle has to be discharged and, although its volume decreases, which would increase speed, its gauge pressure has to drop reasonably strong (cf. Fig. 6.4(e)) and the characteristics presented in this section show that this process is increasingly slower as the pressure level lowers.

From the dynamic point of view, especially settling speed, overshoot and disturbance sensitivity, the KPS 3/4 valves outperform the Tecno valves. Depending on the application their weight can be a problem. This can be improved because of their modular concept. The core elements—plunger, solenoid and pressure sensor—can be isolated from the rest of the valve, bringing the weight down to about 300 g, and the electronic control components can be delocalized from the actuator.

6.5 Compliance/Stiffness

Actuator compliance or, inversely, stiffness can be deduced from the values of torques exerted by the muscles on the joint:

$$\begin{aligned} K = C^{-1} &= -\frac{dM_1}{d\alpha} + \frac{dM_2}{d\alpha} \\ &= l^3 \left(-\frac{dp_1}{d\alpha} m_1 - p_1 \frac{dm_1}{d\alpha} + \frac{dp_2}{d\alpha} m_2 + p_2 \frac{dm_2}{d\alpha} \right) \end{aligned} \quad (6.13)$$

with the dimensionless torque functions as defined by Eq. 6.1. What its value will be depends not only on the static characteristics shown in Fig. 6.4 but also on the dynamic behavior of the servo-valve/muscle combinations and on the thermodynamic processes taking place in the system. The membrane's elasticity, however, is of no influence because of its very high tensile stiffness. Part of the actuator stiffness is caused by the change in pressure accompanying rotational excursions and this will be mainly influenced by the servo-valve action and the change in volume, as can be seen from applying the first law of thermodynamics, cf. Eq. B.26:

$$\frac{dp_{1(2)}}{d\alpha} = \frac{n}{V_{1(2)}} \left(rT_s \frac{dm_{1(2)i}}{d\alpha} - rT_{1(2)} \frac{dm_{1(2)e}}{d\alpha} - P_{1(2)} \frac{dV_{1(2)}}{d\alpha} \right) \quad (6.14)$$

with $dm_{1(2)i}/d\alpha$ and $dm_{1(2)e}/d\alpha$ standing for the incoming and exiting mass flows, respectively. Another contributing part to stiffness is inherent to PAMS and is caused by their changing effective area, which leads to a torque varying with rotation at isobaric conditions.

In case of closed pressurized muscles and polytropic changes of state, the pressure change terms can be elaborated using Eq. 2.3 and the definitions of the dimensionless functions of force and volume (Eqs. 3.43 and 3.44) to

$$\begin{aligned} \frac{dp_{1(2)}}{d\alpha} &= \frac{dp_{1(2)}}{dV_{1(2)}} \frac{dV_{1(2)}}{dl_{1(2)}} \frac{dl_{1(2)}}{d\alpha} \\ &= -n \left(\frac{P_{1(2)}}{V_{1(2)}} \right) \left(-\frac{F_{1(2)}}{p_{1(2)}} \right) \left(-l \frac{d\epsilon_{1(2)}}{d\alpha} \right) \\ &= -nP_{1(2)} \frac{f_{t1(2)}}{v_{1(2)}} \frac{d\epsilon_{1(2)}}{d\alpha} \end{aligned} \quad (6.15)$$

which leads to

$$\begin{aligned} \frac{K}{l^3} &= nP_1 \frac{f_{t1}}{v_1} \frac{d\epsilon_1}{d\alpha} m_1 - p_1 \frac{dm_1}{d\alpha} - nP_2 \frac{f_{t2}}{v_2} \frac{d\epsilon_2}{d\alpha} m_2 + p_2 \frac{dm_2}{d\alpha} \\ &= nP_1 k_{p1} + p_1 k_{m1} + nP_2 k_{p2} + p_2 k_{m2} \end{aligned} \quad (6.16)$$

Notating

$$K_p = nl^3(P_1k_{p1} + P_2k_{p2}) \quad K_m = l^3(p_1k_{m1} + p_2k_{m2}) \quad (6.17)$$

one can write

$$K = K_p + K_m \quad (6.18)$$

The values of stiffness factors $k_{p1(2)}$ and $k_{m1(2)}$, which are dimensionless, depend only on the angle and can therefore be calculated from the static characteristics. The stiffness factors of either muscle compare as

$$k_{p1}(\alpha) = k_{p2}(-\alpha) \quad k_{m1}(\alpha) = k_{m2}(-\alpha) \quad (6.19)$$

The stiffness factors of one muscle and the overall actuator stiffness values are plotted in the diagrams of Fig. 6.10. The strong variation of $k_{p1(2)}$ is not only due to the decreasing volume, but also to the increase in pulling force as the muscle is elongated. The predominance of the pressure change factors in this case can be clearly distinguished. In addition to this, these factors are multiplied by the absolute pressure, whereas the factors accounting for the changing effective area are multiplied by the gauge pressure. Stiffness and compliance are thus mainly determined by the polytropic processes.

Although the situation of closed off muscles will not occur under normal operating conditions, it illustrates the change in volume and the change in effective

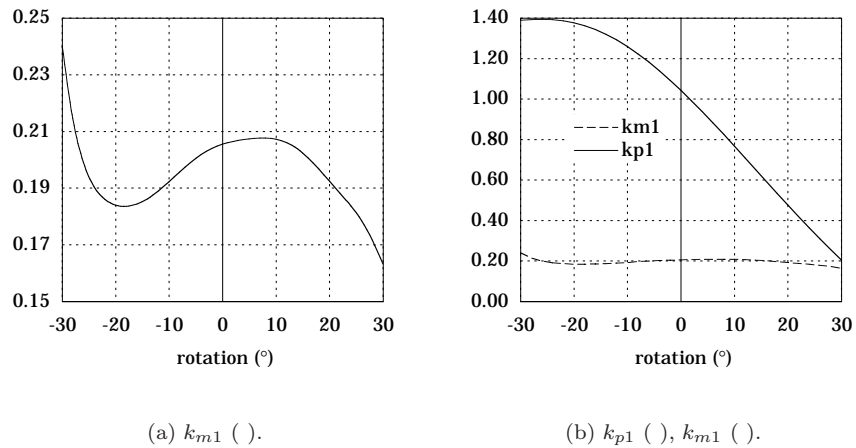
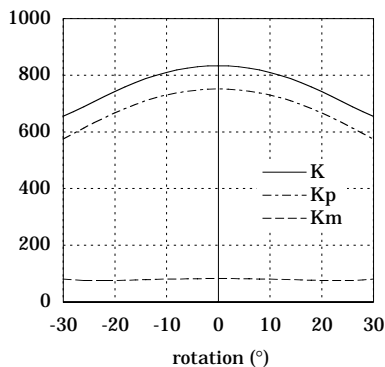


Figure 6.10: Rotative antagonistic actuator stiffness factors and values, closed muscles.



(c) Stiffness values (Nm) with $p_1 = p_2 = 200$ kPa.

Figure 6.10: Rotative antagonistic actuator stiffness factors and values, closed muscles. (cont.)

area as sources of stiffness. As a disturbance moves the actuator out of its equilibrium position, the muscle the actuator is moving towards swells. Hereby its developed force drops because of the inevitable drop in pressure and because of the drop in force function f_t . The other muscle's behavior is opposite to this and, as a result, an equilibrium restoring torque will act on the joint.

If the muscle–valve systems are not closed, as is normally the case, the servo-valves will act and allow a gas flow out of or force a gas flow into a muscle. This can either increase or reduce compliance: if the valves are to sustain the pressure values at the equilibrium levels the compliance will be increased since the terms in $dp_{1(2)}$ will decrease, if, on the contrary, the valves are to restore the equilibrium position at all cost, they will enlarge the pressure changes and thus lower compliance.

6.6 Summary

This chapter described how the developed Pleated PAM can be used to make an antagonistic rotative actuator. Two muscles were connected antagonistically to a revolute joint by means of an eccentric lever arm mechanism. Prototype muscles, as described in Chapter 5 were used. The rotation range was chosen at -30° to 30° , coinciding with a contraction range of 5% to 35% for each muscle. The joint and supporting arm design was discussed. By adjusting the value

of lever arm eccentricity a linear torque to angle of rotation relationship was obtained. This was done to facilitate the actuator control: the actuator position, in the absence of load, is determined by the ratio of the individual muscle gauge pressures, if the sum of these is kept fixed, the position is determined by the difference of the gauge pressures. The actuator static characteristics were derived and the linear torque to rotation relation was experimentally checked. Individual muscle torques were found to range up to 9 Nm at one extreme actuator position and up to 71 Nm at the opposite extreme position.

In an antagonistic PAM set-up, position is determined by the muscle gauge pressures. Pressure regulating servo-valves were chosen to control these and, therefore, they are an integral part of the actuator. These servo-valves set a gauge pressure at their output which is proportional to their input command signal. Step input response tests were done with two kinds of servo-valves, one that is electropneumatically actuated, the other electromagnetically. These tests were performed on muscles at a fixed length and volume. The electromagnetic valve was found to be superior and was thus chosen to control the actuator.

Concluding the chapter, expressions and values of the rotative actuator stiffness were derived in case of closed off muscles. Normally the muscles are not closed off because of the servo-valve operation and compliance and stiffness are therefore actively influenced by this.

Chapter 7

Rotative Actuator Control: the Δp -Approach

7.1 General Considerations

Controlling PAM actuators is generally not an easy task. Firstly, PAMs are non-linear devices, their developed force is a non-linear function of length and applied gauge pressure. Secondly, most of the existing types show dry friction and non-linear elastomer deformation. Thirdly, control is complicated by the compressibility of gas. These effects make it difficult even to establish a practicable model and this is reflected in the proposed control schemes, mainly for McKibben-like muscles.

Linear PID control of position is applied by Inoue (1987) on a Rubbertuator antagonistic actuator. The gauge pressure is regulated by pressure proportional servo-valves. Position step response times of about 1 s are reported. Tondu et al. (1994) describe a SCARA robot actuated by two McKibben muscle pairs and pressure proportional servo-valves. They use servo-valves and a PIDD² scheme combined with feed forward of an estimate from a linear second order model of the muscles and servo-valves to control position. This is the only variable that is controlled, time scales are seconds.

Caldwell et al. (1993a) use a pole placement method based on the results of system identification to obtain position control by pulse width modulated valves; Caldwell et al. (1994, 1995) expand this to an adaptive control algorithm. Settling times are typically in the order of seconds; sinusoidal wave responses show a lag of 180° at a frequency of 0.62 Hz. Adding a load to the actuator or removing it induces a displacement that will be restored after a few seconds.

Beomonte Zobel et al. (1998) report on the use of fuzzy logic to control the

torque generated by an antagonistic McKibben muscles actuator at mid-position. Here also, PWM on-off valves are used. The settling time for a step input of 0 Nm to 45 Nm is 3.5 s or 8 s, depending on the direction of the torque. In addition to these long settling times, this system seems to suffer from a strong directional asymmetry and a residual torque oscillation. Other authors, such as Hesselroth et al. (1994), focus on neural network control, but these, as well, have slow reaction times.

The fundamental reason for developing the Pleated PAM was to avoid energy consuming effects such as friction and membrane material elongation, which are precisely the effects that complicate control. Besides a slight threshold-like behavior due to the enhanced membrane bending resistance brought about by the pleating, as was already mentioned in §5.3.2, none of the other effects are present in the Pleated PAM. Therefore, faster control using simple control techniques, preferably linear, was aimed for. Although the system is non-linear, this can be accomplished, as will be shown in this chapter.

7.2 System Description

The system to be controlled is comprised of the muscles, the linkage mechanism and the servo-valves. It can be derived in full extent from

- the motion governing equation (1 equation),
- the muscle volume to angle relations (2 equations),
- the conservation of energy for each muscle (2 equations),
- the valves' orifice flow rate equations (4 equations),
- the conservation of mass for either muscle (2 equations),
- the ideal gas laws (2 equations).

The actuator is loaded by an external load M_e and by the moments of inertia of all moving parts J . The equation of motion can thus be written using the driving torques approximation of Eq. 6.4 as

$$J\ddot{\alpha} = p_1 l^3 (m_0 - k\alpha) - p_2 l^3 (m_0 + k\alpha) + M_e \quad (7.1)$$

In a first instance losses, such as viscous or dry friction have been disregarded: roller bearings were used for the joint and for the muscle pull rod connections, their friction is very low relative to the values of muscle generated torques;

viscous flow effects of pressurized air are neglected as well, since air viscosity is very low.

The muscle volumes can be approximated, using Eqs. 6.2 and 6.4, by

$$V_1 = V_0 + l^3 m_0 \alpha - \frac{l^3 k}{2} \alpha^2 \quad (7.2a)$$

$$V_2 = V_0 - l^3 m_0 \alpha - \frac{l^3 k}{2} \alpha^2 \quad (7.2b)$$

Expressing the first law of thermodynamics, cf. Eq. B.26, for each muscle leads to

$$\dot{p}_1 = \frac{n}{V_1} \left(rT_s \dot{m}_{1i} - rT_1 \dot{m}_{1e} - (P_0 + p_1) \dot{V}_1 \right) \quad (7.3a)$$

$$\dot{p}_2 = \frac{n}{V_2} \left(rT_s \dot{m}_{2i} - rT_2 \dot{m}_{2e} - (P_0 + p_2) \dot{V}_2 \right) \quad (7.3b)$$

Valve flow rates can be determined by applying Eq. 6.9. Taking compressed air supply temperature equal to ambient temperature, this leads to

$$\dot{m}_{1i} = \frac{A_{1i}}{A_{i\max}} C P_s \rho_0 \Psi(P_0 + p_1, P_s, b) \quad (7.4a)$$

$$\dot{m}_{1e} = \frac{A_{1e}}{A_{e\max}} C (P_0 + p_1) \rho_0 \sqrt{\frac{T_0}{T_1}} \Psi(P_0, P_0 + p_1, b) \quad (7.4b)$$

$$\dot{m}_{2i} = \frac{A_{2i}}{A_{i\max}} C P_s \rho_0 \Psi(P_0 + p_2, P_s, b) \quad (7.4c)$$

$$\dot{m}_{2e} = \frac{A_{2e}}{A_{e\max}} C (P_0 + p_2) \rho_0 \sqrt{\frac{T_0}{T_2}} \Psi(P_0, P_0 + p_2, b) \quad (7.4d)$$

with $A_{1(2)i(e)}/A_{i(e)\max}$ the fraction of valve inlet (exhaust) opening, which is set by the servo-valve controller action. These expressions are completed by the mass conservation expressions:

$$\dot{m}_1 = \dot{m}_{1i} - \dot{m}_{1e} \quad (7.5a)$$

$$\dot{m}_2 = \dot{m}_{2i} - \dot{m}_{2e} \quad (7.5b)$$

Finally, the ideal gas equations, which are well known, are expressed as

$$m_1 r T_1 = (P_0 + p_1) V_1 \quad (7.6a)$$

$$m_2 r T_2 = (P_0 + p_2) V_2 \quad (7.6b)$$

The introduction of angular speed as a new variable, $\dot{\alpha} = \beta$, results in a set of fourteen equations—ten first order linear differential and four algebraic—in fourteen variables $p_{1(2)}$, $T_{1(2)}$, $V_{1(2)}$, $\dot{m}_{i1(2)}$, $\dot{m}_{e1(2)}$, $\dot{m}_{1(2)}$, α and β and depending on four input parameters defining the valve opening fractions. Eliminating $V_{1(2)}$ and their derivatives using Eqs. 7.2, $\dot{m}_{i1(2)}$ and $\dot{m}_{e1(2)}$ using Eqs. 7.4, and $T_{1(2)}$ using the ideal gas equations, reduces this set to six first order linear differential equations, which, subsequently, can be put in canonic form:

$$\mathbf{A}(\mathbf{X}) \dot{\mathbf{X}} = \mathbf{B}(\mathbf{X}) \quad \text{with} \quad \mathbf{X} = [\beta \ \alpha \ p_1 \ p_2 \ m_1 \ m_2]^T \quad (7.7)$$

This set is not easy to use, not only because of the non-constant coefficients of the differential equations but also because of the difficulty of determining the valve openings when using pressure proportional servo-valves. These valves have an independent built-in pressure control loop, which makes them active elements in the system. Unfortunately, the servo-valve system description is usually undisclosed information.

For these reasons a more practical approach was taken. This is based on the linear variation of muscle generated torque with angle in isobaric conditions. Because of that, the angular displacement, in the absence of an external load and in static conditions, is directly proportional to the difference of muscle pressures if the sum of their pressures is kept at a constant level, as was seen from Eq. 6.5. In the presence of loads, Eq. 7.1 can be rearranged to

$$J\ddot{\alpha} + (p_1 + p_2)kl^3\alpha = (p_1 - p_2)m_0l^3 + M_e \quad (7.8)$$

If the pressure control is able to keep the sum of both gauge pressures fixed, this expression represents a linear system with input Δp , defined as

$$p_1 = p_m + \Delta p \quad (7.9a)$$

$$p_2 = p_m - \Delta p \quad (7.9b)$$

notating p_m for the mean value of both muscle pressures. The motion equation can then be rewritten as

$$J\ddot{\alpha} + 2p_mkl^3\alpha = 2m_0l^3\Delta p + M_e \quad (7.10)$$

The gauge pressures, in turn, are set by the servo-valves reacting to their input signals

$$U_1 = U_m + \Delta U \quad (7.11a)$$

$$U_2 = U_m - \Delta U \quad (7.11b)$$

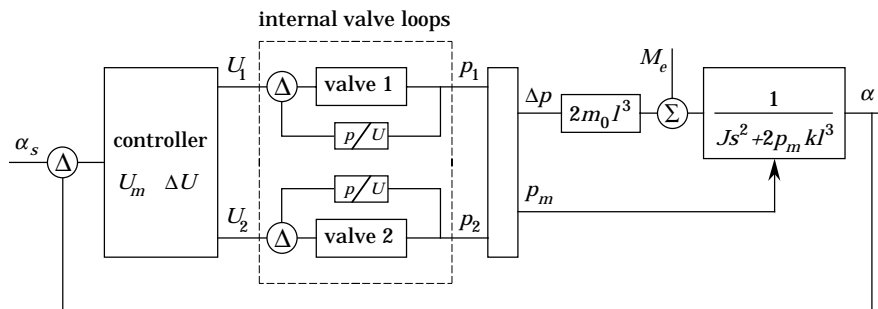


Figure 7.1: Control system block diagram.

and, consequently, these will be the actual system input signals that need to be set by the controller to be designed. The resulting control system will then have a double loop structure: each valve has its built-in loop regulating the muscle gauge pressure according to its input signal, which will be provided by the outer loop. The internal loops use gauge pressure as output feedback, while the external loop will use angular displacement for this purpose. Fig. 7.1 shows the block diagram of the complete control system.

7.3 Dynamic Characterization

In order to determine whether the representation of Eq. 7.10 can be regarded as linear and, if so, to characterize it, unloaded open-loop step input tests were done. The actuator was treated as a black box with as input the valve signals $U_{1(2)}$, and as output angular position. At a constant value of mean valve input signal U_m , valve command signals were suddenly changed according to

$$U_1 = U_{10} + \delta U \quad (7.12a)$$

$$U_2 = U_{20} - \delta U \quad (7.12b)$$

and the resulting angular displacement and muscle gauge pressures were sampled every 10 ms. The values of δU were aimed to coincide as well as possible with small displacements of a fixed value. Enough tests were done to cover the complete range of motion in both directions. The equipment used for these tests is the same as that used to test the performance of the servo-valves (cf. Chapter 6). The length of tubing was 10 cm and its internal diameter 4 mm.

7.3.1 Step Test Results

Fig. 7.2 shows results of such tests performed using the Tecno valves. Displacements were set at $\pm 2^\circ$, the mean gauge pressure p_m at 100 kPa. Four of the step responses are shown, these were chosen to be representative for the complete test. They illustrate the inconsistent behavior of the actuator if these valves are used: for some displacements responses seem vaguely first order like, others show a significant overshoot or even a halfway stalling effect. This could be expected from the results of the Tecno valve tests discussed in §6.4.2, which showed their overshoot and disturbance sensitivity. Furthermore, the changes in pressures during the open-loop step tests are very small, $p_m \approx 5$ kPa, and the valves can accordingly be expected to perform even worse because of valve sen-

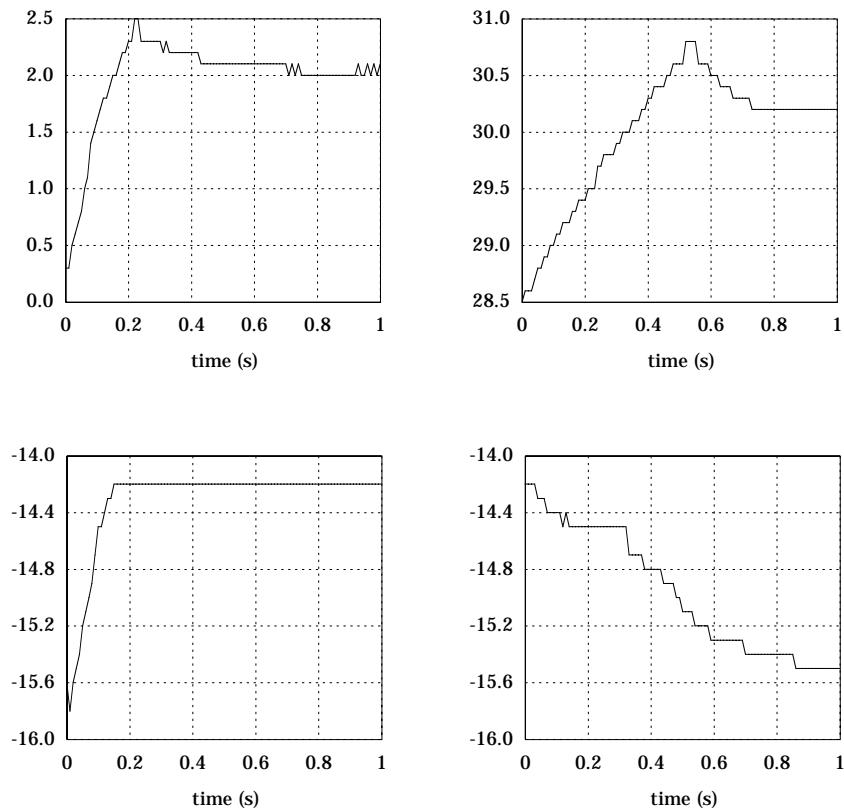


Figure 7.2: Open-loop step responses ($^\circ$) using Tecno valves.

sitivity and hysteresis—the technical specifications state values of 0.016 V and 1.6 kPa, respectively, for these effects. The stepwise evolution of the rotation is due to the resolution of the angle measurement, which is at 0.1° . Although the actuator position in the absence of load can be successfully controlled using these valves (Daerden et al., 1998), this discussion will focus on the use of the KPS 3/4 valves.

Using the KPS 3/4 servo-valves the tests were done in steps of 3° . This way, displacement steps of -30° to -27° , -27° to $-24^\circ \dots 27^\circ$ to 30° , and of 30° to $27^\circ \dots -27^\circ$ to -30° were imposed during a test run and each response was measured during 1.5 s. The values of U_m were set to have a mean muscle gauge pressure of 50 kPa, 100 kPa, 150 kPa, 200 kPa and 250 kPa. Each test run was

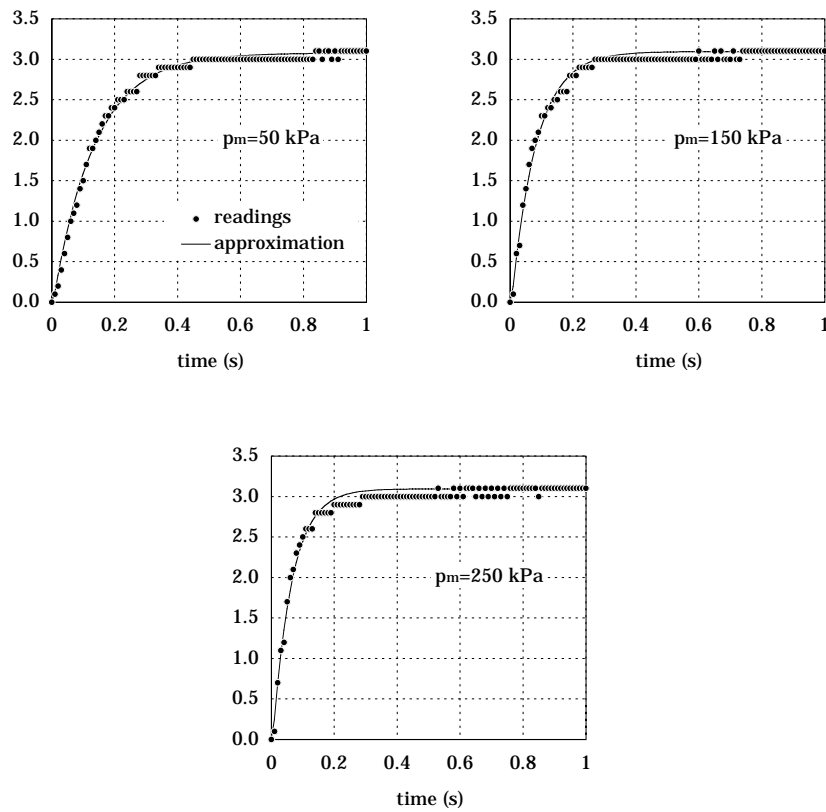


Figure 7.3: Open-loop step responses ($^\circ$) using KPS 3/4 valves.

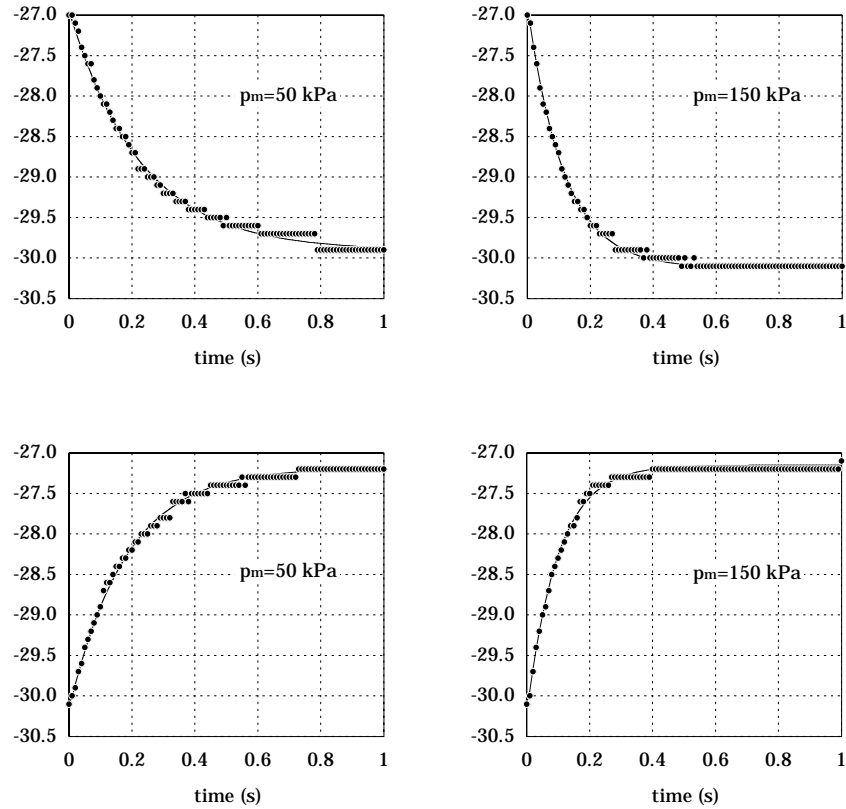


Figure 7.3: Open-loop step responses ($^{\circ}$) using KPS 3/4 valves. (cont.)

repeated three times in order to evaluate response consistency and dispersion. The diagrams of Fig. 7.3 show a representative sample of test results. To obtain a displacement of 3° , Δp had to be set at about 5 kPa for $p_m = 50$ kPa, 13 kPa for $p_m = 150$ kPa and 22 kPa for $p_m = 250$ kPa.

The displacement courses were very consistent throughout the ranges of motion and pressure. No overshoot, disturbance sensitivity, stalling or other detrimental effects were witnessed. Once the end value was reached, the actuator remained stable at that position. The charts show a clear influence of mean pressure: the higher the value of mean gauge pressure, the quicker the actuator settles at its end value. This can be explained from the results of the valve tests displayed in Fig. 6.8, which showed how a higher level of gauge pressure

lowers valve response times. Comparing the settling times of Fig. 7.3 to these of Fig. 6.8 one can notice the effect of the change of volume, as was discussed in the concluding remarks of §6.4.2: settling times for a moving antagonistic actuator are roughly double that of a single muscle undergoing the same pressure change at a fixed length.

The experimental data for each response were approximated by a first order exponential function with a time delay of 5 ms, i.e. the valve time delay, using a least squares method. For each response the sum of the squares of the differences between measured and approximation values, taken at all 150 sampling points, was minimized by changing the value of time constant. Results of this are included in the diagrams of Fig. 7.3. The match between experimental and approximation values, taking into account the angle measurement's resolution of 0.1° , is very good. The averages and standard deviations of the sum of the squared differences for all responses at a fixed value of gauge pressure and moving in one direction are listed in Table 1. The values of angle were put in degrees. A very good agreement between experimental and approximated data is clear from these. This cannot be easily explained; it seems to be due to a coincidence of operating characteristics, i.e. the valve pressure regulating characteristics and the actuator relationships of muscle volume to angular displacement.

Table 1.

p_m (kPa)	-30° to 30°		30° to -30°	
	AV	STDV	AV	STDV
50	0.511	0.217	0.535	0.195
100	0.342	0.109	0.313	0.092
150	0.404	0.187	0.551	0.205
200	0.637	0.187	0.640	0.197
250	0.636	0.159	0.991	0.514

Fig. 7.4 shows the values of the apparent first order time constants for test runs at three different settings of mean muscle gauge pressure. The scattering of time constants between test runs is about 10–20% with regard to their average values. The narrower displacement span at high mean pressures is due to the muscle gauge pressure upper limit which is set at 300 kPa.

The averaged values are displayed by the diagrams of Fig. 7.5. These diagrams show the influence of the value of p_m , the higher its value the faster the reaction times, as was explained before. This influence gradually diminishes, which can be directly related to the results of the valve tests displayed in Fig. 6.8. The time constants are at a minimum around mid-position, this appears to be an

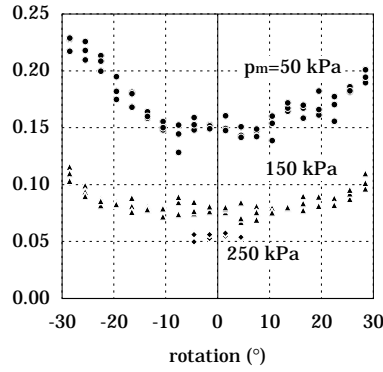


Figure 7.4: Apparent open-loop system time constants (s), moving from 30° to -30° at various mean muscle gauge pressures.

ideal combination of muscle volumes and pressures. When moving towards the outer positions, one of the muscles' volume increases while the other one's pressure lowers. As was seen from the valve tests these effects slow down the pressure regulating.

The tests were repeated for displacements of 1° and 5° to examine the influence of step height. Results of these tests are included in the diagrams of Fig. 7.6, which compare the average time constants with values of p_m equalling 50 kPa

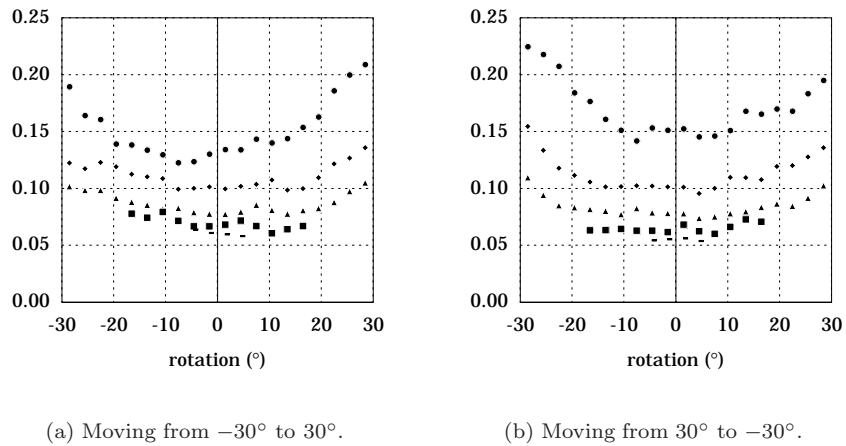
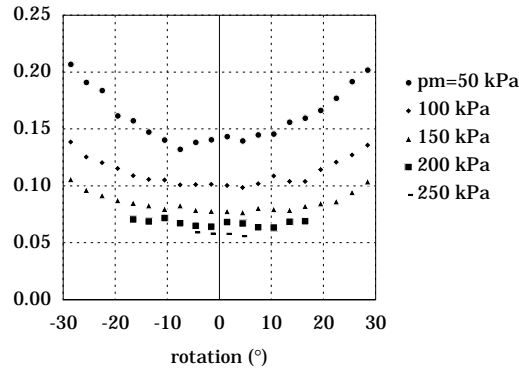


Figure 7.5: Apparent open-loop system time constants (s), averaged values.



(c) Both way average.

Figure 7.5: Apparent open-loop system time constants (s), averaged values. (cont.)

and 150 kPa. Except for the low muscle pressures and a step of 1° , the difference in apparent time constants is negligible. For the smallest step changes one can notice a more capricious scattering of the data. This can be related to the very small values of pressure change to be set, down to ≈ 2 kPa, which will be complicated by valve sensitivity and hysteresis.

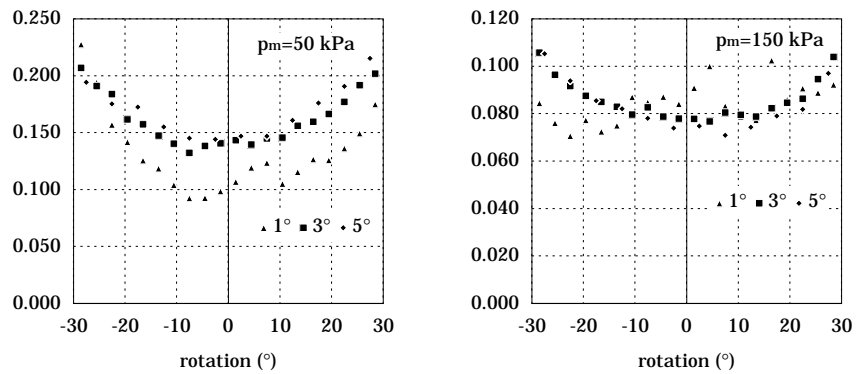


Figure 7.6: Apparent time constants (s) at different displacement steps.

7.3.2 System Model

The inertial load present during the tests can be neglected. The rotating link was brought down to the lever mechanism which has a moment of inertia of $5.7 \times 10^{-4} \text{ kg m}^2$ and, with an mean lever arm taken at 2.7 cm, the linearly moving muscle parts have an equivalent moment of inertia of approximately $7 \times 10^{-5} \text{ kg m}^2$. The total moment of inertia has thus a value of about $6.4 \times 10^{-4} \text{ kg m}^2$. With apparent time constants above 60 ms, an estimate of maximum acceleration is given by

$$\frac{\Delta\alpha}{\tau^2} = \frac{5\pi}{180 \times 0.06^2} \approx 24 \text{ rad/s}^2 \quad (7.13)$$

The resulting load in that case is only 0.015 Nm, which is marginal relative to the developed muscle torques.

Therefore, and with $\Delta p = \Delta p_0 + \delta p$, the motion equation, Eq. 7.10, simplifies to

$$\delta\alpha = \alpha - \alpha_0 = \frac{m_0}{k} \frac{\delta p}{p_m} \quad (7.14)$$

where the start angle of rotation α_0 is defined by

$$\alpha_0 = \frac{m_0}{k} \frac{\Delta p_0}{p_m} \quad (7.15)$$

Concluding from the tests described above, a first order model with a time delay can then be used to describe the antagonistic actuator, including its servo-valves, in the absence of load:

$$\delta\alpha(s) = \frac{m_0}{U_m k} \frac{e^{-t_d s}}{1 + \tau s} \delta U(s) = K_\alpha H(s) \delta U(s) \quad (7.16)$$

with $m_0/k = 0.138/0.207 \text{ rad} \approx 0.67 \text{ rad}$, as was found in §6.3, $t_d = 5 \text{ ms}$ and the time constant τ having values ranging between approximately 60 ms and 200 ms, depending on p_m and α . If loads are present, the first order and time delay system will still represent the gauge pressure evolutions and, hence, the full model expression:

$$\delta\alpha(s) = K_\alpha \frac{H(s)}{1 + (s/w_n)^2} \delta U(s) + \frac{1}{2p_m k l^3} \frac{M_e(s)}{1 + (s/w_n)^2} \quad (7.17)$$

with the natural frequency defined as

$$\omega_n = \sqrt{\frac{2p_m k l^3}{J}} \quad (7.18)$$

This model will be referred to as the Δp -model, since it requires a pressure increase in one muscle to be accompanied by an equal decrease in the other in order to be valid. Its control will accordingly be referred to as the Δp -control. It should be noted that the full actuator system is a non-linear system irrespective of the conclusions of the open-loop step tests. Because of the (approximately) linear torque to rotation angle relationship a linear treatment of the system for small displacements is possible if the condition of a constant sum of muscle pressures is satisfied. Even then, the time constant is dependent on the muscles' mean pressure and on the position. Slight deviations of p_m from its set value during position control are allowed, as will be seen in the course of the next sections dealing with the outer loop control algorithm. Their influence on the value of system time constant is not very important, as can be concluded from the results displayed in Fig. 7.5.

It should be emphasized as well, that the model is strongly valve dependent. If the Tecno valves are used instead of the KPS 3/4, the first order approximation is not possible, as was clear from the open-loop tests in that case. The first order and time delay representation is a consequence of the interaction between the actuator static characteristics, as summarized in Fig. 6.4, the valves' flow characteristics and their pressure regulating characteristics.

7.4 Position Control, Unloaded Case

A direct consequence of the Δp -approach is the necessity of an integral part in the controller. If a new equilibrium position is to be set, the muscle pressures and, hence, the valve signals need to be changed permanently. The examined control system to accomplish this with, is an output feedback PI-controller. Its block diagram is sketched in Fig. 7.7. The controller transfer function is defined as

$$C(s) = K_P + \frac{K_I}{s} \quad (7.19)$$

Such a controller was implemented digitally, using the same equipment as was used for the valve tests and for the step input tests. The sampling period was

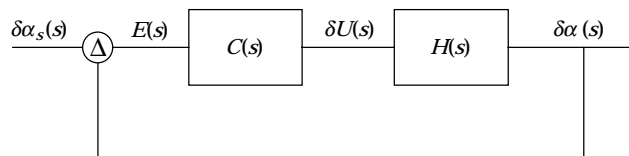


Figure 7.7: Control system block diagram.

set at 10 ms, which is the minimum of the used digital control hardware and software system. In view of the values of time constants and the time delay of 5 ms, this seems fast enough. The controller output has a saturation level which is set to prevent the valve command signals from exceeding the values of $2U_m$ and 3 V. This is done because 0 V is the lowest valve input signal and, thus, if this is reached, the other valve's signal is stuck at a value of $2U_m$. On the other hand the maximum allowable gauge pressure limit is 300 kPa and therefore 3 V is not to be exceeded and if it is reached the other signal is fixed at $(2U_m - 3)$ V.

According to Bühler (1988) a pseudo-continuous treatment of the digital control system is allowed as long as the sampling period T_s is small with regard to the dominant time constants of the controlled system. More precisely, $T_s \leq \tau/2$, which, in this case, with the dominant time constant at a minimum of about 60 ms and $T_s = 10$ ms, is satisfied.

The digital control law is expressed as

$$\delta U_n = K_P E_n + K_I T_s \sum_{i=0}^n E_i \quad (7.20)$$

To determine its Laplace transform one can proceed as described by Kuo (1980) and Bühler (1988):

$$\delta U_n - \delta U_{n-1} = K_P (E_n - E_{n-1}) + K_I T_s E_n \quad (7.21)$$

of which the Laplace transform is

$$(1 - e^{-sT_s})\delta U^*(s) = K_P(1 - e^{-sT_s})E^*(s) + K_I T_s E^*(s) \quad (7.22)$$

where $\delta U^*(s)$ and $E^*(s)$ represent the Laplace transforms of the data series taken at the sampling instants. For the sampled data series E_n one can write

$$E^*(s) = \frac{1}{T_s} \sum_{n=-\infty}^{\infty} E(s + jn\omega_s) \quad (7.23)$$

and in the primary strip ($-\omega_s \leq \omega \leq \omega_s$) this is reduced to

$$E^*(s) = \frac{E(s)}{T_s} \quad (7.24)$$

if no aliasing occurs. The controller output signal is subjected to a zero order sample and hold device whose output is the actual input of the Δp -model. Therefore,

$$\delta U(s) = \frac{1 - e^{-sT_s}}{s} \delta U^*(s) \quad (7.25)$$

Combining the last equations leads to

$$\delta U(s) = K_P \frac{1 - e^{-sT_s}}{sT_s} E(s) + \frac{K_I}{s} E(s) \quad (7.26)$$

A first order Padé approximation for e^{-sT_s} can be used to replace the transcendental function by a rational:

$$e^{-sT_s} \approx \frac{1 - sT_s/2}{1 + sT_s/2} \quad (7.27)$$

The pseudo-continuous representation of the digital control law is then expressed as

$$\begin{aligned} \delta U(s) &\approx \frac{K_P}{1 + sT_s/2} E(s) + \frac{K_I}{s} E(s) \\ &= K_I \frac{1 + \tau_c s}{s(1 + sT_s/2)} E(s) \end{aligned} \quad (7.28)$$

with

$$\tau_c = \frac{K_P}{K_I} + \frac{T_s}{2} \quad (7.29)$$

The controlled system's transfer function, which relates position output to error and is defined as $G_{ol}(s) = \delta\alpha(s)/E(s)$, is thus represented by

$$G_{ol}(s) \approx \frac{0.67K_I}{U_m} \frac{(1 + \tau_c s)e^{-t_d s}}{s(1 + sT_s/2)(1 + \tau s)} \quad (7.30)$$

This is a transfer function having a small delay time t_d and a small time constant $T_s/2$ with regard to the dominant time constant τ . The time delay can be approximated according to Bühler (1988) by a first order time constant and, hence, the transfer function simplifies to

$$G_{ol}(s) \approx \frac{0.67K_I}{U_m} \frac{1 + \tau_c s}{s(1 + sT_s/2)(1 + t_d s)(1 + \tau s)} \quad (7.31)$$

7.4.1 Integral Control

To evaluate the system description derived above, tests were done using a purely integral control law. In this case $K_P = 0$ and the open-loop transfer function is written as

$$G_{ol}(s) \approx \frac{0.67K_I}{U_m} \frac{1}{s(1 + t_d s)(1 + \tau s)} \quad (7.32)$$

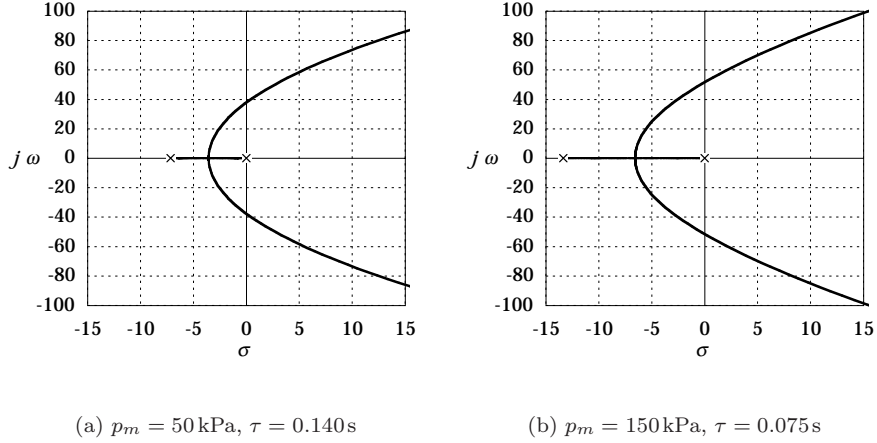


Figure 7.8: Root loci of Δp -I-controlled system around mid-position.

Typical root locus plots of the closed-loop system are shown in Fig. 7.8. The far-off regions are not plotted because the approximations made are not valid there. Besides, in view of the values of τ , high frequencies will be sufficiently damped. The approximative system description of Eq. 7.32 has two dominant poles, one in the origin and one at $\sigma = -1/\tau$. From there two branches of the locus depart along the real axis, from which they break away where they meet. They converge towards asymptotes at an angle of $\pm \pi/3$ with respect to the real axis as K_I tends to infinity. The third branch of the locus, which is not visible on the diagram, starts from $\sigma = -1/t_d$ and runs along the real axis towards $-\infty$.

The system is destabilized if the integral control gain K_I exceeds a limiting value $(K_I)_l$, which can be found by expressing the purely imaginary character of the poles of the closed-loop system:

$$\frac{0.67(K_I)_l}{U_m} + j\omega_l(1 + t_d j\omega_l)(1 + \tau j\omega_l) = 0 \quad (7.33)$$

which, since $t_d \ll \tau$, yields

$$\frac{0.67(K_I)_l}{U_m} \approx \frac{1}{t_d} \quad \text{and} \quad \omega_l = \sqrt{\frac{1}{t_d \tau}} \quad (7.34)$$

In practice the risk for instability is high because the root locus is located close to the imaginary axis. This was observed experimentally, as can be seen from Fig. 7.9, which displays the results of positioning the actuator from 0°

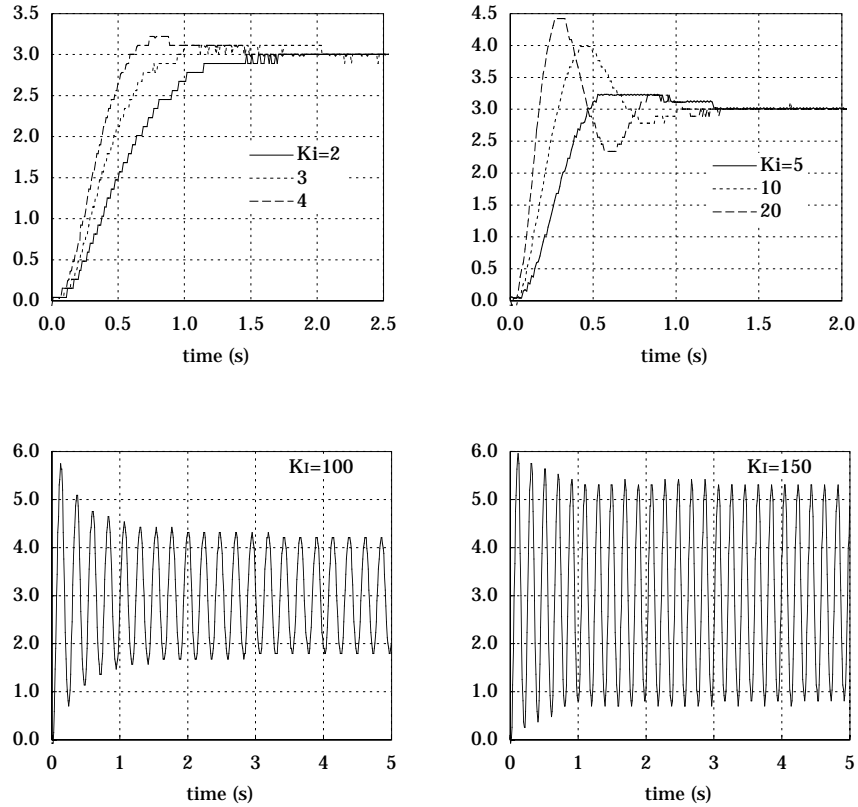


Figure 7.9: Positioning results ($^{\circ}$) of the Δp -I-controlled system with varying integral gain and $p_m = 50$ kPa.

to 3° at $p_m = 50$ kPa ($U_m = 0.5$ V). In these conditions τ was found to be 0.140 s in §7.3.1 and, thus, $(K_I)_l \approx 150$ V/rad s and $\omega_l = 37.8$ rad/s. Overshoot occurs if K_I exceeds a value ranging between 2 V/rad s and 3 V/rad s; the value predicted by the model, i.e. when the root locus breaks away from the real axis, is 1.3 V/rad s. As the integral gain increases the system moves at higher speeds but shows progressively more overshoot and a tendency towards oscillation. The oscillation amplitude is limited at first ($\approx 1.1^{\circ}$ for $K_I = 100$ V/rad s) and increases as the gain increases to a limit of about 3° . The amplitude is limited because the controller output values are limited to the saturation levels and because polytropic compression and expansion processes will start to affect the actuator. The latter is due to the increasing actuator speed if the oscillation

amplitude increases. The valves will not be able to keep up with the speed of muscle volume changes and compression and expansion effects will thus gain in importance and generate position restoring torques. The maximum oscillation amplitude is reached if the gain exceeds the value of 300 V/rad s. The frequency of oscillation increases with K_I , as was predicted by the model. At $K_I = 150$ V/rad s, i.e. the point of instability of the model, the measured frequency is 32.0 rad/s, which is somewhat lower than the predicted value of 37.8 rad/s.

Instability emerges in an unusual way: as from $K_I = 100$ V/rad s a permanent oscillation remains, although its amplitude has decremented with regard to the start of the control process, the decrement gradually diminishes as K_I increases, until the amplitude is more or less fixed, which happens around $K_I = 150$ V/rad s. For other conditions and displacement ranges, the observed sustained oscillations had amplitudes as low 0.2°. This limit cycle is probably caused by the quantization of the angular measurement: the PEP ADC3 converter has a resolution of 12 bit, which makes for a 0.09° or 0.0015 rad quantization on the value of α . With $K_I = 100$ V/rad s, this leads to an output signal quantization of $0.0015 \times T_s \times K_I = 1.5$ mV, which corresponds to a pressure of 0.15 kPa, whereas the value of Δp to jump from 0° to 3° was seen to be 5 kPa.

The diagrams show the slowness of the actuator, which could be expected from the purely integral control action. This is especially emphasized if one compares them to the open-loop responses shown in Fig. 7.3. Even if the mean gauge pressure increases, the actuator remains sluggish, as is confirmed by the diagrams of Fig. 7.10, showing similar results at a mean gauge pressure of 150 kPa.

The steady state error of the position lies within a margin of $\pm 0.1^\circ$, which is also the angular measurement's resolution. The actuator oscillates somewhat within these margins, even at low integral gain values.

Table 2 lists experimental data of the gain at the onset of instability, the oscillation's frequency at that point and its amplitude, together with the predicted values of $(K_I)_l$ and ω_l . For the outer ranges, motion in both directions was considered in order to examine whether the slight asymmetry in time constants that could be seen from the test results of Figs. 7.5(a) and 7.5(b) had an important influence, which does not appear to be the case.

One can conclude from the tests that the behavior of the system is as predicted by Eq. 7.31, but that the values of oscillation frequencies and corresponding integral gains divert from the predicted values. Instability is, however, not only caused by the time delay but also by the ADC converter quantization. Because of this and because of the narrow margin between the root locus and the imaginary axis in the left-half s -plane, instability occurs at lower values of integral gain than expected. Furthermore, the dispersion of the measured

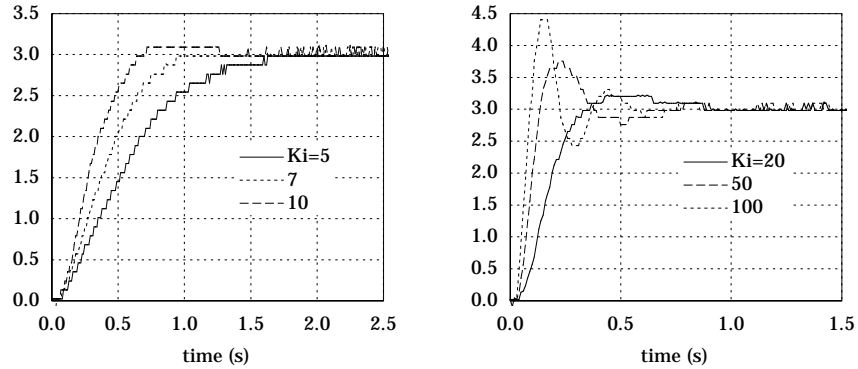


Figure 7.10: Positioning results ($^{\circ}$) of the Δp -I-controlled system with varying integral gain and $p_m = 150$ kPa.

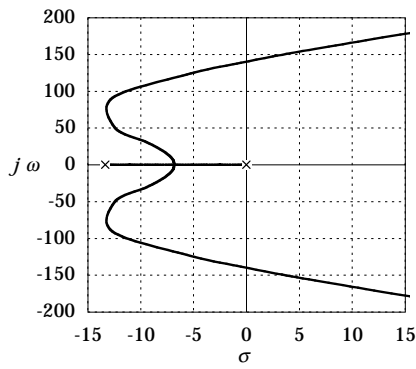
apparent time constants and the dispersion of the value of time delay, which cannot be expected to equal exactly 5 ms in all conditions, will cause a deviation between the actual values and those predicted by the model. Considering for instance the position course of 0° to 3° at a mean gauge pressure of 50 kPa, an oscillation frequency of 32.0 rad/s at an integral gain of $K_I = 150$ V/rads was observed. Putting these values in the expressions of Eq. 7.34 and assuming they represent the stability limit, yields $\tau = 0.146$ s and $t_d = 6.7$ ms, which do not deviate very much from the model values of 0.140 s and 5 ms, respectively.

Table 2.

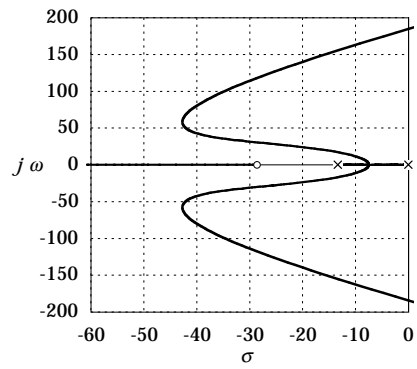
displacement ($^{\circ}$)	p_m (kPa)	K_I (V/rads)	$(K_I)_l$ (V/rads)	ω (rad/s)	ω_l (rad/s)	amplitude ($^{\circ}$)
0–3	50	95	150	24.5	37.8	0.8
0–3	150	280	450	36.4	51.6	0.5
0–3	250	400	750	36.4	57.7	0.3
15–18	50	115	150	25.1	35.4	1.0
18–15	50	105	150	25.1	35.4	1.0
15–18	150	300	450	35.8	42.6	0.5
18–15	150	280	450	34.6	42.6	0.3
27–30	50	150	150	19.5	31.6	1.0
30–27	50	140	150	24.5	31.6	1.0
27–30	150	300	450	32.0	39.2	0.3
30–27	150	280	450	32.0	39.2	0.2

7.4.2 Proportional-Integral Control

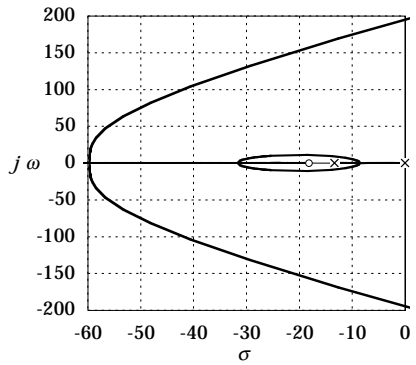
The effect of adding a proportional term to the control law is to introduce a zero and a remote pole in the open-loop transfer function, as is clear from Eq. 7.31. The zero is located at $\sigma = -1/\tau_c$, which is determined by the ratio of both controller gains and the sampling period (cf. Eq. 7.29). As the value of K_P/K_I increases, it moves closer to the origin and affects the root locus



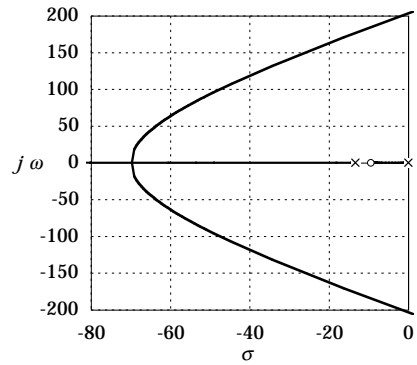
(a) $K_P/K_I = 0.01\text{ s}$, $1/\tau_c = 66.7\text{ s}$



(b) $K_P/K_I = 0.03\text{ s}$, $1/\tau_c = 28.6\text{ s}$



(c) $K_P/K_I = 0.05\text{ s}$, $1/\tau_c = 18.2\text{ s}$



(d) $K_P/K_I = 0.1\text{ s}$, $1/\tau_c = 9.52\text{ s}$

Figure 7.11: Root loci of a Δp -PI-controlled system around mid-position, $p_m = 150\text{ kPa}$, K_P/K_I fixed.

as shown in Fig. 7.11. The root locus now has four branches, the asymptotes are at $\pm \pi/3$ and π . The zero has a tendency to draw the upright branches towards the left-half s -plane and towards higher values of ω . When it nears the dominant actuator pole, the root locus shows a small loop about these two. If the zero is smaller than the dominant pole a small branch starting from the origin and ending in the zero is created. This will cause a slow integral component entering the overall behavior.

The root locus can also be calculated with K_p as parameter and K_I fixed. The characteristic equation of the closed-loop controlled system is rearranged for this purpose, from

$$\frac{0.67K_I}{U_m} \frac{1 + \tau_c s}{s(1 + sT_s/2)(1 + t_d s)(1 + \tau s)} + 1 = 0 \quad (7.35)$$

to

$$\frac{K_p s}{(1 + sT_s/2)(K_I + \frac{U_m}{0.67} s(1 + t_d s)(1 + \tau s))} + 1 = 0 \quad (7.36)$$

and results of this are diagrammed in Fig. 7.12. It shows how the proportional term can speed up the system response to a step input and at the same time increase the damping. Adding proportional control to an instable I-controlled system has a potential for stabilizing, as is clear from the second diagram, and,

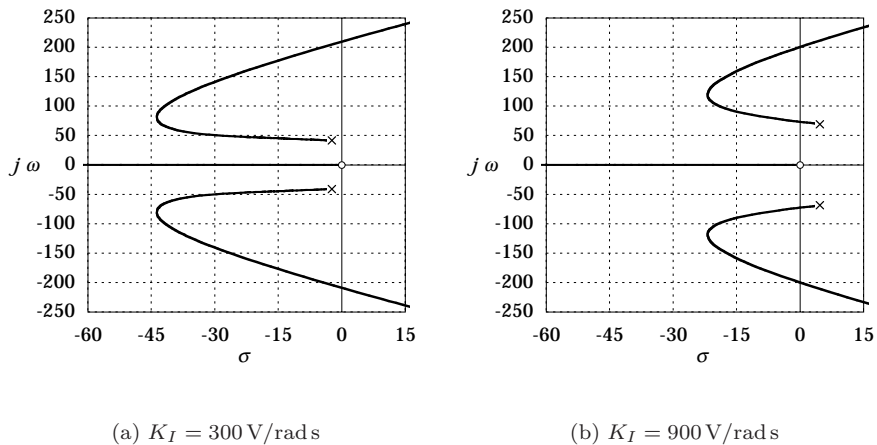


Figure 7.12: Root loci of a Δp -PI-controlled system around mid-position, $p_m = 150$ kPa, K_I fixed.

hence, allows the open-loop gain to be increased. If the value of proportional gain is too high, however, the system destabilizes again. Moreover, one of the system poles also nears the origin, slowing down response times. There is a marked difference in oscillation frequency for instability brought about by too big an integral gain and by too big a proportional gain. The latter will be higher with regard to the first.

Fig. 7.13 shows readings of step responses for a step of 0° to 3° at a mean muscle gauge pressure of 150 kPa and an integral gain of 300 V/rads. As predicted, the system stabilizes by introducing a proportional term in the control; if the proportional gain increases too much, destabilization occurs again, but at a higher frequency. The predicted value of K_P to destabilize the system is 72 V/rad, which is a lot higher than the measured value of 25 V/rad. The amplitude at this point, however, is only 0.4° and, therefore, the quantization

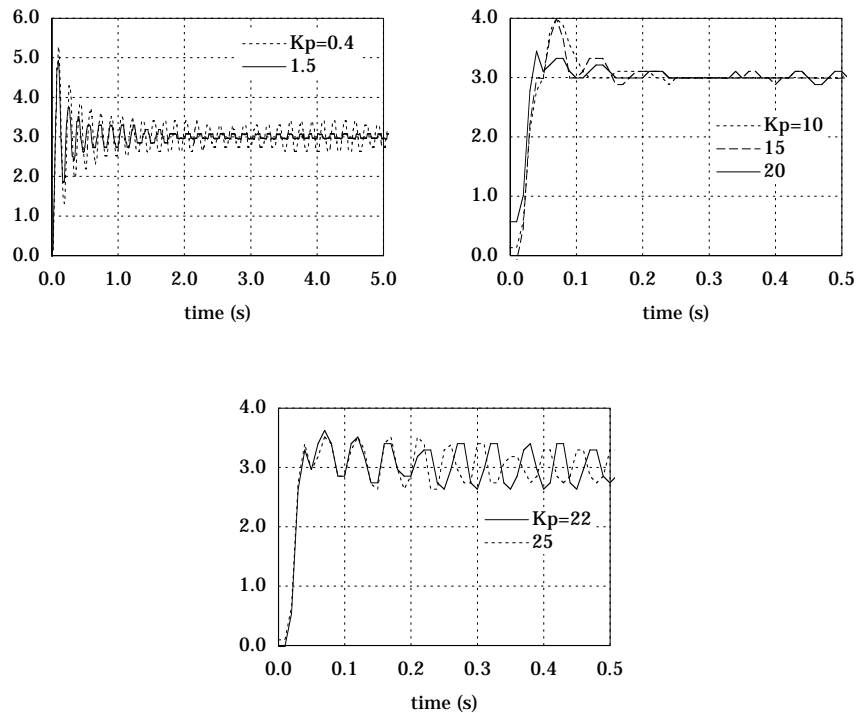
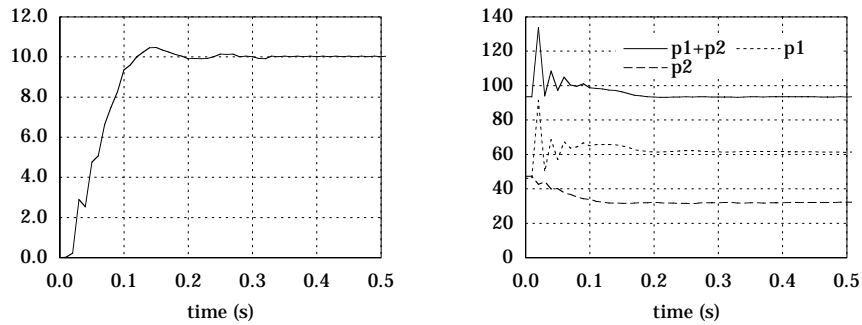


Figure 7.13: Input step responses ($^\circ$) for a Δp -PI-controlled system, U_m set at 1.5 V and K_I at 300 V/rads, varying K_P .

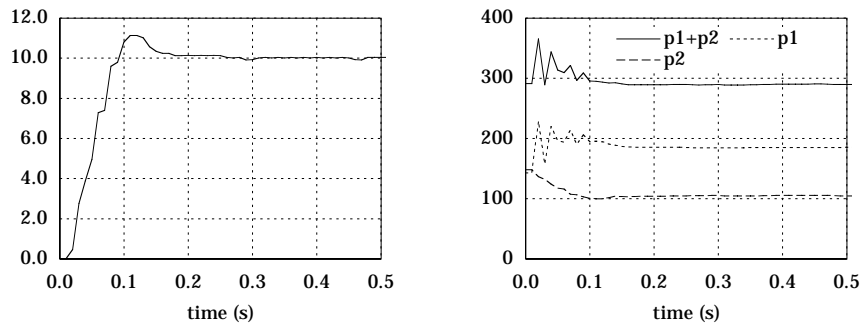
error is assumed to lead to a limit cycle as was the case in the I-controlled system.

For $K_I = 450 \text{ V/rad s}$ good values of K_P were found to range within 9 V/rad to 13 V/rad , although an overshoot of 1.5° was observed. At $K_P = 30 \text{ V/rad}$ the system oscillates at a sustained amplitude of 1.4° and a frequency of 157 rad/s ; the model yields a damped oscillation at a frequency of 145 rad/s and a damping ratio of 0.18 . Again, with such a low value of damping ratio, the quantization error can be expected to lead to a limit cycle.

Setting higher values of integral gain never led to a stable result, although



(a) $p_m = 50 \text{ kPa}$, $K_I = 150 \text{ V/rad s}$, $K_P = 6 \text{ V/rad}$.

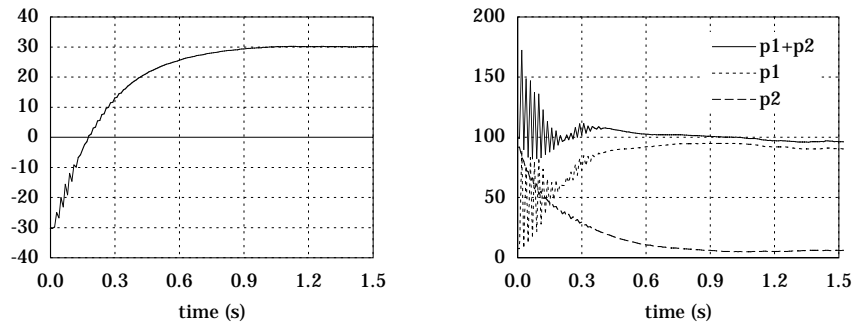


(b) $p_m = 150 \text{ kPa}$, $K_I = 300 \text{ V/rad s}$, $K_P = 12 \text{ V/rad}$.

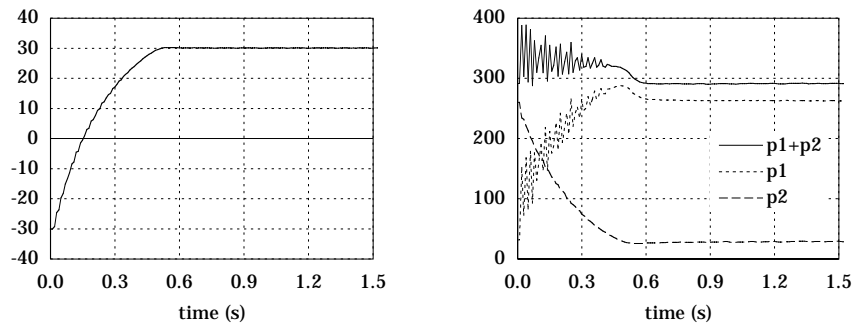
Figure 7.14: 0° to 10° input step responses ($^\circ$) and gauge pressure readings (kPa) for a Δp -PI-controlled system.

the model predicts this should be the case, cf. Fig. 7.12(b). The narrow margin between the root locus and the imaginary axis and quantization of the angular measurement can, once more, be cited as the probable causes for this. Measurements at other values of integral gains confirmed the findings of the model.

Figs. 7.14 to 7.16 display some typical broad range displacement input step test responses. Jumps from 0° to 10° , -30° to 30° , which is the full range motion, 25° to 30° and 30° to 25° at various values of mean muscle gauge pressure are shown. It is clear how the system, at these step sizes, can no longer be



(a) $p_m = 50 \text{ kPa}$, $K_I = 150 \text{ V/rads}$, $K_P = 6 \text{ V/rad}$.

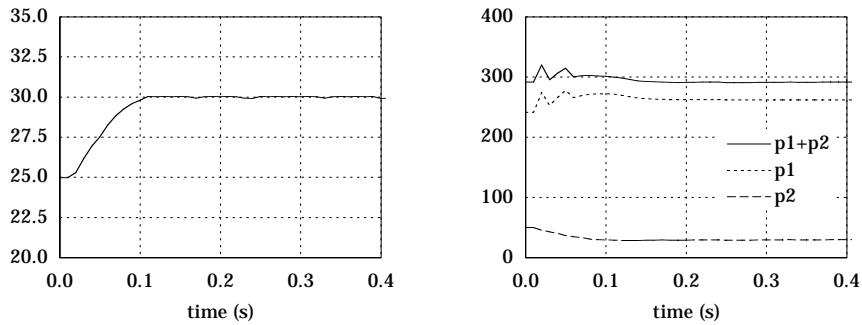


(b) $p_m = 150 \text{ kPa}$, $K_I = 300 \text{ V/rads}$, $K_P = 12 \text{ V/rad}$.

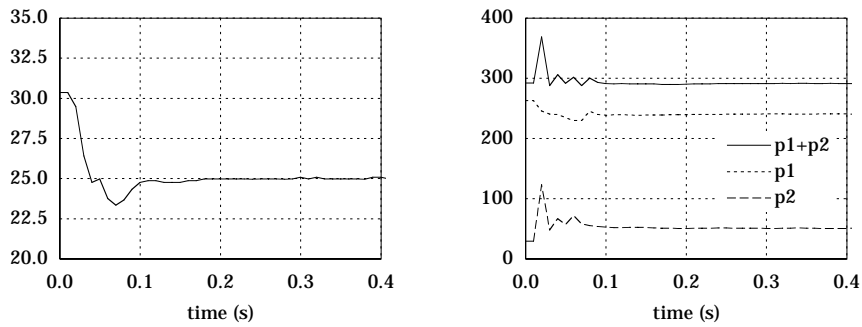
Figure 7.15: Full range input step responses ($^\circ$) and gauge pressure readings (kPa) for a Δp -PI-controlled system.

regarded as linear, since the response is decidedly dependent on the step size: comparing Fig. 7.14(b) to Fig. 7.13 an increase in rise time—the time interval from the start of the input step to the first crossing of the set value—from about 40 ms to about 100 ms is obvious. A full range displacement, with the same controller gains and mean pressure, takes about half a second. Higher values of p_m increase the actuator speed because of the resulting lower value of the system’s dominant time constant, as was seen before.

The responses to a full range step prove the point made in the concluding remarks of §6.4.2: as the actuator nears its extreme position, it slows down.



(a) $p_m = 150$ kPa, $K_I = 300$ V/rads, $K_P = 12$ V/rad.

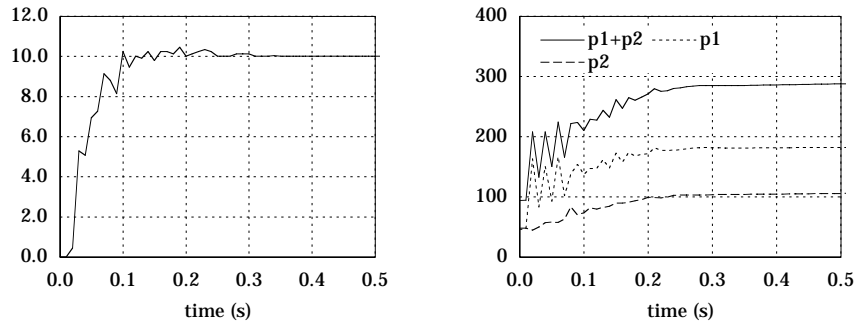


(b) $p_m = 150$ kPa, $K_I = 300$ V/rads, $K_P = 12$ V/rad.

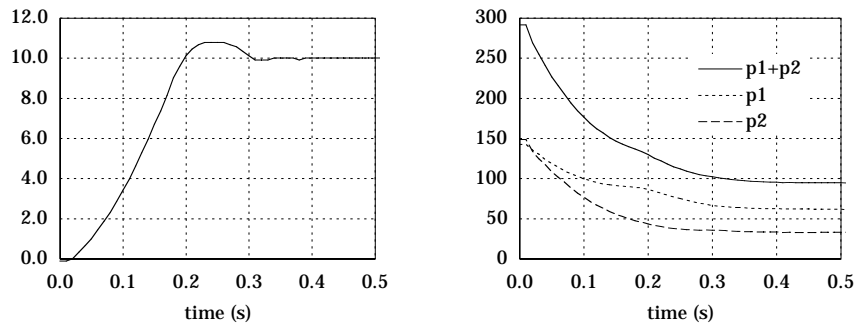
Figure 7.16: 25° to 30° and 30° to 25° input step responses (°) and gauge pressure readings (kPa) for a Δp -PI-controlled system.

This can be related to the dropping pressure time course, which is an almost perfect inversion of the position time course. The departure from an extreme, on the other hand is very swift. These effects are accentuated by the asymmetry of the 5° step responses taken near an extreme, shown by Fig. 7.16. The diagrams of the time courses of muscle pressures indicate how in all cases the deflating muscle limits the speed.

The gauge pressure diagrams plot the sum of the measured gauge pressures. During the settling phase, it deviates from its set value but this does not seem to have an important effect on the control behavior. An oscillation of the charged muscle's pressure is observed. This is the same as was apparent from the valve

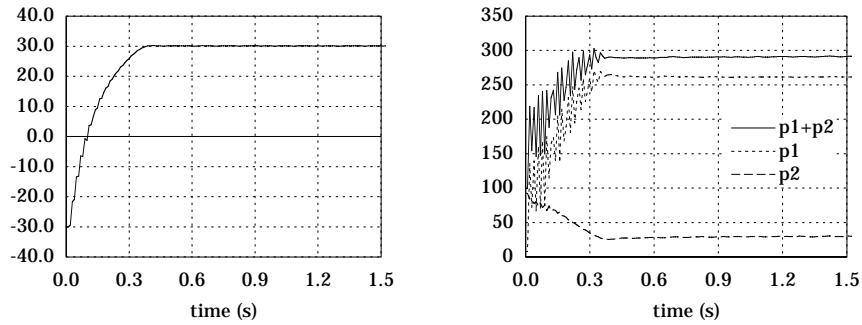


(a) U_m : 0.5 V to 1.5 V, $K_I = 300$ V/rads, $K_P = 12$ V/rad.

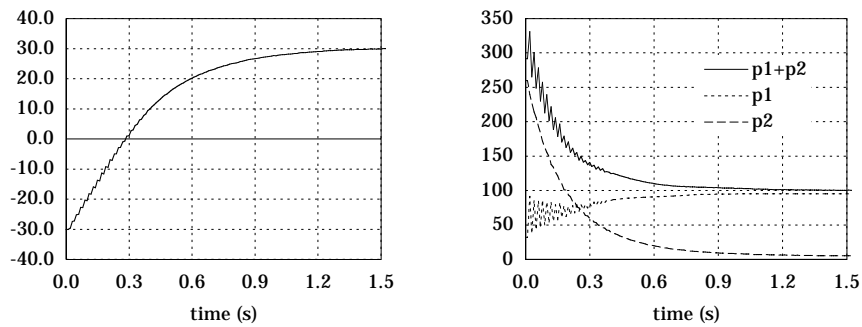


(b) U_m : 1.5 V to 0.5 V, $K_I = 150$ V/rads, $K_P = 6$ V/rad.

Figure 7.17: Responses ($^\circ$) to step in set angle and U_m and gauge pressure readings (kPa) for a Δp -PI-controlled system.



(c) U_m : 0.5 V to 1.5 V, $K_I = 300$ V/rads, $K_P = 12$ V/rad.



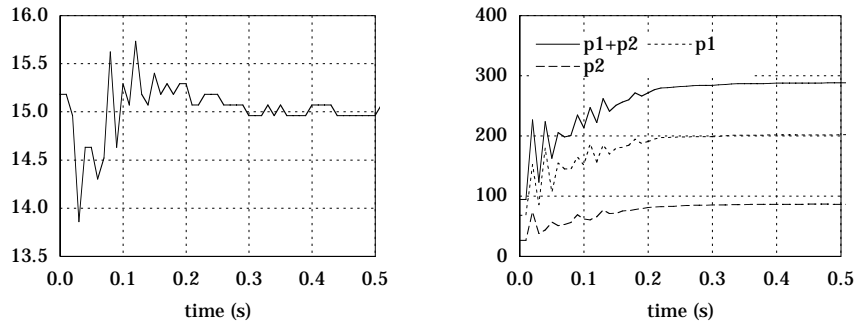
(d) U_m : 1.5 V to 0.5 V, $K_I = 150$ V/rads, $K_P = 6$ V/rad.

Figure 7.17: Responses ($^\circ$) to step in set angle and U_m and gauge pressure readings (kPa) for a Δp -PI-controlled system. (cont.)

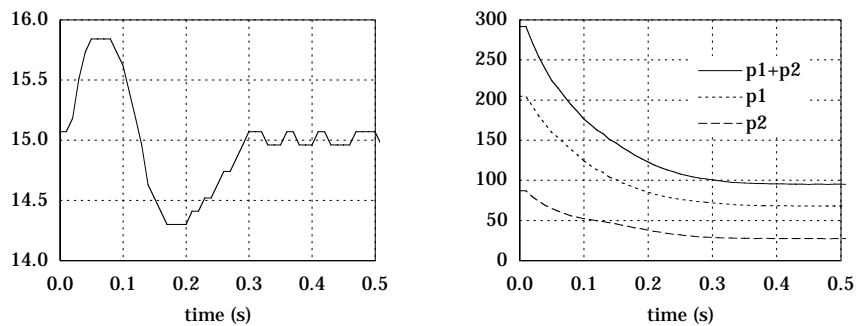
tests of §6.4.2 and affects the displacement by introducing small shudders at the start of the response.

In spite of these non-ideal and non-linear effects, the control algorithm of the outer loop can be maintained. The reason for this is the inherent stability brought about by the antagonistic operation and the validity of the linear model if the actuator is near enough to its end-position.

Fig. 7.17 shows results of step tests that put a sudden change to U_m as well as to the set angle. The change in mean valve command signal is immediately transmitted to the valves by the controller: each actual valve signal is multiplied by the ratio of the new mean voltage to the actual and this value is set at the first



(a) U_m : 0.5 V to 1.5 V, $K_I = 300$ V/rads, $K_P = 12$ V/rad.



(b) U_m : 1.5 V to 0.5 V, $K_I = 150$ V/rads, $K_P = 6$ V/rad.

Figure 7.18: Responses ($^\circ$) to step in U_m and gauge pressure readings (kPa) for a Δp -PI-controlled system positioned at 15° .

sampling instance. Subsequently the controller takes these new valve signals as the start values to which its output has to be added. The values of controller gains are changed as the value of the mean signal command tension changes. This is necessary because of the dependence of the system time constant τ on the mean gauge pressure, as was concluded from §7.3.1. The diagrams show how an increase in U_m speeds up the actuator and a decrease slows it down. The reason for this can be found in the change in individual muscle gauge pressure time courses. To increase p_m , the drop in pressure in one muscle will diminish or even change to a rise and, as a result, its speed limiting effect will be reduced. At the same time, the rise in the other muscle's pressure and its

power to pull the actuator to its end position will be enhanced. Decreasing p_m , on the other hand, will cause enhanced pressure drops and diminished rises, that can even change to drops.

Fig. 7.18 shows how the Δp -PI-controlled actuator deals with a step change in U_m while staying at an equilibrium position, which, in the case of the displayed results is 15° . An excursion of less than 1° is observed for a change of mean pressure of 50 kPa to 150 kPa. The reaction to an increase in mean pressure is more nervous than to a decrease because of the valve nervousness, as was discussed earlier. The reaction lasts for about 200 ms to 300 ms, depending on the amplitude of the step. During these tests, the muscle volumes remained at a near constant value and, therefore, a similarity between the pressure evolutions of Figs. 7.18 and 6.7 can be seen. Similar tests at $\alpha = 0^\circ$ and $\alpha = 30^\circ$ showed excursions of within 0.5° while the settling times remained similar.

7.4.3 Controller Influence on Compliance/Stiffness

Stiffness was expressed in its basic form by Eq. 6.13. Assuming the controlling system able to keep the Δp -condition satisfied at all times, the changes in muscle pressures are

$$\frac{dp_1}{d\alpha} = -\frac{dp_2}{d\alpha} \approx \frac{\delta p}{\delta\alpha} \quad (7.37)$$

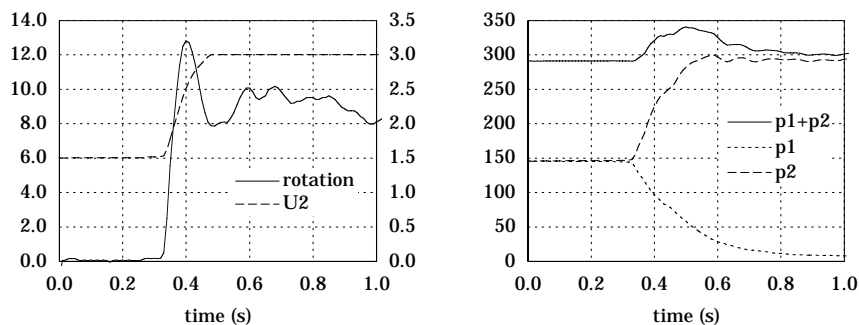
Introducing this and the linear torque approximation of Eq. 6.4 in the expression of stiffness results to

$$K \approx 2kl^3 p_m - 2m_0 l^3 \frac{\delta p}{\delta\alpha} \quad (7.38)$$

If the angular position is suddenly changed the controller will react by instructing the valves to change the muscle pressures in order to restore the position. This will be a dynamic process since a PI-control algorithm is used. Because of the integral action a progressively growing term will be added as the deviation from the set value is sustained. The restoring torque and, hence, stiffness will increase until the controller output has reached its saturation level.

Fig. 7.19 shows the results of a test where a sudden change in angular position was imposed on the Δp -PI-controlled actuator. This was done by hand, as can be seen from the fluctuating time course of rotation angle. It shows clearly the effect of the integral control: the position restoring muscle's valve input signal increases until saturation is reached and its gauge pressure then reaches the maximum allowable level, the other muscle is completely let off.

Only position is, consequently, controlled by the Δp -PI-control system. This is evident since it acts solely on the position error signal. Compliance could be



(a) Rotation angle ($^{\circ}$), left hand, valve signal (V), right hand.

(b) Muscle gauge pressures (kPa).

Figure 7.19: Δp -PI-controlled system response to an imposed displacement jump.

controlled by an open-loop position control system that would set the position by regulating the pressure at fixed values. These are determined from the values of the gauge pressure ratio and the mean muscle gauge pressure. The pressure ratio is obtained from the desired position and is calculated from the values of m_0 and k and Eq. 6.5. The mean gauge pressure is deduced from the desired compliance, whose steady state value is now expressed as

$$C \approx \frac{1}{2kl^3p_m} \quad (7.39)$$

Such an open-loop controller could be made to give the actuator a soft touch by calculating the muscle developed torques from the pressure readings and, from these, the value of its external load. This could be set to a predefined maximum in order not to damage any obstacles. An increasing external load could even make the actuator yield. This kind of controller would give precedence to the setting of compliance instead of position, which is the opposite from the Δp PI-approach.

7.5 Influence of Inertial Load

If an inertial load is present two purely imaginary poles, $\pm j\omega_n$, are added to the system transfer function. This has a destabilizing effect on the system and complicates its control. Using the previously discussed PI-control scheme now

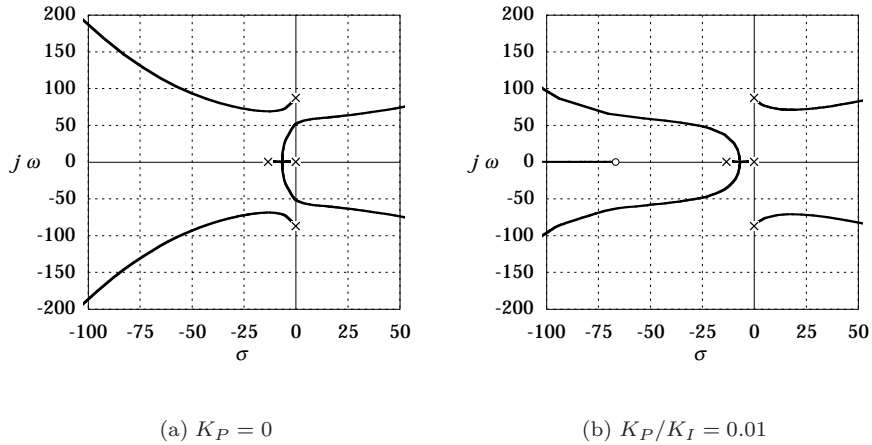


Figure 7.20: Effect of an inertial load on the root loci of a Δp -PI-controlled system around mid-position, $p_m = 150$ kPa, $J = 0.0082$ kg m², $\omega_n = 87.2$ rad/s.

leads to a root locus having six branches and asymptotes at $\pm \pi/5$, $\pm 3\pi/5$ and π , as is shown by Fig. 7.20. It is clear from these that a classic PI-approach is not very suitable. With the proportional gain zero and the integral gain at the stability limit value, the natural frequency poles have evolved towards the left-half s -plane but still have a damping ratio of only 0.09. Introducing a proportional part does not improve this situation, on the contrary, at fairly

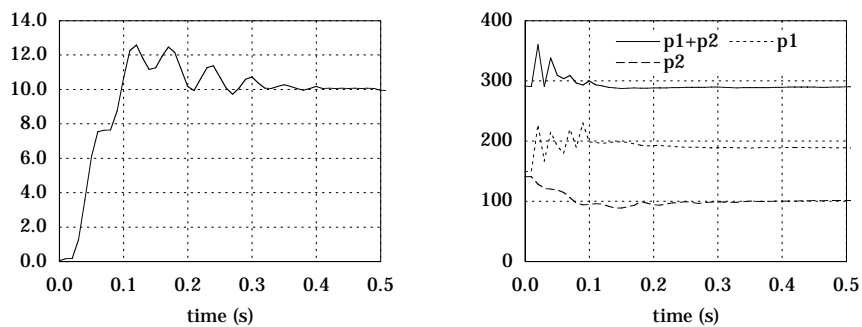


Figure 7.21: Step input response ($^\circ$) and gauge pressures (kPa) of a Δp -PI-controlled system around mid-position, $J = 0.0082$ kg m².

low values of proportional to integral gain ratios, the direction of the upright branches is reversed and the system is permanently unstable. If the natural frequency decreases—due to an increased moment of inertia or by a lower mean gauge pressure—the branches starting from the natural frequency poles will move towards the right-half s -plane for lower gain ratios or even immediately, destabilizing the system no matter what the values of K_I and K_P are.

Fig. 7.21 plots the response to a step input of 10° when a moment of inertia of $J = 0.0082 \text{ kg m}^2$ is attached to the effector. The controller gains were set at $K_I = 100 \text{ V/rad s}$ and $K_P = 6 \text{ V/rad}$ and the mean gauge pressure at 150 kPa . The rise time is comparable to the unloaded case but, because of the extra second order part of the system, overshoot and oscillations are stronger. If the value of the proportional gain is increased from 6 V/rad to 7 V/rad , the system turns unstable and starts oscillating at an amplitude of 15° and a frequency of 113 rad/s ; the gauge pressures oscillate at an amplitude of about 70 kPa .

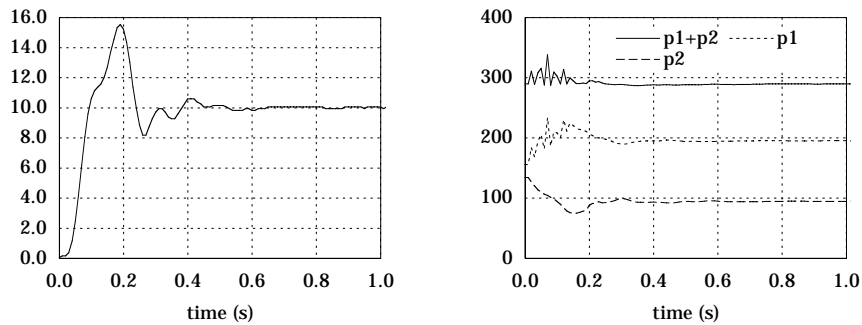


Figure 7.22: Step input response ($^\circ$) and gauge pressures (kPa) of a Δp -PI-controlled system around mid-position, $J = 0.0281 \text{ kg m}^2$.

Fig. 7.22 plots similar results for a moment of inertia of $J = 0.0281 \text{ kg m}^2$. The controller gains were now set at $K_I = 100 \text{ V/rad s}$ and $K_P = 1.5 \text{ V/rad}$ and the mean gauge pressure at 150 kPa . Instability occurred as from $K_P = 3 \text{ V/rad}$, confirming the findings of the root locus discussion, and at a frequency of 61 rad/s .

Insufficient damping is the main reason for the inaptness of the controller. Some energy consuming effects are inevitably present—the resistance of the muscle membranes to their bulging and the friction inside the bearings of the joint and muscle attachment pivots—but these are hardly enough to provide sufficient damping to the system. Adding damping, e.g. viscous friction, seems necessary.

7.6 Summary

A state variable representation for the rotative actuator system—two muscles, the linkage mechanism and two servo-valves—was derived in this chapter. Because of the unknown servo-valve flow sections during operation and because of the non-constant coefficients of the differential equations, state feedback control using this description was avoided. Instead of this, an angular position output feedback control was tried. This is based on what was named the Δp -approach: since a linear approximation of the static muscle torque to angle relations is possible (cf. Chapter 6) the motion governing equation can be linearized if the servo-valves can keep the sum of both muscle gauge pressures fixed, this equation then represents a linear system with the difference of both gauge pressures as input. The resulting controller has to calculate the valve command signals from the deviation between the set value and the measured value of the angular position. The servo-valves' built-in control systems subsequently set the pressures according to their input command signals.

This approach was validated by open-loop tests measuring displacement responses to valve command signal steps. In the absence of load a first order and time delay system was found to represent the pressure difference between both actuator muscles in an accurate way. The time delay is caused by the valve operation and equals 5 ms. The first order time constants depend on the mean muscle gauge pressure and to a lesser extent on the angular position, they range between 60 ms and 200 ms. The proposed Δp -approach was found to be an effective method to provide a linear treatment of the non-linear actuating system. The actuator linear torque to rotation relation and fast pressure regulation are the main reasons for this.

Based on this approach linear control techniques were used. A PI-control law yielded very good results in the absence of loads. The integral term is necessary because a permanent displacement is only possible if the pressures are permanently changed. The controller gains are dependent on the mean gauge pressure, however, because of the influence of this parameter on the system time constant. The presented position controller is fast and accurate, with steady state position errors within a margin of 0.1° , at a displacement range of 60° .

The influence of the position controller on joint compliance/stiffness was examined. The position control system intentionally changes the actuator compliance in order to reach a set position. A sustained deviation from that point will cause the stiffness to increase progressively until the controller reaches its saturation level. The reason for this was seen to be the integral control action. A compliance controller that acts on the known torque to angle relations and measured muscle gauge pressures could be designed. The actuator could this

way be made to yield if an obstacle is met on its course. Its positional accuracy would not be as good, since it would lack a feedback control loop acting on the value of position.

Finally, the destabilizing influence of inertial loads was discussed. The danger of instability is enhanced because of the extra poles, representing the system's natural frequency, that are introduced. Adding damping to the system was seen to be necessary in this case. Using still faster pressure regulating servo-valves will have a beneficiary effect on the overall system stability as this increases the dominant time constant and, hence, takes the root loci further away from the imaginary axis.

Chapter 8

Conclusions

The need of appropriate actuators will always be acute as new applications will always arise and the demands of existing applications will continuously evolve. This work aims to be a meaningful contribution in satisfying this need. It was set out to find an apt walking and running machines engine but resulted in the development of a new actuator as few existing engines meet this application's requirements—lightweight, high values of torques at low and moderate speeds, direct joint connection, natural compliance, shock resistance and possible autonomous operation.

The developed actuator, which complies with the demands, is pneumatically powered and belongs to the family of Pneumatic Artificial Muscles. It was named Pleated Pneumatic Artificial Muscle. PAMs are distinguished from the more common pneumatic cylinder by their changing force to length relationship, as if they had a changing piston head area. This is due to their shape changing property. An important consequence of this is the unique relation between the equilibrium position of an antagonistic PAM actuator and the ratio of its muscle gauge pressures. Pressure control, instead of mass flow control, is the key to position control for this kind of actuator. Another major difference is weight: whereas cylinders are typically made of aluminum or plastics, a PAM's core element is its membrane which is, obviously, extremely lightweight.

In this dissertation a comprehensive account was given of the development of the Pleated PAM. Its concept, a cartridge pleated inflatable membrane, was explained starting from a formal mathematical model. Other ways of folding are possible as well, and several were tried in the course of action leading to this work. None of these had the same contraction capacity as cartridge pleating. The design and a prototype construction were discussed. Material choices and stress loadings were considered for this. The resulting weight of a 10 cm long Pleated PAM of a diameter of 2.5 cm is as low as 58 g. Using copper instead of

aluminum led to a weight of 116 g.

The agreement between the characteristics derived by the mathematical model and the observations is very good. Because of this, the developed tensional force can be safely predicted from the readings of position and gauge pressure. The model showed all geometric characteristics to be dependent on muscle slenderness, its full length and a parameter gathering the applied gauge pressure and the membrane material properties. In case of a high tensile stiffness membrane material, all properties depend on slenderness and full length alone and the developed force is proportional to the gauge pressure. Geometric similarity laws were derived for this case, allowing the muscles to be tailored to the needs of the particular application.

A rotative actuator was built using Pleated PAMs as powering devices and its use to control position was examined. The muscles are directly attached to the joints by pull rods. The static torques developed by the muscles vary between values of only a few Nm to over 70 Nm, depending on the position and on the applied gauge pressure. Thanks to a linkage mechanism design leading to a linear torque to rotation relationship, a linear treatment of this non-linear system was possible. A proportional-integral control law was proposed and found to be very effective and accurate in the absence of inertial load. Overshoot and danger of instability were shown to be enhanced by the inertial load proving the need of damping. It was indicated how the actuator can be used as a compliance controlled device, giving it the capacity to handle delicate tasks that need a soft touch.

Central elements in the control of the revolute joint actuator are the pneumatic valves. These have to control the flow of gas in and out of the muscles in order to regulate their gauge pressures and, as such, they decisively determine the actuator's dynamic behavior and power rating. Several types of servo-valves were tried and an electromagnetic servo-valve was chosen as best option.

Research is, of course, never finished and it is the task of any researcher to indicate the focus of future attention. In this case, two main areas can be distinguished: muscle fabrication and control elements. The main problems that will be faced from the point of view of fabrication are the machining of the folds in a cylindrically closed membrane and the connection of the membrane to the end fittings. At this point the membrane has a seam running parallel to the muscle axis and this, of course, is a weak spot.

From the point of view of control elements several items are to be examined. First of all, the nervousness of the servo-valves that were used in this work indicate that pressure regulating speed can be enhanced. This would allow to use a greater closed-loop feedback gain for the actuator and increase its stability. Valve weight, now at 1 kg, is a second item that needs attention. It can be brought down, however, to about 300 g because of its modular design. Using

plastics where possible should lower the weight further. To date, pneumatic valve technology is apparently not focussed on weight reduction. Making the rotative actuator modular, that is, with embedded sensors and controller, is another objective to be set.

Life span tests should be performed. These should give an indication not only about the life expectancy, but also about the failure mechanism. At this point it can only be said that after extensive testing, often in the damaging conditions of instability testing, the prototype muscles show no signs of deterioration. Because of the bidirectional weave damage can be expected to occur gradually and not in a catastrophic way: if the liner is pierced or if membrane fabric fibers break, air will leak out of the muscle and its pulling force will then be diminished. This was witnessed on earlier and less successful models.

Besides these items, other aspects of technological research will inevitably arise as more experience will be gained by using the Pleated PAM.

Appendix A

Elliptic Integrals of the First and Second Kind

The canonical form of an elliptic integral of the first kind is (Abramowitz and Stegun, 1965; Erdelyi, 1981)

$$F(\varphi | m) = \int_0^\varphi \frac{d\theta}{\sqrt{1 - m \sin^2 \theta}} \quad (\text{A.1})$$

or

$$F(x | m) = \int_0^x \frac{dt}{\sqrt{(1 - t^2)(1 - mt^2)}} \quad (\text{A.2})$$

with $x = \sin \varphi$ and $m = \sin^2 \alpha$, and of that of the second kind

$$E(\varphi | m) = \int_0^\varphi \sqrt{1 - m \sin^2 \theta} \, d\theta \quad (\text{A.3})$$

or

$$E(x | m) = \int_0^x \sqrt{\frac{1 - t^2}{1 - mt^2}} \, dt \quad (\text{A.4})$$

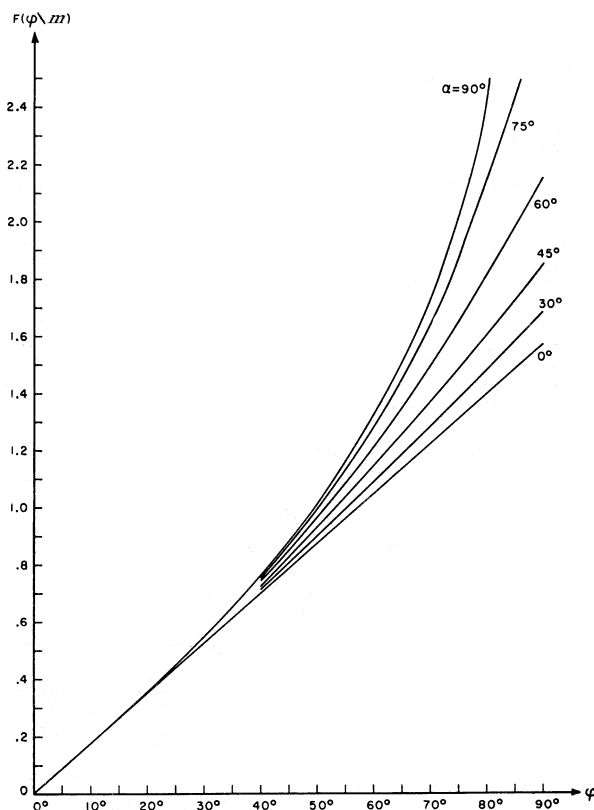


Figure A.1: Elliptic integral of the first kind. (Abramowitz and Stegun, 1965)

m is the parameter of the integral, α the modulus and φ the amplitude.

Integrals of this form, but having m outside the interval $[0, 1]$, can be transformed to standard elliptic integrals using the transformation formulas

$$F(\varphi \setminus m) = \sqrt{\hat{m}} F(\hat{\varphi} \setminus \hat{m}) \tag{A.5}$$

$$E(\varphi \setminus m) = \sqrt{\frac{1}{\hat{m}}} (E(\hat{\varphi} \setminus \hat{m}) - (1 - \hat{m}) F(\hat{\varphi} \setminus \hat{m})) \tag{A.6}$$

with $\hat{m} = 1/m$ and $\sin \hat{\varphi} = \sqrt{m} \sin \varphi$.

All elliptic integrals can be reduced to a combination of the integral of a rational function and the three canonical forms of the elliptic integral using

$$Y^2 = a_0 r^4 + 4a_1 r^3 + 6a_2 r^2 + 4a_3 r + a_4 \tag{A.7}$$

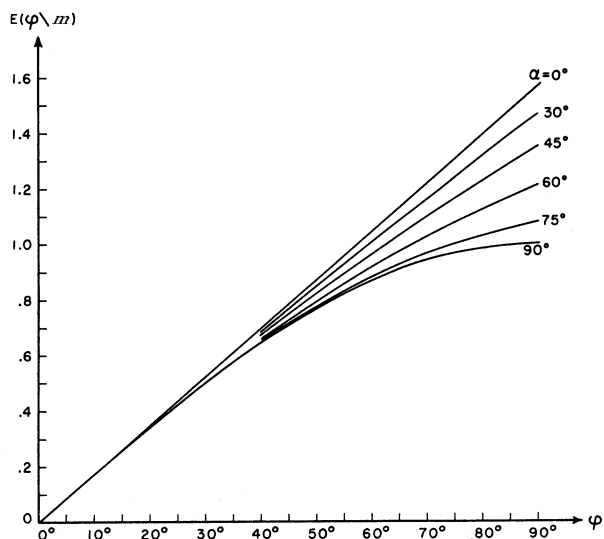


Figure A.2: Elliptic integral of the second kind. (Abramowitz and Stegun, 1965)

$$I_n = \int \frac{r^n}{Y} dr \tag{A.8}$$

and the reduction rule

$$r^n Y = (n + 2)a_0 I_{n+3} + 2(2n + 3)a_1 I_{n+2} + 6(n + 1)a_2 I_{n+1} + 2(2n + 1)a_3 I_n + na_4 I_{n-1} \tag{A.9}$$

or, in differential form:

$$\frac{d}{dr}(r^n Y) = (n + 2)a_0 \frac{r^{n+3}}{Y} + 2(2n + 3)a_1 \frac{r^{n+2}}{Y} + 6(n + 1)a_2 \frac{r^{n+1}}{Y} + 2(2n + 1)a_3 \frac{r^n}{Y} + na_4 \frac{r^{n-1}}{Y} \tag{A.10}$$

Appendix B

First Law of Thermodynamics Applied to a Pneumatic Artificial Muscle

In general the conservation of energy of a control volume with one inlet and one exit flow (Fig. B.1) can be stated in its rate form as (Moran and Shapiro, 1992)

$$\dot{Q}_{cv} = \frac{dE_{cv}}{dt} + \dot{W}_{cv} + \dot{m}_e \left(h_e + \frac{C_e^2}{2} + gz_e \right) - \dot{m}_i \left(h_i + \frac{C_i^2}{2} + gz_i \right) \quad (\text{B.1})$$

where \dot{Q}_{cv} is the net rate of heat transfer into the control volume and \dot{W}_{cv} the net rate of technical work done by the control volume and crossing its boundary.

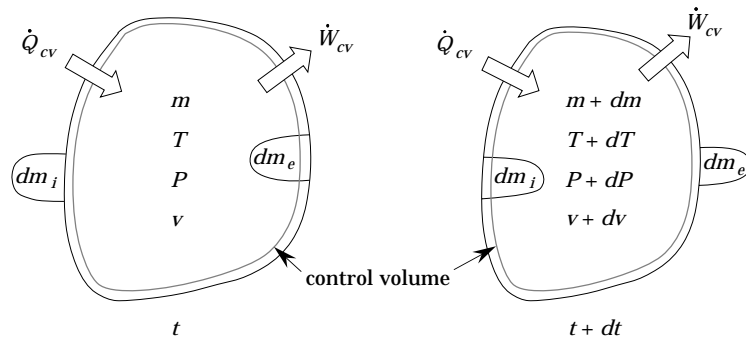


Figure B.1: Control volume at two subsequent instances.

E_{cv} or total control volume energy, can be expressed as a volume integral

throughout the control volume:

$$E_{cv} = \int_{cv} e \rho dV = \int_{cv} \left(u + \frac{C^2}{2} + gz \right) \rho dV = \tilde{e} \int_{cv} \rho dV = \tilde{e} m_{cv} \quad (\text{B.2})$$

The system to be considered here is that of the muscle and the inlet and outlet valves as shown in Fig. B.2. The muscle, including the tubing up to the valve orifices, is taken as the control volume. Inside this the state is assumed to be uniform. It is therefore necessary to keep the tube lengths at a minimum and their volume at a negligible level compared to the muscle's. Changes

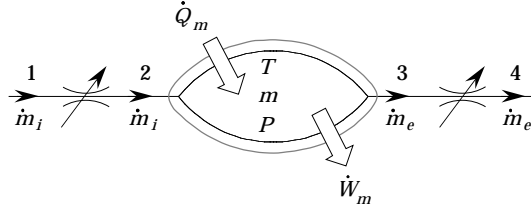


Figure B.2: Muscle and valves.

in potential energy are marginal or even non-existent and can be left out. During a time interval dt the work crossing an infinitesimal piece of muscle surface can be written as the product of the pressure, the area of that piece and the displacement perpendicular to the surface. Integrated throughout the boundary assuming uniform pressure, this results in the product of pressure and volume change

$$dW_m = P dV \quad (\text{B.3})$$

This, of course, holds only if there is no deformation of the muscle membrane due to surface stresses and if the inertia of the membrane and its moving parts is negligible.

The flow through a valve orifice is usually regarded as adiabatic (Ezekiel and Shearer, 1960) because the change of state happens in a very short time and small space. There is no transfer of technical work and the orifice contains no mass so the energy rate balance reduces to

$$h_{1(3)} + \frac{C_{1(3)}^2}{2} = h_{2(4)} + \frac{C_{2(4)}^2}{2} \quad (\text{B.4})$$

stating that the stagnation state enthalpy is not affected by the orifice.

Neglecting the mean kinetic energy of the gas inside the muscle, energy conservation can be put as

$$\dot{Q}_{cv} = \frac{d}{dt}(um) + \dot{W}_m + \dot{m}_e(h_3 + \frac{C_3^2}{2}) - \dot{m}_i(h_1 + \frac{C_1^2}{2}) \quad (\text{B.5})$$

If one assumes pressurized air to behave as an ideal gas, it is possible to simplify this further. Ideal gases show the following property relations:

$$PV = mrT \quad (\text{B.6a})$$

$$u = c_v(T - T_0) \quad (\text{B.6b})$$

$$h = c_pT - c_vT_0 \quad (\text{B.6c})$$

$$c_p = c_v + r \quad (\text{B.6d})$$

With these, one can write

$$\dot{Q}_m = \frac{d}{dt}(\frac{c_v}{r}PV) - \frac{d}{dt}(mc_vT_0) + P\dot{V} + \dot{m}_e(h_3 + \frac{C_3^2}{2}) - \dot{m}_i(h_1 + \frac{C_1^2}{2}) \quad (\text{B.7})$$

and using $c_p/c_v = \gamma$ and balance of mass flow rate, $\dot{m} = \dot{m}_i - \dot{m}_e$

$$\dot{Q}_m = \frac{d}{dt}(\frac{1}{\gamma-1}PV) + P\dot{V} + \dot{m}_e(c_pT_3 + \frac{C_3^2}{2}) - \dot{m}_i(c_pT_1 + \frac{C_1^2}{2}) \quad (\text{B.8})$$

Pneumatic systems are devised to get their energy mainly from the fluid pressure. Changes in fluid kinetic energy can be disregarded compared to the other terms in the energy rate equation (Shearer, 1960). Furthermore, because of the assumption of uniform state inside the muscle $T_3 = T$. This leads to the fundamental expression of the energy rate balance:

$$\begin{aligned} (\gamma - 1)\dot{Q}_m &= \dot{P}V + \gamma P\dot{V} + \gamma rT\dot{m}_e - \gamma rT_1\dot{m}_i \\ &= PV \left(\frac{\dot{P}}{P} + \gamma \frac{\dot{V}}{V} - \gamma \frac{T_1}{T} \frac{\dot{m}_i}{m} + \gamma \frac{\dot{m}_e}{m} \right) \end{aligned} \quad (\text{B.9})$$

Heat transfer, in general, is difficult to evaluate. Overall system behavior considerations supply a way to circumvent this. The main types of behavior are the isothermal, the adiabatic, the isentropic and the polytropic.

Isothermal case. Extremely slow acting systems tend to operate nearly isothermal, making \dot{Q}_m an important part of the balance equation. Since an isothermal change of state of a volume filled by an ideal gas is characterized by

$$\frac{\dot{P}}{P} + \frac{\dot{V}}{V} = \frac{\dot{m}}{m} \quad (\text{B.10})$$

(cf. Eq. B.6a) and $T_1 = T$, Eq. B.9 will simplify to

$$\dot{Q}_m = -V\dot{P} \quad (\text{B.11})$$

Adiabatic case. Fast acting systems on the other hand can be expected to have only a negligible heat transfer with respect to change of internal energy and power. They can be reliably regarded as adiabatic (Shearer, 1960). In this case Eq. B.9 reduces to

$$\frac{\dot{P}}{P} + \gamma \frac{\dot{V}}{V} = \gamma \frac{T_1}{T} \frac{\dot{m}_i}{m} - \gamma \frac{\dot{m}_e}{m} \quad (\text{B.12})$$

Isentropic case. If furthermore $T_1 = T$, the adiabatic model will also be isentropic, i.e. no internal irreversibilities occur. Conservation of energy in this case is given by

$$\frac{\dot{P}}{P} + \gamma \frac{\dot{V}}{V} = \gamma \frac{\dot{m}}{m} \quad (\text{B.13})$$

which is in fact non other than the well-known expression for adiabatic isentropic changes of state of ideal gases:

$$d(Pv^\gamma) = 0 \quad (\text{B.14})$$

This case is a strong simplification since it requires supply temperature to equal inside temperature at all times.

Polytropic case. Often in thermodynamical engineering, compression or expansion in a closed system can be approximately described by what is called a polytropic law:

$$d(Pv^n) = 0 \quad (\text{B.15})$$

with n called the index of expansion or compression, or more generally the polytropic coefficient. This is in fact an extension based on constant pressure, isothermal, isentropic and constant volume processes. They can be readily shown to have “polytropic coefficients” of 0, 1, γ and ∞ respectively.

This can be applied to open systems in the same way as proposed by Ohligschläger (1990). In a first instance dm_e is expelled from the control volume, dm_i is admitted and $m - dm_e$ undergoes a change of state governed by a polytropic law. Next an instantaneous mixing of dm_i and $m - dm_e$ occurs. This mixing is assumed to be adiabatic and at constant pressure and volume. Starting from a state characterized by m , P , T and V one can write for the polytropic change

$$(P + dP) \left(\frac{V + dV - dV_i}{m - dm_e} \right)^n = P \left(\frac{V - dV_e}{m - dm_e} \right)^n \quad (\text{B.16})$$

which is equivalent to

$$\frac{dP}{P} + n \frac{dV}{V} - n \frac{dV_i}{V} = -n \frac{dV_e}{V} \quad (\text{B.17})$$

The volumes of the entering and leaving masses can be expressed as

$$dV_i = v_i dm_i = \frac{rT_2}{P + dP} dm_i \approx \frac{rT_1}{P} dm_i = \frac{VT_1}{T} \frac{dm_i}{m} \quad (\text{B.18})$$

$$dV_e = v_e dm_e = \frac{rT}{P} dm_e = V \frac{dm_e}{m} \quad (\text{B.19})$$

leading to

$$\frac{\dot{P}}{P} + n \frac{\dot{V}}{V} = n \frac{T_1}{T} \frac{\dot{m}_i}{m} - n \frac{\dot{m}_e}{m} \quad (\text{B.20})$$

Combining Eqs. B.9 and B.20 offers an expression for the rate of heat transfer:

$$\dot{Q}_m = \frac{\gamma - n}{\gamma - 1} \left(P\dot{V} - rT_1\dot{m}_i + rT\dot{m}_e \right) \quad (\text{B.21})$$

Pressure difference expressions. An alternative way of expressing system behavior is by formulating the pressure differentials for an infinitesimal change of state. Eqs. B.9, B.10, B.12, B.13 and B.20 turn into

$$\text{general:} \quad dP = \frac{\gamma}{V} \left(rT_1 dm_i - rT dm_e - PdV + \frac{\gamma - 1}{\gamma} dQ_m \right) \quad (\text{B.22})$$

$$\text{isothermal:} \quad dP = \frac{1}{V} (rT dm - PdV) \quad (\text{B.23})$$

$$\text{adiabatic:} \quad dP = \frac{\gamma}{V} (rT_1 dm_i - rT dm_e - PdV) \quad (\text{B.24})$$

$$\text{isentropic:} \quad dP = \frac{\gamma}{V} (rT dm - PdV) \quad (\text{B.25})$$

$$\text{polytropic:} \quad dP = \frac{n}{V} (rT_1 dm_i - rT dm_e - PdV) \quad (\text{B.26})$$

Appendix C

Instrumentation

Quartz Load Washer Kistler Type 901A

Range	1500 kg
Resolution	1 g
Maximum allowable force	1650 kg
Sensitivity	43 pC/kg
Linearity	$\pm 0.5\%$
Insulation resistance	$10^{14} \Omega$
Capacity	$\approx 12 \text{ pF}$
Resonant frequency	60 kHz
Rise time	$\approx 7 \mu\text{s}$
Temperature coefficient	$\approx 0.025 \%/^{\circ}\text{C}$

Charge Amplifier Kistler Type 5001

Measuring ranges	10–500000 pC
Range capacitors	10–50000 pF
Output voltage	$\pm 10 \text{ V}_{\text{DC}}$
Output impedance	100Ω
Insulation at input	$> 10^{14} \Omega$

Frequency range	0–180 kHz
Time constant short	0.01–50 s
medium	1–5000 s
long	1000–100000 s
	(determined by drift)
Linearity	0.05%
Accuracy	±1%
Maximum drift	±0.03 pC/s
Temperature drift	max. ±0.1 mV/°C
Maximum capacity at input	100 nF

PEP ADC3

A/D converter chip	LTC1290DCN
Number of channels	8 differential
Resolution	12 bit
Hold time	8 μ s
Conversion time	43 μ s
Throughput rate	20 kHz
Linearity error	±3/4 LSB
Voltage ranges unipolar	0–5 V, 0–10 V
bipolar	–5–5 V, –10–10 V
Input resistance 5 V range	20 k Ω
10 V range	40 k Ω
EEPROM	93C46
Temperature range	0–70 °C
Temperature drift	Typ. 1 LSB at 10 V
Input circuitry: inverter and first order filter	
filter resistance	1 k Ω
capacitance	1 μ F
Opto-isolated	

PEP DAC3

D/A converter chip	AD7568B
Number of channels	4
Resolution	12 bit
Serial data transfer time	4 μ s per data word
Rise time	2.5 μ s/V
Linearity error	$\pm 3/4$ LSB
Voltage output ranges unipolar	0–10 V
bipolar	–10–10 V
Reference voltage	10 V
Maximum current	2 mA per channel
EEPROM	93C46
Temperature range	0–70 °C

Gauge pressure sensor Data Instruments XCA5-60GN

Temperature compensated silicon pressure sensor	
Supply voltage minimum	3.0 V _{DC}
nominal	8.0 V _{DC}
maximum	16.0 V _{DC}
	ratiometric output
Supply current	< 2 mA
Linearity & hysteresis	$\pm 0.5\%$ span
Repeatability	0.1% span
Zero offset	1.0 V _{DC}
Nominal full scale output	6.0 V _{DC}
Full scale pressure	60 PSI
Proof pressure	180 PSI
Response time	0.1 ms
Compensated temperature	70 °C

Potentiometer Sakae FCP40A

Resistance value	1 k Ω
Total resistance tolerance	$\pm 10\%$
Linearity	$\pm 0.05\%$
Output smoothness	$< 0.1\%$ against input voltage
Contact resistance variation	$< 2\%$ C.R.V.
Power rating	3.0 W
Electrical travel	$350^\circ \pm 5^\circ$
Mechanical travel	360°
Insulation resistance	$> 1 \text{ G}\Omega$ at 1 kVDC
Starting torque	$< 4 \text{ mN m}$
Resistance temperature coefficient	$\pm 400 \text{ ppm}/^\circ\text{C}$
Weight	80 g

Pressure servo-valves Kolvenbach KPS 3/4

Proportional, electromagnetically actuated	
Supply voltage	24 VDC $\pm 10\%$
Supply current	max. 0.8 A
Signal input voltage	0–10 VDC
Input impedance	50 k Ω
Output	0–10 VDC
Supply pressure	0–10 bar
Output pressure	0–10 bar
Gain	1 bar/VDC
Hysteresis	0.5 % FS
Accuracy	$< 1\%$ FS
Reaction time	5 ms
Maximum flow 6 bar \rightarrow 0 bar (gauge)	550 Std.l/min
6 bar \rightarrow 5 bar (gauge)	300 Std.l/min

Weight	1 kg
Temperature range	0–50 °C

Pressure servo-valves Hoerbiger-Origa Tecno

Proportional, piezoelectrically actuated

Supply voltage	24 VDC \pm 10%
Supply current	max. 10 mA
Nominal electric power	0.25 W
Signal input voltage	0–10 VDC
Input impedance	200 k Ω
Output	0–10 VDC
Supply pressure	1.5–10 bar
Output pressure	0–8 bar
Gain	1 bar/VDC
Repeatability	< 0.2 % FS
Hysteresis	< 0.2 % FS
Sensitivity	< 0.2 % FS
Linearity	< 0.5 % FS
Reaction time	\approx 5 ms
Flow constants: b	0.132
C	29.9 Std.l/min bar
Maximum flow 6 bar \rightarrow 5 bar (gauge)	115 Std.l/min
Weight	225 g
Temperature range	0–50 °C

Pressure servo-valves Matrix EPR 100

PWM, electromagnetically actuated

Supply voltage	24 VDC \pm 10%
Nominal electric power	2 W

Signal input voltage	0–5(10) VDC
Supply pressure	1–8 bar
Output pressure	0–7 bar
Gain	7/5(10) bar/VDC
Repeatability	< 1% FS
Hysteresis	< 1% FS
Sensitivity	< 1% FS
Linearity	< 1% FS
Reaction time	5 ms
Rise time 2–4 bar ($p_s = 8$ bar, $V = 30$ cm ³)	60 ms
Fall time 4–2 bar ($p_s = 8$ bar, $V = 30$ cm ³)	100 ms
Maximum flow 6 bar → 0 bar (gauge)	60 Std.l/min
Weight	400 g
Temperature range	–10–50 °C

Nomenclature

A	membrane parallel cross-sectional area	m^2
	orifice flow section area	m^2
a	membrane compliance	–
	skeletal muscle constant	N
b	pleat width or pitch	m
	skeletal muscle constant	m s^{-1}
	pneumatic valve critical pressure ratio	–
C	gas velocity	m s^{-1}
	compliance, linear motion	m N^{-1}
	rotative motion	$\text{N}^{-1} \text{m}^{-1}$
	pneumatic valve flow constant	$\text{Std.m}^3 \text{s}^{-1} \text{Pa}^{-1}$ ($\text{Std.l min}^{-1} \text{bar}^{-1}$)
c_1	constant = $\sigma_1 sr$	N
c_2	constant = $p_i/2c_1$	m^{-2}
c_3	constant = $F_t/2\pi c_1$	–
c_p	constant pressure specific heat = 1000.5 for dry air at 300 K	$\text{J kg}^{-1} \text{K}^{-1}$
c_v	constant volume specific heat = 718 for dry air at 300 K	$\text{J kg}^{-1} \text{K}^{-1}$
D	muscle equatorial diameter	m
d	muscle equatorial diameter function	–
d_0	muscle equatorial diameter function, inelastic case	–
$d_{0\text{max}}$	muscle bulk diameter to full length ratio, inelastic case	–
d_{c1}	end fitting cone's smallest face diameter	m
d_{c2}	end fitting cone's highest face diameter	m
d_{ci}	end fitting cone inner diameter	m

d_{cm}	end fitting cone's median face diameter	m
d_{ri}	inner diameter of the end fitting outer ring	m
d_{ro}	outer diameter of the end fitting outer ring	m
d_{tr}	end fitting teeth root diameter	m
E	Young's modulus	Pa
	extensive energy	J
	error signal	rad
e	intensive energy	J kg^{-1}
	lever drive eccentricity	m
F	force	N
F_r	muscle radial or transverse force	N
F_t	muscle traction	N
f_t	muscle traction or force function	–
f_{t0}	muscle force function, inelastic case	–
$G_{ol}(s)$	open-loop controlled system transfer function	–
g	standard gravity = 9.81	m s^{-2}
$H(s)$	Δp -model system transfer function	–
h	intensive enthalpy	J kg^{-1}
J	moment of inertia	kg m^2
K	stiffness, linear motion	N m^{-1}
	rotative motion	Nm
K_I	integral controller gain	$\text{V rad}^{-1} \text{s}^{-1}$
K_P	proportional controller gain	V rad^{-1}
K_m	stiffness due to changing effective area	Nm
K_p	stiffness due to pressure change	Nm
K_P	steady state rotational position gain	rad V^{-1}
k	slope of rotative actuator torque function to angle of rotation relation	rad^{-1}
k_m	stiffness factor due to changing effective area	–
k_p	stiffness factor due to pressure change	–
L	link's compressed length	m
l	full muscle length at rest	m
	length	m
l_r	resin filling height	m
l_s	braided muscle strand length	m
l_t	end fitting tooth length	m
M	torque	Nm
m	mass	kg
	elliptic integral parameter	–
	rotative actuator torque function	–
m_0	rotative actuator torque function at central position	–

\dot{m}	mass flow	kg s^{-1}
n	polytropic constant	–
	integer	–
P	absolute pressure	Pa (bar)
P_0	ambient absolute pressure	Pa (bar)
P_s	supply pressure	Pa (bar)
p	gauge pressure = $P - P_0$	Pa (bar)
p_m	mean muscle gauge pressure	Pa
p_S	material surface pressure	Pa
\dot{Q}	rate of heat transfer	W
R	muscle radius at zero pressure and contraction	m
r	dry air gas constant = 287	$\text{J kg}^{-1} \text{K}^{-1}$
	radial membrane coordinate	m
	joint lever arm	m
r_0	muscle equatorial radius at full inflation	m
r_f	foot eccentricity	m
S	surface	m^2
s	membrane thickness	m
	Laplace variable	s^{-1}
T	temperature	K
T_s	gas supply temperature	K
	sampling period	s
t	time	s
	pleat or fold depth	m
t_d	time delay	s
U	servo-valve input signal	V
U_m	mean servo-valve input signal	V
u	intensive internal energy	J kg^{-1}
V	volume	m^3
v	specific volume	$\text{m}^3 \text{kg}^{-1}$
	muscle volume function	–
v_0	muscle volume function, inelastic case	–
W	work	J
W_d	material deformation work	J
W_l	work transferred to load	J
W_m	work crossing a membrane's boundary	J
x	longitudinal membrane coordinate	m
z	height coordinate	m
α	elliptic integral modulus	rad
	angle of rotation	rad

β	angle between muscle axis and meridian	rad
γ	specific heat ratio = c_p/c_v = 1.4 for dry air at 300 K	–
	cone angle	°
ϵ	contraction	–
ε	strain	–
θ	weave angle	°
ν	Poisson's ratio	–
ρ	density	kg m ⁻³
	friction angle	°
σ_1	membrane meridional stress	Pa
σ_2	membrane parallel stress	Pa
σ_{np}	plug compressive stress normal to meridional section	Pa
σ_{nr}	resin tensile stress normal to meridional section	Pa
ς	membrane stress function	–
ς_0	membrane stress function, inelastic case	–
τ	time constant	s
τ_c	= $K_P/K_I + T_s/2$	s
τ_{sf}	filament facial shear stress	Pa
τ_{sr}	resin shear stress	Pa
φ	elliptic integral amplitude	rad
χ	gas compressibility	Pa ⁻¹ (bar ⁻¹)
ω	frequency	rad s ⁻¹
ω_n	natural frequency	rad s ⁻¹
ω_s	sampling frequency	rad s ⁻¹

Bibliography

- M. Abramowitz and I. A. Stegun. *Handbook of Mathematical Functions*, chapter 17, pages 589–594. Dover Publications Inc., New York, 1965.
- H. A. Baldwin. Realizable models of muscle function. In *Biomechanics, Proceedings of the First Rock Biomechanics Symposium*, pages 139–148, New York, 1969. Plenum Press.
- P. Beomonte Zobel, T. Raparelli, G. Mattiazzo, S. Mauro, and M. Velardocchia. Force control with fuzzy logic for pneumatic rubber muscles. In *Advanced Robotics Beyond 2000 - The 29th International Symposium on Robotics*, Birmingham, UK, 1998. dmg Business Media Ltd.
- Th. Beullens. Hydraulic or pneumatic drive device. US Patent No. 4,841,845, 1989.
- H. Bühler. *Conception de Systèmes Automatiques*, chapter 10. Presses Polytechniques Romandes, 1988.
- D. G. Caldwell. Natural and artificial muscle elements as robot actuators. *Mechatronics*, 3(3):269–283, 1993.
- D. G. Caldwell, G. A. Medrano-Cerda, and M. J. Goodwin. Braided pneumatic actuator control of a multi-jointed manipulator. In *IEEE International Conference on Systems, Man and Cybernetics*, pages 423–428, Le Touquet, 1993a.
- D. G. Caldwell, G. A. Medrano-Cerda, and M. J. Goodwin. Characteristics and adaptive control of pneumatic muscle actuators for a robotic elbow. In *IEEE International Conference on Robotics and Automation*, pages 3558–3563, San Diego, 1994.

- D. G. Caldwell, G. A. Medrano-Cerda, and M. J. Goodwin. Control of pneumatic muscle actuators. *IEEE Control Systems Magazine*, 15(1):40–48, 1995.
- D. G. Caldwell, A. Razak, and M. J. Goodwin. Braided pneumatic muscle actuators. In *IFAC Conference on Intelligent Autonomous Vehicles*, pages 507–512, Southampton, 1993b.
- D. G. Caldwell, N. Tsagarakis, D. Badihi, and G. A. Medrano-Cerda. Investigation of bipedal robot locomotion using pneumatic muscle actuators. In *IEEE International Conference on Robotics and Automation*, pages 799–804, Albuquerque, New Mexico, 1997.
- D. G. Caldwell, N. Tsagarakis, D. Badihi, and G. A. Medrano-Cerda. Pneumatic muscle actuator technology: a light weight power system for a humanoid robot. In *IEEE International Conference on Robotics and Automation*, pages 3053–3058, Leuven, Belgium, 1998.
- J. Carvill. *Mechanical Engineer's Data Handbook*. Butterworth-Heinemann Ltd., Oxford, 1993.
- C.-P. Chou and B. Hannaford. Measurement and modeling of McKibben pneumatic artificial muscles. *IEEE Transactions on Robotics and Automation*, 12(1):90–102, 1996.
- F. Daerden, D. Lefeber, and P. Kool. Using free radial expansion pneumatic artificial muscles to control a 1DOF robot arm. In *First International Symposium on Climbing and Walking Robots*, pages 209–214, 1998.
- H. Ebertshäuser. *Fluidtechnik von A bis Z*. Vereinigte Fachverlage, Mainz, 1989.
- A. Erdelyi. *Higher Transcendental Functions*, volume 2, chapter XIII—part one, pages 295–299. Krieger, Malabar, 1981.
- F. D. Ezekiel and J. L. Shearer. Pressure-flow characteristics of pneumatic valves. In J. F. Blackburn, G. Reethof, and J. L. Shearer, editors, *Fluid Power Control*, chapter 8. The M.I.T. Press, 1960.
- A. G. Feldman. Once more on the equilibrium-point hypothesis (λ model) for motor control. *Journal of Motor Behavior*, 18(1):17–54, 1986.
- M. M. Gavrilović and M. R. Marić. Positional servo-mechanism activated by artificial muscles. *Medical and Biological Engineering*, 7:77–82, 1969.
- I. M. Gelfand and S. V. Fomin. *Calculus of Variations*, section 1.12. Prentice-Hall Inc., Englewood Cliffs, 1963.

- S. Greenhill. The digit muscle. *Industrial Robot*, 20(5):29–30, 1993.
- J. J. Grodski and G. B. Immega. Myoelectric control of compliance on a ROMAC protoarm. In *International Symposium on Teleoperation and Control*, pages 297–308, 1988.
- B. Hannaford and J. M. Winters. Actuator properties and movement control: Biological and technological models. In J. M. Winters and S. L.-Y. Woo, editors, *Multiple Muscle Systems: Biomechanics and Movement Organization*, chapter 7, pages 101–120. Springer-Verlag Inc., New York, 1990.
- B. Hannaford, J. M. Winters, C.-P. Chou, and P.H. Marbot. The anthroform biorobotic arm: A system for the study of spinal circuits. *Annals of Biomedical Engineering*, 23:399–408, 1995.
- T. Hesselroth, K. Sarkar, P. P. van der Smaght, and K. Schulten. Neural network control of a pneumatic robot arm. *IEEE Transactions on Systems, Man and Cybernetics*, 24(1):28–38, 1994.
- N. Hogan. Adaptive control of mechanical impedance by coactivation of antagonistic muscles. *IEEE Transactions on Automatic Control*, AC-29(8):681–690, 1984.
- J. M. Hollerberg, I. W. Hunter, and Ballentyne J. A comparative analysis of actuator technologies for robotics. In O. Khatib, J. J. Craig, and T. Lozano-Perez, editors, *The Robotics Review 2*, pages 299–342. The MIT Press, Cambridge, Massachusetts, 1991.
- J. C. Houk. Regulation of stiffness by skeletomotor reflexes. *Annual Review of Physiology*, 41:99–114, 1979.
- I. W. Hunter and S. Lafontaine. A comparison of muscle with artificial actuators. In *Technical Digest of the IEEE Solid-State Sensor and Actuator Workshop*, pages 178–185, 1992.
- G. Immega. Tension actuator load suspension system. US Patent No. 4,826,206, 1989.
- G. Immega and M. Kukolj. Axially contractable actuator. US Patent No. 4,939,982, 1990.
- G. B. Immega. ROMAC muscle powered robots. Technical Report MS86-777, Society of Manufacturing Engineers, Dearborn, 1986.
- G. B. Immega. ROMAC actuators for micro robots. In *IEEE Micro Robotics and Teleoperators Workshop*, Hyannis, Massachusetts, 1987.

- K. Inoue. Rubbertuators and applications for robotics. In *4th International Symposium on Robotics Research*, pages 57–63, 1987.
- R. Isermann and U. Raab. Intelligent actuators—Ways to autonomous systems. *Automatica*, 29(5):1315–1331, 1993.
- D. A. Jones and J. M. Round. *Skeletal Muscle in Health and Disease*. Manchester University Press, 1990.
- H. Kleinwachter and J. Geerk. Device with a pressurizable variable capacity chamber for transforming a fluid pressure into a moment. US Patent No. 3,638,536, 1972.
- H. Kraus. *Thin Elastic Shells*, chapter 1, 2 and 4. John Wiley & Sons Inc., New York, 1967.
- A. I. Krauter. Hydraulic muscle pump. US Patent No. 5,014,515, 1991.
- M. Kukulj. Axially contractable actuator. US Patent No. 4,733,603, 1988.
- B. C. Kuo. *Digital Control Systems*, chapter 2. Holt, Rinehart and Winston, Inc., 1980.
- Yuan Lü. *Elektropneumatischer Positionierantrieb mit schnellen Schaltventilen*. PhD thesis, RWTH Aachen, 1992.
- J. Marcinčin and A. Palko. Negative pressure artificial muscle—An unconventional drive of robotic and handling systems. In *Transactions of the University of Košice*, pages 350–354, Slovak Republic, 1993. Riečansky Science Publishing Co.
- J. Marcinčin and J. Smrček. The atypical actuators for advanced robotic devices. In *3rd International Workshop on Robotics in Alpe-Adra Region*, pages 111–117, Slovenia, 1994a.
- J. N. Marcinčin and J. Smrček. The UPAM—New actuator for advanced robotic devices. In *25th International Symposium on Industrial Robots*, pages 299–304, Germany, 1994b.
- J. N. Marcinčin, J. Smrček, and J. Niznik. Bioactuators—Most efficient actuators for biomechanics. In *7th International IMEKO TC-13 Conference on Measurement in Clinical Medicine—Model Based Biomeasurements*, pages 369–371, Slovak Republic, 1995.
- W. Matek, D. Muhs, H. Wittel, and M. Becker. *Machine-onderdelen*, chapter 12. Academic Service, Schoonhoven, 1993.

- Th. A. McMahon. *Muscles, Reflexes, and Locomotion*. Princeton University Press, 1984.
- M. J. Moran and H. N. Shapiro. *Fundamentals of Engineering Thermodynamics*. John Wiley and Sons Inc., 1992.
- A. H. Morin. Elastic diaphragm. US Patent No. 2,642,091, 1953.
- B. M. Nigg and W. Herzog, editors. *Biomechanics of the Musculo-skeletal System*. John Wiley & Sons, 1994.
- O. Ohligschläger. *Pneumatische Zylinderantriebe—Thermodynamische Grundlagen und digitale Simulation*. PhD thesis, RWTH Aachen, 1990.
- H. M. Paynter. Tension actuated pressurized gas driven rotary motors. US Patent No. 3,854,383, 1974.
- H. M. Paynter. High pressure fluid-driven tension actuators and methods for constructing them. US Patent No. 4,751,869, 1988a.
- H. M. Paynter. Hyperboloid of revolution fluid-driven tension actuators and methods of making. US Patent No. 4,721,030, 1988b.
- J. J. Pipliacampi. Organic fibers. In Th. J. Reinhart, C. A. Dostal, M. S. Woods, H. J. Frissell, and A. W. Ronke, editors, *Engineered Materials Handbook*, volume 1, section 2, pages 55–57. American Society of Civil Engineers, Metals Park, 1988.
- U. Raab and R. Isermann. Actuator principles with low power. In VDI/VDE *Tagung Actuator 90*, Bremen, 1990.
- Th. J. Reinhart, C. A. Dostal, M. S. Woods, H. J. Frissell, and A. W. Ronke, editors. *Engineered Materials Handbook*, volume 1. American Society of Civil Engineers, 1988.
- H. F. Schulte. The characteristics of the McKibben artificial muscle. In *The Application of External Power in Prosthetics and Orthotics*, number Publication 874, pages 94–115. National Academy of Sciences–National Research Council, Lake Arrowhead, 1961.
- R. Schwenzer. *Entwurf und Auslegung servopneumatischer Antriebsregelungen*. PhD thesis, RWTH Aachen, 1983.
- J. R. Shaefgen. Aramid fibers: Structure, properties and applications. In A. E. Zachariades and R. S. Porter, editors, *The Strength and Stiffness of Polymers*, pages 327–355. Marcel Dekker Inc., New York, 1983.

- J. L. Shearer. Pneumatic drives. In J. F. Blackburn, G. Reethof, and J. L. Shearer, editors, *Fluid Power Control*, chapter 16. The M.I.T. Press, 1960.
- J. Smrček, J. N. Marcinčin, and J. Niznik. The under pressure artificial muscle (UPAM)—New actuator in biorobotics. In *5th International Symposium on Measurement and Control in Robotics*, pages 199–203, Slovak Republic, 1995.
- S. P. Timoshenko and S. Woinowsky-Krieger. *Theory of Plates and Shells*, chapter 14, pages 429–434. McGraw-Hill Kogakusha Ltd., Tokyo, 1959.
- B. Tondu, V. Boitier, and P. Lopez. Natural compliance of robot-arms based on McKibben artificial muscle actuators. In *European Robotics and Intelligent Systems Conference*, pages 783–797, Malaga, 1994.
- B. Tondu, V. Boitier, and P. Lopez. Théorie d'un muscle artificiel pneumatique et application à la modelisation du muscle artificiel de McKibben. In *Comptes Rendus de l'Académie des Sciences*, number t.320, Série IIb, pages 105–114. Académie des Sciences, Paris, 1995.
- R. E. Wilfong and J. Zimmerman. Strength and durability characteristics of kevlar aramid fiber. *Journal of Applied Polymer Science: Applied Polymer Symposium*, 31:1–21, 1977.
- J. M. Winters. Braided artificial muscles: Mechanical properties and future uses in prosthetics/orthotics. In *RESNA 13th Annual Conference*, pages 173–174, Washington DC, 1995.
- J. E. Woods. Mechanical transducer with expansible cavity. US Patent No. 2,789,580, 1957.
- J. M. Yarlott. Fluid actuator. US Patent No. 3,645,173, 1972.
- H. Yoshinada, T. Yamazaki, T. Suwa, T. Naruse, and H. Ueda. Seawater hydraulic actuator for subsea manipulator. In *Proceedings of the ISART*, pages 559–566, 1991.
- G. I. Zahalak. Modeling muscle mechanics (and energetics). In J. M. Winters and S. L.-Y. Woo, editors, *Multiple Muscle Systems: Biomechanics and Movement Organization*, chapter 1, pages 1–23. Springer-Verlag Inc., New York, 1990.